NEUTRON PRODUCTION IN A SPHERICAL PHANTOM ABOARD THE INTERNATIONAL SPACE STATION

By

Azadeh Tasbaz

A Thesis Submitted in Partial Fulfillment
of the Requirements for the Degree of

Master of Applied Science

In

Faculty of Energy Systems and Nuclear Science

Program

University of Ontario Institute of Technology

December, 2010

Abstract

Since the beginning of space exploration in last century, several kinds of devices from passive and active dosimeters to radiation environment monitors have been used to measure radiation levels onboard different space crafts and shuttles allowing the space community to identify and quantify space radiation. The recent construction of several laboratories on the International Space Station (ISS) has confirmed that prolonged duration space missions are now becoming standard practice and as such, the need to better understand the potential risk of space radiation to Astronaut's health, has become a priority for long mission planner.

The complex internal radiation environment created within the ISS is due to high-energy particle interactions within the ISS shielded environment. As a result, a large number of secondary particles, that pose specific health risks, are created. Neutrons are one important component of this mixed radiation field due to their high LET. Therefore, the assessment of the neutron dose contribution has become an important part of the safety and monitoring program onboard the ISS. The need to determine whether neutron dose measured externally to the human body give an accurate and conservative estimate of the dose received internally is of paramount importance for long term manned space missions.

This thesis presents a part of an ongoing large research program on radiation monitoring on ISS called Matroshka-R Project that was established to analyze the radiation exposure levels onboard the ISS using different radiation instruments and a spherical phantom to simulate human body. Monte Carlo transport code was used to simulate the interaction of high energy protons and neutrons with the spherical phantom currently onboard ISS. A Monte Carlo model of the phantom has been built, and it consists of seven spherical layers presenting different depths of

the simulated tissue. The phantom has been exposed to individual proton energies and to a spectrum of neutrons. The flux of the created neutrons inside the phantom has been calculated. The internal to external neutron flux ratio was calculated and compared to the experimental data, recently, measured on three separate expeditions of the ISS. The results from the calculations showed that the value of the neutron fluxes inside and outside the phantom is different from the data recently measured with bubble detectors.

.

Key words

Space Radiation, Dosimetry, Phantom, Neutron, Proton, International Space Station, Radiation Risk, Monte Carlo Simulation.

.

Table of Contents

Acknowledgement

First and for most I would like to thank my supervisor Dr. Rachid Machrafi, who provided significant guidance and support during the course of this thesis. I would also like to thank all the faculty and staff who have shaped my mind throughout my studies at UOIT. A special thank to my family who with continual patience and love has supported me throughout my life. Finally, an honourable mention goes to many friends who supported me through my graduate years.

List of Tables

List of Figures

List of Appendices

Acronyms

ACR	Anomalous Cosmic Radiation
ALARA	As Low As Reasonably Achieved
AmBe	Americium Beryllium
BFO	Blood Forming Organs
BBND	Bonner Ball Neutron Detector
BD	Bubble Detector
CPD	Crew Passive Dosimetry
CGS	Centimetre-Gram-Second System
DNA	Deoxyribonucleic Acid
DOSTEL	Dosimetry Telescope
ESA	European Space Agency
EV-CPDS	Extravehicular Charge Particle Directional Spectrometers
FF	Fission Foils
GCR	Galactic Cosmic Rays
HRD	High Rate Dosimetry
HZE	High Z-Charged Particles
$H^*(10)$	Ambient Dose Equivalent
$H_p(10)$	Personal Dose Equivalent
ICRU	International Commission on Radiological Units
ICRP-51	International Radiation Protection Committee report $N^0 51$
ICRP-60	International Radiation Protection Committee report $N^0 60$
IV-CPDS	Intravehicular Charge Particle Directional Spectrometers

ISS	International Space Station
LET	Linear Energy Transfer
LEO	Low Earth Orbit
LANSCE	Los Alamos Nuclear Service Center
LiF	Lithium Fluoride
MCC	Mission Control Center
MCNP	Monte Carlo N-Particle
MCNPX	Monte Carlo N-Particle eXtended
MOSFET	Metal Oxide Semiconductor Field-Effect Transistor
NPE	Nuclear Photoemulsions
NASA	National Aeronautic and Space Administration
NASDA	National Space Development Agency of Japan
NeM	Neutron spectrometer system
PNTD	Plastic Nuclear Track Detector
PDS	Passive Dosimetry Systems
RBE	Relative Biological Effect
RP	Recoil Proton
RRMD	Radiation Area Monitors
RSA	Russian Space Agency
RAMs	Radiation Area Monitors
SBD	Space Bubble Detectors
SFD	Scintillation Fiber Detector
SPE	Solar Particle Evente

SRIM	The Stopping and Range of Ions in Matter
TEPC	Tissue Equivalent Proportional Counter
TLD	Thermoluminescent Detectors

Glossary

Deoxyribonucleic acid	The nucleic acid that contains the genetic instructions
Galactic Cosmic Rays	High energy protons, electrons or heavy energetic particles produced outside the solar system
HZE	High energy protons, electrons and other heavy nuclei that are released from the sun
Linear Energy Transfer	The amount of energy absorbed per unit of length
Low Earth Orbit	An Orbit within the Locus extending from the Earth's surface up to an altitude of 2,000 km

Nomenclature

A	Thickness of the Slab
C_i	Neutron Count at the Detector i
DE_n	Ambient Neutron Dose calculated using Bubble Detector
D_γ	Dose with Low LET
$D(L)$	Dose from the Radiation Environment at a point 10 mm Deep within the ICRU Sphere (a sphere of tissue-equivalent material with a diameter of 30 cm)
$D_{R,T}$	Average Absorbed Dose from Radiation R in Tissue T
$E_2(z=n\sigma a)$	The Exponential Integral of order 2
E_{min}	Minimum Energy Required for Bubble Formation
F4	Flux Tally in MCNPX
$F_t(Z, E, t)$	Time Dependent Function of Spectrum of Particle with Charge Z
$F_r(Z, E, t)$	Radial Dependent Function of Spectrum of Particle with Charge Z
$F_q(Z, E, t)$	Heliolatitude Dependent Function of Spectrum of Particle with Charge Z
$F_f(Z, E, t)$	Heliolongitude Dependent Function of Spectrum of Particle with Charge Z
H_T	Dose Equivalent

H	The Molar Heat of Vaporization
$H^*(10)/\Phi$	Ratio of the Ambient Dose Equivalent $H^*(10)$ and Neutron Fluence Φ
$J(y)$	The Differential Lineal Energy Spectrum
k	The Proportionality Constant Related to the Unit of Measurement
K_{γ}	Dose Rate Coefficient for Low Dose Rate
$J_0(Z, E)$	Local Interstellar Spectrum of Particle with Charge Z
M	The Molecular Weight
M_u	The Number of Bubble by Bubble Detector
P_v	The Density of the Vapour
q	The Quality Factor taken from ICRP-60
R_{γ}	Cancer Risk From the Low LET
$R(i, E)$	The Neutron Spectrum Function at the Detector i
RD_{amb}	The Calibration Factor for Bubble Detector
$R_{\Phi}(E)$	The Response Function of Bubble Detector
r_c	The Critical Radius for Bubble Formation
T	Track Length

v	Volume of the Cell
w	Particle Weight
w_R	Radiation Weighting Factor
y	The Lineal Energy
γ	The Surface Tension of the Liquid
Δ	The Degree of Superheat
$\Phi(E)$	The Neutron Spectrum Function at the Detector i
σ	Cross Section
Φ	Flux
$\rho(v)$	Neutron Density with Velocity v
Φ_0	Incident Flux of Neutron on a Slab of Thickness ‘a’

Introduction

Due to its significant contribution to health risks of the astronauts, space radiation has been a major concern for space research for several decades. Being exposed for a long period of time to space radiation, Astronauts are open to several health risks. These effects can be divided into two broad categories, acute effects and long term effects. The acute effect is seen immediately after radiation exposure such as skin redness, vomiting, and dehydration. While the long term effect of the radiation exposure causes cell damage such as DNA damage that may lead to a cell death or cell deformation. The acute effect is not that much of concern since the cells can be reproduced by the body itself. However cells that deform can produce abnormal ones and this may cause cancer. Also, at very high doses of radiation, cells cannot be replaced fast enough, and this leads to death of the irradiated person.

There are several parameters that can be taken into consideration, mainly, the structure material and design of the spacecraft, its altitude and weather conditions to protect the astronauts from being exposed to radiation during the space missions.

The radiation environment inside the International Space Station (ISS) is an extremely complex mixture of photons, charged and neutral particles whose levels in a near-earth orbit are dependent on the phase of the solar activity cycle, geophysical and orbital parameters of the space station. This complex mixture of different particles is different from radiation field on earth in terms of energy and intensity. Space radiation falls into three main types: Galactic Cosmic Rays (GCR), Solar Particle Events (SPE) and trapped high energy electrons and protons by the Earth's magnetic field, which is called the Van Allen belts. All three forms of radiation

can be extremely dangerous to astronauts, especially when they are performing extravehicular activities.

Other than the primary radiation sources, there are also secondary particles resulting from the interaction of the primary particles with the material of space-crafts (photons, neutrons and others).

Space radiation has a wide energy, charge and linear energy transfer (LET) ranges and in such complex field it is, extremely, difficult to measure the radiation exposure even with very sophisticated instrumentations. Therefore, measurements of radiation dose in different spacecrafts has been a concern for many years and different research groups around the world have attempted to quantify different components of space radiation using different calculation models and different types of instrumentation to understand the interaction of space radiation with shielded environment.

Currently, there are many ongoing research studies using different simulation codes to analyze and calculate the radiation doses. In addition, there are different types of detectors used to characterize the space radiation field. These devices can be grouped into two types: passive and active detectors. Passive detectors such as TLDs, plastic track detectors and nuclear emulsions give only integral measurements, while active detectors such as TEPC and silicon detectors, are used for real time monitoring [1].

As secondary particles with high LET, neutrons are very important component in any shielded space environment in terms of dose contribution. They contribute about 20 to 35% to the total dose equivalent of the astronaut [2]. Because of the lack of charge, neutrons can penetrate deep inside the human tissue without experiencing Coulomb interaction with atomic electrons.

Therefore they can get close to the nuclei and interact with it to create secondary radiation that ionizes the tissue and causes biological damage.

Due to the broad energy range of neutrons, their detection has become a complex task for researchers and it is even more complicated in space due to the fact that neutrons are mixed with many other particles.

L. Heilbronn presented an overview of ground-base neutron measurements relevant to galactic cosmic rays and solar particle events transported through shielding material in space and he has reported that 57%, 40% and less than 2% of the neutron dose equivalent rate could come from neutrons with energies above 10 MeV, 50 MeV and 200 MeV, respectively [3].

The real time energy spectrum of neutron in space shuttle (STS-89 during January 24-27, 1998) was reported, using Bonner Ball Neutron Detector (BBND), by H. Matsumoto and his colleagues [4]. The energy range of secondary neutrons is broad and it extends from thermal to 100 MeV. The dose equivalent rate of 75 μSv/d, for neutrons of 1-10 MeV, was reported in reference [4].

Russians have measured the neutron energy spectra on the MIR orbital station. Such work has been conducted by V. I. Lyagushin for three energy intervals: from thermal to 10 KeV, 10 KeV-20 MeV and 20 to 400 MeV. Measurements were taken using four different techniques, namely, nuclear photo-emulsions, fission foils, recoil protons using an organic scintillator and a CsI crystal. The total neutron dose equivalent reported in this work ranges from 76-130 μSv/d [5].

In terms of instrumentation, different types of detectors have been used to measure neutron doses. L. A. Braby, in his work, discusses the use of a tissue equivalent proportional counter (TEPC) as a neutron detector [6]. This device is an active detector and has been used in different areas for neutron dose measurement. However, the device is sensitive to all types of radiations

and therefore, the measured dose is a contribution from other sources of radiation rather than just from neutrons. To overcome this problem, L. A. Braby, used two proportional counters: one typical TEPC and the other a carbon proportional counter, which is sensitive only to charged particles, in order to distinguish between neutrons and charged particles.

H. Ing reported that neutrons above 10 MeV contribute half of the dose equivalent, the measurement was done using bubble detectors on the Bion-9 and 10, Mir, STS-81, 84, 86, 89 and 91. However, the bubble detector has an unknown response for neutrons above 20 MeV and the dose equivalent measured with such device on the space shuttles ranges from 80 to140 μSv/d where about 23% of such value is a contribution of fast neutrons (10-20 MeV) [7].

Another study was conducted by G.D. Badhwar and his colleagues; they reported neutron dosimetric measurements onboard seven shuttle flights with the use of passive detectors [8]. Two different techniques were used to measure the neutrons in the energy ranges of 1-14 MeV: recoil proton measurements and Bonner spheres with different diameters with imbedded Au foils. It was found that, the contribution of neutrons with energies less than 1 MeV to the total dose equivalent is less than 5%, and neutrons of 1-10 MeV dose equivalent contribution is 50% of the total dose equivalent. The dose measurements depend on the altitude, solar conditions and shielding locations [8].

R. Machrafi and colleagues, as part of the Matroshka-R project, using space bubble detectors (SBDs) on the international space station, reported that internal and external dose measured on the surface and inside a spherical phantom are almost the same. In their work, the ratio of the internal to external dose is consistent in different sessions of measurements [9].

Although there are few groups conducting researches on space radiation and on neutron dose measurements in particular, up to now, there are no accurate measurement of the neutron spectra and neutron dose on the international space station. Previous studies show that the neutron dose received internally and externally in space environment is almost the same [9] whereas on earth, due to the attenuation of neutrons, the internal dose is much less than its external value. In fact the complexity of the space radiation field inside the space craft doesn't allow drawing clear conclusions on this big difference between the ratio of the internal to external dose in space compared to such ratio on earth. It is also not clear why the experimental results are in variance with the theoretical results [8]. It is more probably, that the difference is related to other secondary particles such as protons, which don't interact with the shielding material and go through to interact directly with the phantom itself. From the interaction of these high energy protons, there will be additional secondary neutrons produced inside the phantom that compensate for the attenuation of the neutrons entering the phantom surface.

This thesis is a part of a large program on radiation monitoring on the international space station. It presents a contribution to an ongoing investigation and measurements of the neutron dose aboard the International Space Station (ISS). The objective of the work is to study the neutron production in a spherical phantom currently flying aboard the international space station and compared the results with experimental measurements. Also, the work aims to clarify the relationship between the internal and external doses measured on the surface and inside the phantom. It includes the simulation of high energy protons and neutrons in different layer of the phantom. The simulation used the extended Monte Carlo Code MCNPX [10] to transport neutron spectra and individual energy protons through the phantom. The thesis contains an introduction, four chapters and a conclusion.

The introduction gives an overview of the thesis and its structure. Chapter 1 presents a general background on space explorations and radiation risks, sources of space radiation and their complexity. Chapter 2 discusses the challenges facing the terrestrial and space neutron dosimetry. Chapter 3 is dedicated to Monte Carlo simulation and the methodology used in this work. Chapter 4 presents and discusses the results obtained in this study in comparison with the experimental measurements and, finally, the thesis ends with a conclusion which summarise the work and emphasize the main findings.

Chapter 1:
Space and Terrestrial Radiation

1.1 General Background

Humans first became aware of radiation on Earth at the end of the 19th century following Roentgen's identification of X-rays in 1895 and Becquerel's discovery of natural radioactivity in 1896. Over a hundred years later, terrestrial radiation is now well characterized and understood. The four major types of radiation on Earth are gamma (γ) rays, beta (β) particles, alpha (α) particles and neutrons (n). Terrestrial dosimetric concepts, techniques and instrumentation are all developed mainly for these radiations, with other forms of radiation such as protons and atomic nuclei only considered as special cases in large facilities for fundamental studies. Classifying radiation on Earth in such a way is reasonable since the four types of radiation have different properties and interact with matter differently. Table 1.1 summarizes the properties of terrestrial type of particles.

Table 1.1 Properties of the Four Major Types of Terrestrial Radiation

	α	β	γ	n
Mass	Heavy	Light	None	Medium
Charge	+2	-1	None	None
Range	< 0.1 mm	< 2 cm	High	High
LET	High	Low	Low	Medium
Penetration	Low	Medium	High	High

Space radiation was first identified on Hess's balloon flight in 1911 and Milikan later referred to this radiation as cosmic rays to reflect its extraterrestrial origin. Space radiation, outside the shield provided by the Earth's intrinsic magnetic field, is considerably different from that found on Earth. Therefore, its classification into four major types, as for terrestrial radiation, is not appropriate in a space context. Radiation in space is a mixed field, generally divided into two categories.

Given that, the radiation field in space is a mixture of many types of radiation particles, the concepts and instrumentation of terrestrial dosimetry have, thus far, been adopted for use in space. Radiation protection associated with human spaceflight is an important issue which becomes even more vital as both the length of the mission and the distance from Earth increase. Given the recent interest in long-duration space travel, in low-Earth orbit (for example on the International Space Station (ISS)), understanding of radiation issues is paramount. Protection of astronauts is divided into two main areas: (1) radiation dosimetry and monitoring and (2) radiation shielding. Considerable research and development (R&D) has been performed, and continues to do so, in both areas. Operational practices can also be used to limit the radiation dose, for example by selecting older crewmembers or by limiting the duration of extravehicular activity. Longer-term countermeasures might include pharmaceutical radio-protectants and screening to determine astronauts with high cancer risks, though neither is considered.

There are two types of health risk to the astronaut, acute and long term effect. The acute effects are such as vomiting, nausea, lethality and skin redness and the long term effect is the risks of cancer in the life time, depending on the age and gender of the person. The limitation of 30 days

is for the acute effect, and the career limitation is to protect the astronaut from the long term effects of radiation.

1.2. Radiation Dosimetry and Limits

Radiation dose is simply the energy absorbed per unit mass of the absorbing material and is measured in units of rad or gray (Gy) where 1Gy = 100 rad. Since dose measurements do not take into account the biological effects of radiation it is useful to introduce a second quantity known as dose equivalent, allowing for measurements of radiation damage of different types of radiation. Dose equivalent is defined as the dose multiplied by the relative biological effectiveness (RBE) and is measured in units of rem or sievert (Sv) where 1 Sv = 100 rem. The RBE is different for different types of radiation, depending on LET and penetration, and is often approximated by a quality factor (Q). Typical values of Q are 1 for γ rays and 1 – 20 for neutrons. Determination of radiation quality factors is difficult and has become an important issue in space radiation.

The following formula can be used to calculate the equivalent dose:

$$H_T = \sum w_R D_{R,T} \tag{1}$$

Where the w_R are the radiation weighting factor, $D_{R,T}$ are the average absorbed dose from radiation R in tissue T, and summation is over all the different types of radiation. The radiation weighting factors are presented in Table 1.2 [11]. However, recently it has been shown that the value for protons of energy greater than 2 MeV is too high, therefore the weighting factor has been changed to 2 [12].

Table 1.2 Radiation Wighting Factor (ICRP 60) [11]

Types and energy range	W_R
Photons, all energies	1.0
Electrons and muons	1.0
Neutron, energy $<$ 10 KeV	5.0
10 -100 KeV	10.0
100 KeV- 2 MeV	20.0
2 -20 MeV	10.0
$>$ 20 MeV	5.0
Protons, Other than recoils, E>2 MeV	5.0
Alpha particles, Fission frag. heavy nuclei	20

Dose equivalent can also be calculated using:

$$H_T = \bar{Q}.D_{T,R} \quad (2)$$

Where

$$\bar{Q} = \frac{1}{D}\int_0^\infty Q(L)D(L)dL \quad (3)$$

D*(L)* is the distribution in dose from the radiation environment at a point 10 mm deep within the ICRU sphere (a sphere of tissue-equivalent material with a diameter of 30 cm). *Q* is an approximation of the radiation weighting factor w_R and the new quality factor have been calculated depending on LET these values are given in Table 1.3[11].

Table.1.3 Quality Factor in Various Regions of LET [11]

Unrestricted LET, *L*, in water KeV/µm	***Q(L)***
< 10	**1**
10 -100	**0.32 L – 2.2**
> 100	**$300 / L^{1/2}$**

In space, to ensure the safety of the crew members and astronaut during the mission, the radiation dose should not exceed the acceptable radiation limits. Since there is little or no enough information about human or even on animal exposure to the space radiation, the health risk limitation are not known for certain. The radiation limitations, which are currently used are recommended by the National Council on Radiation Protection and Measurements (NCRP), are the same limitations established for low-earth orbit (LEO) operations. The GCR and solar proton flares are important for the latent carcinogenic effect and the limits for the dose are taken as a whole body exposure and it is assumed to be equal to the blood forming organs (BFO) dose. The BFO dose is calculated in five centimetre depth in tissue and the dose for skin and eyes is made using zero centimetre depth dose [13]. Current estimate for limits of radiation for whole body in

LEO are 25 cSv in any 30 days period, 50 cSv within any year and 100-400 cSv within a career depending on the age and gender [12].The limitation of 30 days is for the acute effect, and the career limitation is to protect the astronaut from the long term effects of radiation. Table.1.4 summarizes the ionizing radiation exposure limits for low earth orbit recommended by NCRP-98-1989 [14].

Table.1.4 Ionizing Radiation Exposure Limits for Low Earth Orbit Recommended by NCRP-98 [14]

Exposure Interval	**BFO Dose Equivalent (cSv)**	**Ocular Lens Dose Equivalent (cSv)**	**Skin Dose Equivalent (cSv)**
30-day	25	100	150
Annual	50	200	300
Career	100-400*	400	600

*Varies with age and gender

The astronaut cancer risk for a low LET is calculated by using [15]:

$$R_\gamma = K_\gamma D_\gamma \tag{4}$$

Where, D_γ is the dose with low LET and K_γ is the sensitivity coefficient of the low dose rate. To calculate the cancer risk for the high LET $D_\gamma$should be replaced by dose equivalent H_T in equation 1.

Also to calculate the radiation risk of cancer from galactic cosmic rays in particular organs, a Computerized Anatomical Man (CAM) has been used. The risk coefficient for radio-sensitivitie organs of the body which is recommended by ICRP60 has been used and is given in table 1.5

[11]. The total risk of radiation induced cancer is estimated to be 4% per Sv for an adult population [16].

Table.1.5 Low Dose-rate Cancer Mortality Risk Coefficients [11]

Organ/Tissue	**Probability of Excess Fatal Cancer[1] (Percent / Sv)**
Stomach	0.88
Colon	0.68
Lung	0.68
Bone Marrow	0.4
Bladder	0.24
Esophagus	0.24
Breast	0.16
Liver	0.12
Ovary	0.08
Thyroid	0.06
Bone Surface	0.04
Skin	0.02
Remainder	0.4
Total	**4.0**

Both the GCRs and SPEs are the sources of radiation outside the earth magnetic field, the contribution of different particle components from GCR and SPE to the dose equivalent for space radiation is shown respectively in Fig.1.1 (a) and Fig. 1.1 (b).

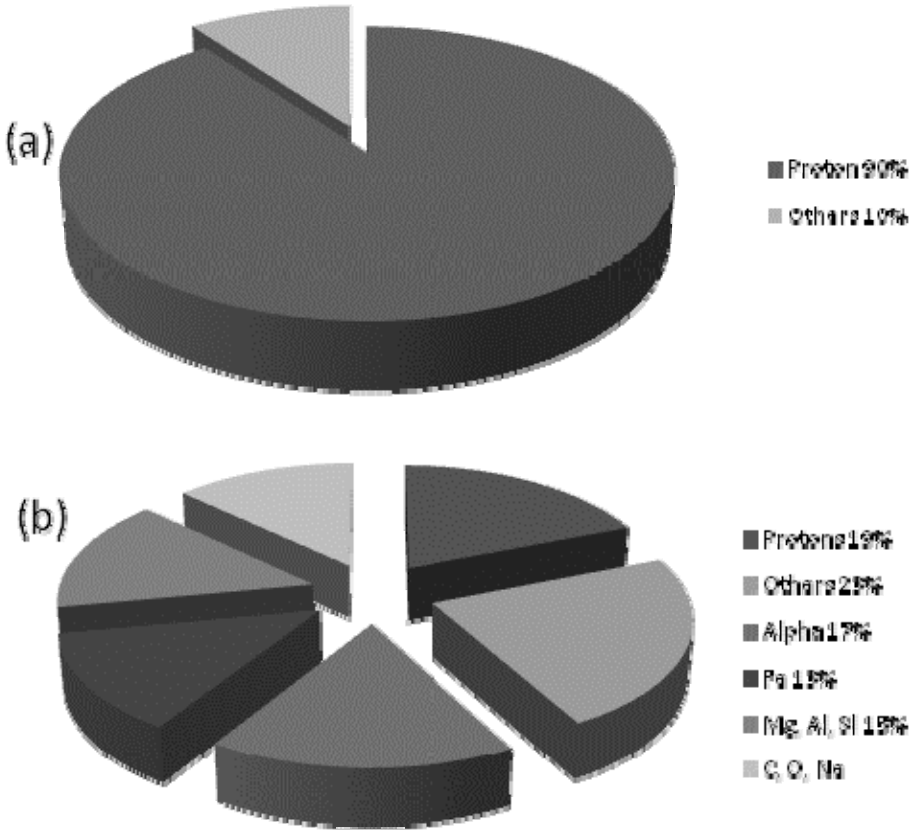

Fig1.1 Relative Contribution of Different Particle Components from (a) GCRs and (b) SPEs to Dose Equivalent for Space Radiation

When calculating the cancer risks there are a few sources of uncertainty [16]:

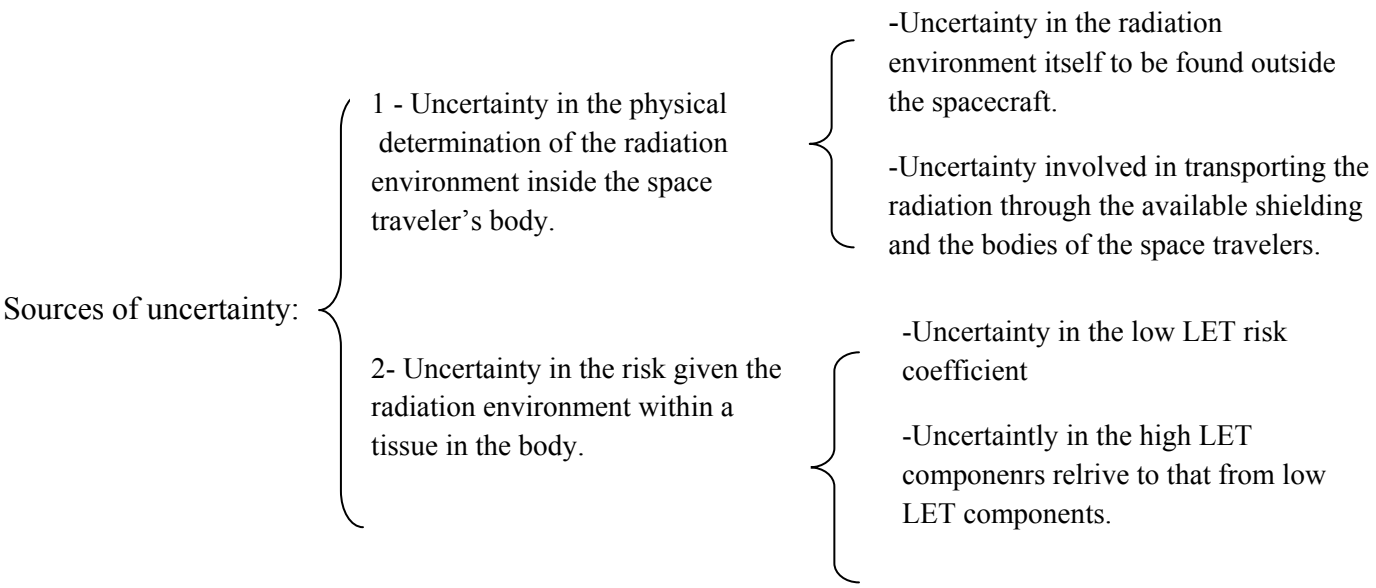

There are many unanswered questions regarding the biological effects of heavy ions, and more studies are needed to understand the potential effect of high and low energy charged particles to be able to protect the astronaut form exposure to these kinds of radiation.

1.3 Space Radiation Sources and Risk

Space radiation can be classified into two different groups: galactic cosmic rays (GCR) produced in supernova explosions outside the solar system and solar particle events (SPE) from the Sun.

Galactic cosmic rays are estimated to be composed of 86% protons and 12% α particles with the other 2% being composed equally of photons (γ and X rays) and atomic nuclei of various masses. Radiation due to GCR represents a constant background level in deep space, with the radiation traveling in all directions. Chronic exposure to the background GCR environment is mainly a matter of concern for stochastic effects, such as the induction of cancer, and late deterministic

effects such as cataracts. Damage to the central nervous system, usually a more immediate effect, is also possible. The most damaging radiation from GCR is those atomic nuclei which have high charge (Z) and energy (known as HZE particles) [17]. Unfortunately, the actual risks of cancer induction and mortality for the HZE component of the GCR spectrum are essentially unknown, but are the subject of numerous, current radiobiological investigations using laboratory beam, animal and cell culture systems.

GCR can have significantly biological impact, since the rate of energy deposition or linear energy transfer (LET) is very high. The abundances for the elements from GCR are shown in Fig.1.2a and it can be observed that the abundances is very low for heavier elements than helium, also the energy spectra of some of the important GCR elements are shown in Fig.1.2b, it can be seen that the energy peaks of these elements are near a few hundred MeV/nucleon and their fluxes are decreasing at both lower and higher energies ends, the peak of flux is around 30-40 MeV/nucleon, which is due to the Anomalous Cosmic Radiation (ACR).

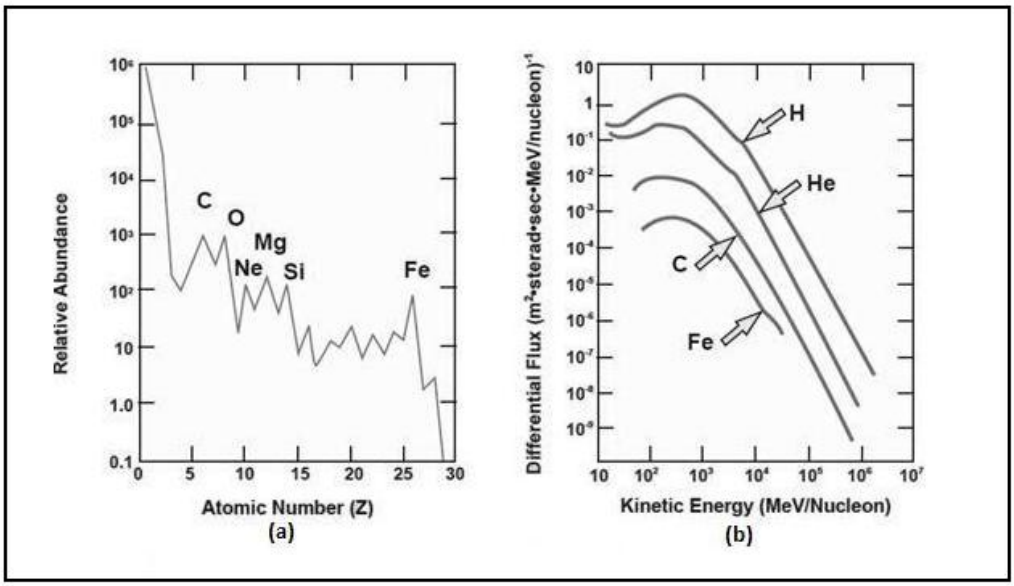

Fig.1.2 (a) Abundance of GCR and (b) Energy Spectra of some of the important Elements [17]

Solar particle events can be due to the solar wind, a continuous flux of low-energy protons, or due to solar flares, sporadic emissions from the Sun which follow the eleven-year solar cycle. Solar flares eject HZE particles and thus represent a much more serious threat than the constant solar wind. Although most SPE are too low in particle intensity or energy to present a health risk to spacecraft crew, very large events that may pose significant health risks can occur, especially during the solar maximum (the time of highest solar activity). The sporadic and unpredictable occurrence of these extremely large SPE is a major concern for mission planners and spacecraft designers. The peak flux of high energy protons is two to five orders greater than the GCR in time of SPE. After the SPE the peak flux can last for days, the periods of enhanced flux are shown in Fig.1.3. The energy of SPE may vary in each event, the fluxes for some of the past major event are shown in Fig.1.4.

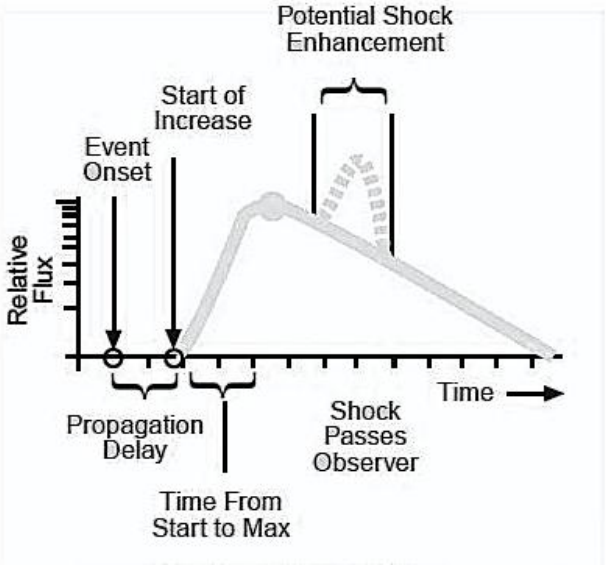

Fig.1.3 Chronology of SPE [17]

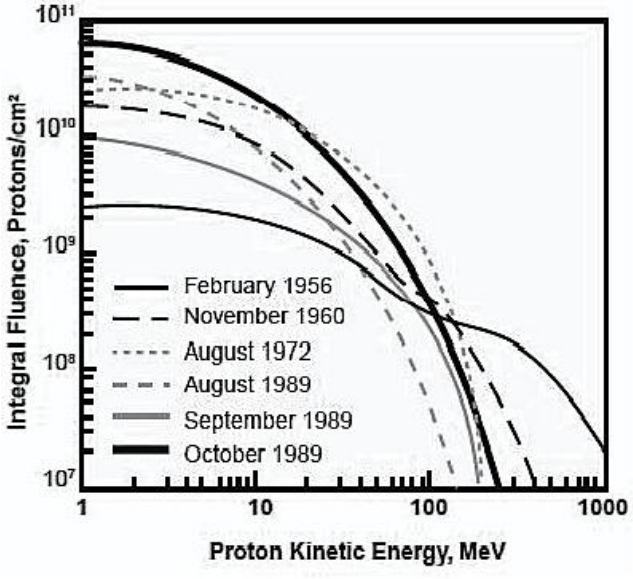

Fig1.4 Energy Distribution of Proton Fluxes for Past Major Events [17]

Effects on crew members include the possible manifestation of acute effects owing to the accompanying high doses of such radiations, especially acute radiation syndrome effects such as nausea, emesis, hemorrhaging, or even death. The large organ dose equivalents associated with these events can also contribute significantly to an increased risk of cancer induction and mortality in spacecraft crew.

The third source of space radiation is from the trapped electrons and protons in the radiation belt. The magnetic field of earth is thousands of kilometres out from surface of the earth, and it protects the earth from solar radiation. The sun produces particles which travel almost one million miles per hours; these stream particles are called the solar wind. The solar wind is mostly consists of proton and electrons. When the solar wind reaches the earth magnetic field, the charged particle traveling in the solar wind will be deflected by the magnetic field and they will move around the earth. The moving charged particles create a magnetic field themselves and this

will cause deformation in the earth magnetic field. The charged particles of lower energies leak into the earth magnetic field and change their path as they are traveling the earth magnetic lines and they will be trapped in Van Allen Belts [18]. The Van Allen Belts surrounds the earth and it consists of an inner belt and outer belt, protons are in the inner belt and electrons are in both inner and outer belts, Fig.1.5.

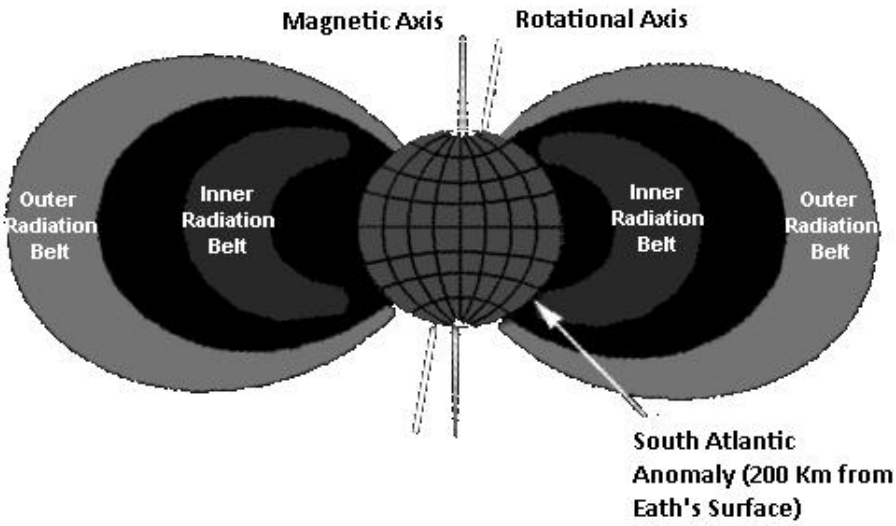

Fig.1.5 The Van Allen Radiation Belt [18]

The earth magnetic field is offset to the rotational axis, therefore the radiation belts that are centred on the magnetic field are not centered on rotational axis. In the region that the belt is closer to the surface of earth is called South Atlantic Anomaly (SAA) which is located near the

cost of Brazil. The belts altitude distributions and intensity changes with solar activity and daily seasonal changes, the proton fluxes can have energies of several hundred MeV. The energy distribution of the trapped proton and the SAA is shown in Fig.1.6.

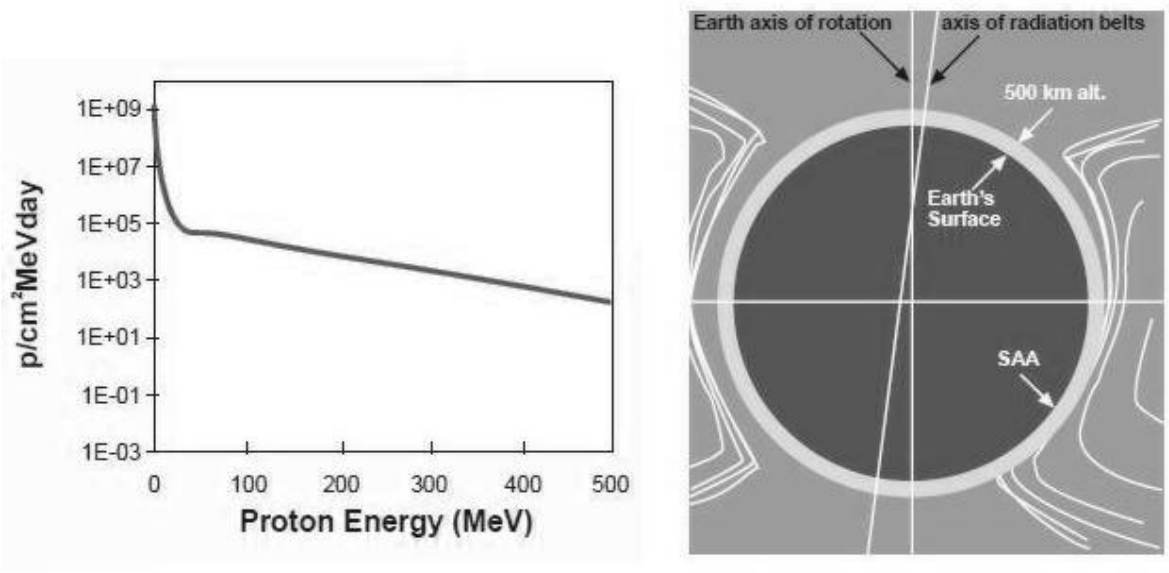

Fig1.6. Energy Distribution of Trapped Proton and South Atlantic Anomaly [17]

1.4. Space Neutron Radiation

Neutrons are one important component of the mixed radiation field created inside any space craft, the assessment of the neutron dose quantities remains an important part of any safety and space monitoring program.

The International Space Shuttle (ISS) is located in low earth orbit (LEO), which is beyond the protection of the atmosphere, but within the protection of the magnetic field. Radiation in the LEO is due to GCR and trapped radiation belt protons.

The primary high energetic particles, mostly protons, move very fast in matter and interact with different material to create secondary radiation. In space, when these high energy particles interact with the spacecraft shielding they produce a complex environment inside the space craft. Therefore, the radiation field created inside the space craft consists of charged and secondary particles. The most important secondary particles produced in the spacecraft shielding material are neutrons.

Neutrons are free of charge and have a high linear energy transfer LET. They can penetrate deep inside the human tissue without interaction with the atomic electrons and they get close to the nuclei and interact with it. Neutron interaction types are discussed in Appendix A.

1.5 Radiation Models to Predict GCR and SPE

To design any cosmic radiation model, there are some basic requirements that should be taken into consideration. These requirements are such as follows: the elemental abundances as a function of energy/ nucleon, the energy spectra of all the major elements, and the energy spectra of secondary particles should be correctly reproduced. The model should take the isotope composition into account and should have the capability to predict a reasonable accuracy of GCR spectra in future and extrapolate the current observation towards the outer heliosphere. Considering these requirements Mewalds suggested that the differential energy spectrum, *j (Z, E, t, r, q, f)* [2]can be expressed by:

$$j = j_0(Z,E) \times F_t(Z,E,t) \times F_r(Z,E,t) \times F_q(Z,E,t) \times F_f(Z,E,t) \qquad (5)$$

Where,

$j_0(Z,E)$ is the local interstellar spectrum of particle with charge Z, and $F_t(Z,E,t)$, $F_r(Z,E,t)$,

$F_q(Z,E,t)$ and $F_f(Z,E,t)$, are the time, radial, heliolatitude, and heliolongitude dependent function respectively.

One of the first models designed was called CREME, in addition there are four new models; reported in [2]. All of these new models are based on the standard diffusion-convection theory of solar modulation. These models include the most recent data on composition and spectra and they have significant improvements compare to the CREME model.

To calculate the expected energy spectra for SPE, Nymmik *et al* model has been used. The average spectra peak flux is given by [2]:

$$F(R)dR = C'(^{R}/_{R_{30}})^{-\gamma} \tag{6}$$

Where,

$$\gamma = 16.9[F(\geq 30)]^{-0.068} \tag{7}$$

Later Nymmik [2] modified this model and suggested that γ is an energy dependent parameter and it is given by:

$$\gamma = \gamma_0(^{E}/_{30})^{\alpha} \tag{8}$$

Where, γ_0 is the spectra index at E>30 MeV.

Chapter2:
Terrestrial and Space Neutron Dosimetry

2.1 Challenges in Neutron Dosimetry Research

Neutron dosimetry is a complex task and it is consider as the last frontier in radiation protection measurements. Since neutrons have a broad range of energies it is difficult to design an instrument that can cover all energies with acceptable resolution. Also, there is lack of knowledge on biological effectiveness of the secondary particles produced by high energy neutrons. It has been found that the neutrons with the energy range of 0.1 to 150 MeV have significant contribution to the total dose [1]. At the same time there is a very little experimental data on dose measurements from high energy neutrons.

From instrumentation point of view, personal dosimeters can be divided into two groups: through direct reading, which can be active or passive devices, and though remotely read passive devices. The remotely read passive devices have the advantage of immunity from most types of failure that might interrupt a measurement, but it is not suitable for long duration. Therefore it is not a good space dosimeter. Also the remotely passive dosimeters are good for low neutron measurement but not suitable for high energy neutrons and they cannot differentiate between neutrons and other charged particles. The direct passive and active dosimeters are important for space radiation protection program; these devices have the ability to monitor the radiation dose in real time, so that the astronaut can monitor the exposure dose during different activities and at different locations of the space craft. The minimum requirements for personal dosimeter, the sensitivity and the neutron energy range, varies by the environment that it will be used in.

At present, there is no reliable neutron personal dosimeter to measure the dose in space environment. Therefore, It is essential to validate the radiation transport models for the space environment. To do so, two approaches can be used; neutron spectroscopy and identification of the fractions of the high LET dose delivered by short and long range particles.

The fraction of the dose produced by light charge particles is not a complete substitute for secondary neutron spectroscopy, however; the fraction of the dose produced by light range ions can be compared for consistency with the calculated neutron dose. The advantage of the devices for lower energy particles is that the detector is easy to develop, light weighted and compact. But the detector for neutron spectrometery over the range of 0.1 to 150 MeV [1] presents a serious challenge. In addition, the detector would be large and heavy. Although this kind of detectors is not a routine part of the radiation protection program, the large weight is not prohibited. The size of the detectors are important component only when it comes to measuring the dose in specific organs, the detector should be small enough so that it could easily be inserted inside the tissue equivalent phantom. However, the sensitivity and discrimination between neutrons and other particles mainly protons are required.

The other concern of neutron measurements is due to testing and calibration of neutron instrumentation. Different types of neutron sources are needed during the development of neutron spectroscopy to calibrate the system, especially for high energy neutrons. There are a few facilities for monoenergetic neutron sources, which allow the evaluation of the detector in mixed radiation environment. Also there are high neutron energy sources, which produce spectra with about half of the total neutron fluence in a relatively narrow peak at the specific energy, and the remainder in a continuous distribution at lower energies [1].

2.2 Ground Based Research on Neutron Space Dosimetry

There are many ongoing ground-based researches on neutron production especially on fast neutrons. These measurements are used to predict the production of neutrons from interaction of GCR like particles.

There are two types of ground-base experiments; cross section on thin target measurements, and thick target measurements. On thin target experiments, measurements provide information on the physical properties of neutron interaction with a target and neutron spectra created by a projectile at one specific energy with no contribution from secondary interaction in the target. On the other hand, with the thick target, experiments are used for a quantitative evaluation of different modeling codes such as production from secondary interactions with target nuclei, and neutron flux attenuation within the target.

The ground base neutron measurements is based on the production of neutrons from interaction of SPE and GCR like particles. Target masses that are used should include all the possible shielding materials as well as tissue components. The experimental results for neutron production from proton interaction and heavy ion interaction are available in literature. The cross section data is used in the development of radiation transport codes, while thick target data provide are used for testing the codes, in terms of their accuracy in modeling secondary interactions in the target.

First set of data from the ground base experiments is from neutron production resulting from proton interaction, these set of data is very important, since protons make up about 90% of the GCR flux [19]. In a research measurement of neutrons from proton induced interactions was measured with thin and thick target measurements. The measurements have been made with

proton energies of 113, 256, 318, 597 and 800 MeV protons on targets of Be, B, C, N, O, Al, Fe, Pb and U at angels of 7.5, 30, 60, 120 and 150 degrees. These measurements cover most of the data needed to predict the neutron production from induced GCR like protons [1].

Using the data for neutron yields from 256 MeV protons stopping in Aluminum 20 cm long and a density of 54 g/cm^2, the dose equivalent was calculated for neutron of energy above 0.5 MeV. Percentage of the total neutron flux and the dose equivalent is given in Table 2.1 [1].

Table.2.1 Percentage of the Total Neutron Flux and the Dose Equivalent yields from 256 MeV Protons Stopping in Aluminum 20 cm long and a Density of 54 g/cm^2 [1]

Energy Range, MeV	% Neutron Flux	% Dose Equivalent
0.5-1	13%	6%
1-5	38%	28%
5-10	13%	9%
10-20	7%	5%
20-50	9%	12%
50-100	13%	25%
100-200	6%	13%
>200	1%	2%

The second set of ground base data is from neutron production from heavy ion interactions. Helium makes up about 12%, and HZE makes about 1% of the GCR flux, however; in the calculation it has been shown that about 15% of neutron flux behind 50 g/cm^2 of water and another 16% of neutron flux comes from helium and HZR, respectively. Also, the same calculation was done behind aluminum shielding and it was predicted that 12.5% of neutron flux comes from Helium and 6% come from HZE interactions [1]. In the case of neutron production

from interaction of heavy ions unlike the protons, there are not that many references. And there are a few experiments in regards to thin target neutron cross sections.

One experiment was done using a 435 MeV/nucleon Nb beam that was stopped in a target of 1.27 cm thick aluminum and 0.51 cm thick Nb. The data was taken with the use of four thin detectors which were placed in different angles. The neutrons spectra produced in these experiments at 3^o, 9^o, 16^o, 28^0, 48^0 and 80^0 is shown in Fig.2.1 [19].

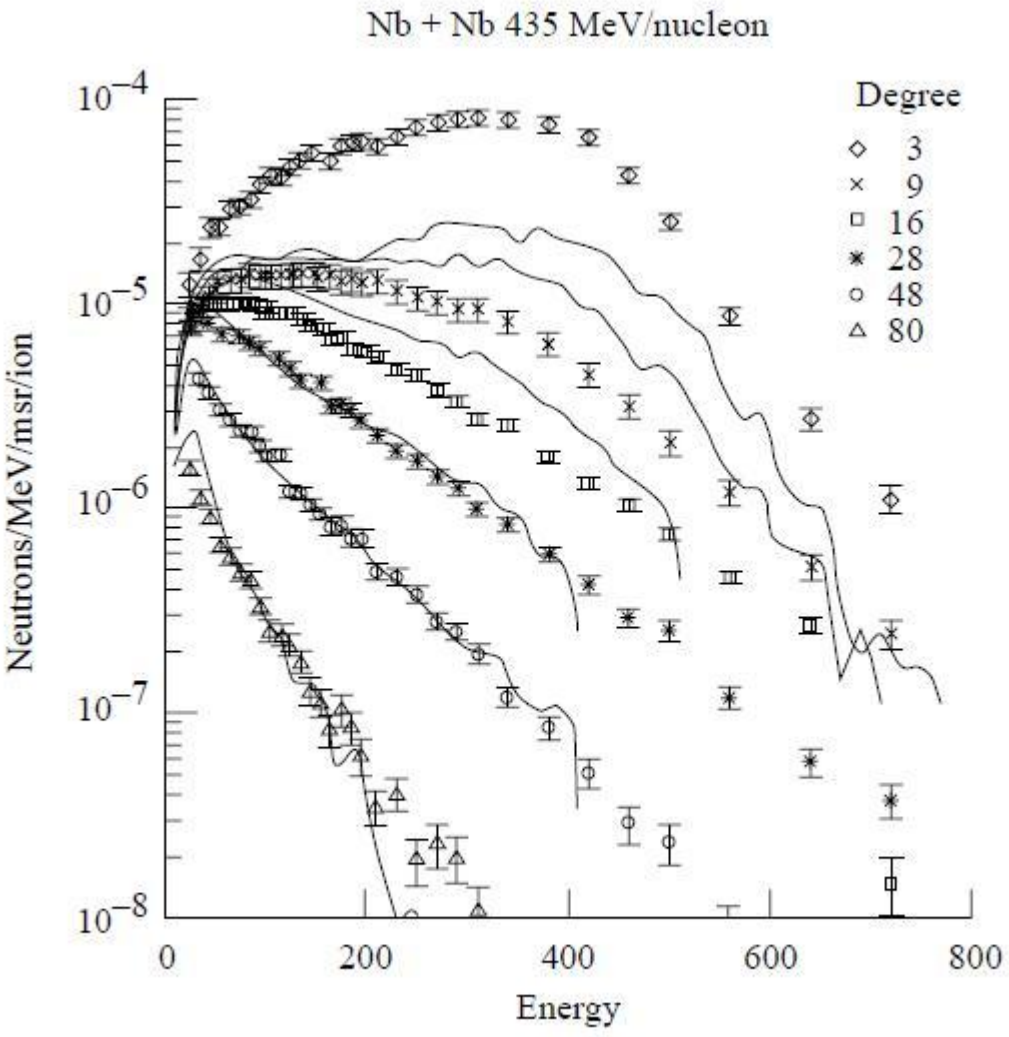

Fig.2.1 Neutron Spectra from 435 MeV/nucleon Nb at indicated Angels [19]

Another experiment was done with thick target neutrons yield from 155 MeV/ nucleon He+Al and from 155 MeV/ nucleon C+Al, also cross section measurements was conducted for C+Al at 155 MeV/nucleon and 75 MeV/ nucleon. Neutron detectors in this experiment were placed at 4° to 160° . The results are shown for 10, 30, 60, 90, 125, and 160 for the 155 MeV/nucleon C+ Al systems Fig.2.2 [19].

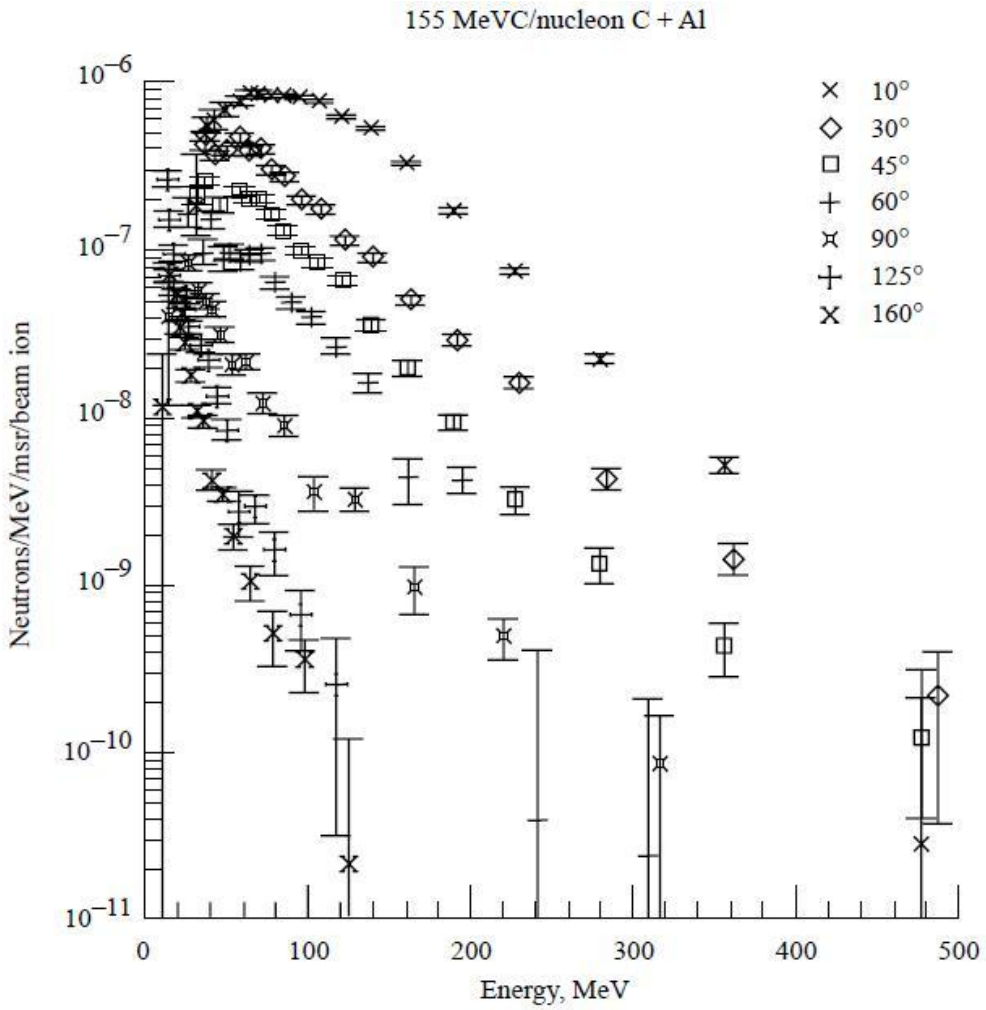

Fig.2.2 Neutron Spectra from 155 MeV/nucleon C+Al at indicated Angels [19]

Furthermore, there are varies types of detectors that are being developed for the neutron dosimetry. The neutrons detectors which are developed for the use in space environment are also being tested in the facilities available on earth.

One of the available facilities for the calibration of dosimetric devices in high energy neutron radiation fields is available at CERN. These reference fields are similar to the cosmic ray field at 10-20 kilometre altitude [20]. A positive hadron beam with momentum of usually 120 GeV/c hits a 7 cm diameter copper target, and the secondary particles produces in the target are filtered by 80 cm concrete or 40 cm iron [20], from these shielding a uniform radiation field which is mostly neutron will be produced. The large range of the spectrum radiation fields created are suitable for testing instrumentation under different conditions.

In addition, there are several passive and active detectors that are being tested at CERN facility, such as; Tissue Equivalent Proportional Counter (TEPC). GM-Counter, bubble detectors, scintillator based dose-rate meters and others.

2.3 Neutron Dosimetry Investigation in Space

Neutron dosimetry is a challenging task on earth and it is more challenging in space environment because of the complexity of the mixed field. There are many different research group conducting different radiation experiments in space environment. Also, there are different detectors that are being used and developed in order to measure the neutron dose, specifically, aboard the international space station (ISS) and to predict the exposure rate to the astronaut.

Neutrons present an important component of space radiation and the neutron dose contribution has been estimate to be 15 to 35% of the total equivalent [21].

In the next section there is a brief review of some of the available neutron measurements in space environment and some ongoing neutron investigation. In addition, different detectors and technologies used for characterizing space radiation and neutron dosimetry in particular are discussed.

2.3.1 Measurements of Neutron Dose in Space

H. Matsumoto has investigated real time neutron measurement using Bonner Ball Neutron Detector (BBND) during Space Shuttle Mission STS-89 and he reported that the dose equivalent rate for neutrons of 1-10 MeV is about 75μSv/day. However the secondary neutrons in space shuttle ranges from thermal to 100 MeV and their contribution is from 10 to 35% of the total dose equivalent [4].

The used detector BBND is made of six ^{3}He proportional counter, which is sensitive to thermal neutron. The ^{3}He proportional counter detects neutron through the nuclear reaction:

$$^{3}He + n \longrightarrow {}^{1}H + {}^{3}H + 765\ KeV \qquad (9)$$

To measure the neutron energy spectrum the unfolding method was used and the count number C_i of the i^{th} counter can be expressed by:

$$C_i = \int_0^x R(i,E)\Phi(E)dE \qquad (i=1, 2, ...n) \qquad (10)$$

Where, $\Phi(E)$ the neutron spectrum at the detector, i, and $R(i, E)$ are the response function of the detectors. The $R(i, E)$ can be find experimentally or theoretically, and the value of $\Phi(E)$ can be obtained by unfolding techniques and counting for C_1-C_n. In these study the response function $R(i, E)$ was calculated by another similar ^{3}He proportional counter and $\Phi(E)$ was obtained by cumulative measured result by J. E. Keith et al. The unfolding technique was based on the

unfolding code SAND-II. The conversion coefficient for calculating the dose equivalent was taken from ICRP-51 report. The result from the analysis of the rate/dose equivalence roughly agreed with the values obtained using space radiation environmental model (AP-8), HERMES and other models. Also the average value obtained in the study agreed well with the energy spectrum obtained using STS-28 by J. E Keith, in August, 1989 [4].

V. I. Lyagushin in his measurements of neutron energy spectra on the MIR Orbital station has generalized the results of Russian measurements. He has reported neutron spectra from three energy ranges: from thermal to 10 KeV, from 10 KeV- 20 MeV and from 20 to 400 MeV. The measurements of these three ranges were taken using four different techniques: nuclear photo-emulsions (NPE), fission foils (FF), recoil protons (RP) using an organic scintillator, and a CsI crystal. He obtained total neutron dose equivalent of 76-130 μSv/d inside MIR station [5].

In addition, V. I. Lyagushin concluded that the largest contribution of neutron fluxes and the dose equivalent rate is generated by the neutrons of 100 KeV to 100 MeV [5], and the number of neutron and the dose increases are dependent on shielding and spacecraft mass.

There are number of different detectors which are being used in space environment for neutron dosimetry. L. A. Braby discusses the use of a tissue equivalent proportional counter (TEPC) as a neutron detector, TEPC are active detectors and are used in different areas for neutron dose measurement [6]. The advantage of using this type of detectors is that it can be relatively small, light and it does not require high power. The TEPC is sensitive to all radiations that are produce dose in tissue. Therefore, he used two proportional counters: a carbon proportional counter to overcome the problem of distinguishing between neutrons and charge particles sources of radiation, and one typical TEPC.

The bubble detectors are used in space missions since about 1989, H. Ing in studying neutron field in space using bubble detectors reported that neutrons above 10 MeV contribute half of the dose equivalent [7]. These measurements were carried using bubble detectors on the Bion-9,-10,- , Mir, STS-81, -84, - 86, -89 and -91. However, the bubble detector has an unknown response for neutrons above 20 MeV. The dose equivalent measurements on the space shuttles were from 80 to140 μSv/d. The dose contribution from neutrons from 10-20 MeV was about 23%. In this work it will be referred to bubble detector since our comparison will be based on the measurement done by bubble detectors.

In a study conducted by Gautam D., the measurement of neutron of energy 1-14 MeV were made by recoil proton measurements in nuclear emulsions and Bonner sphere [8].

In proton measurements in nuclear emulsions, the neutron energy spectrum is constructed using the kinematics of elastic scattering from the measured proton spectra. In the measurements with Bonner sphere, four Bonner sphere with Au foils in different shuttle flights were used to drive the neutron spectra for each flight. The neutron spectra were derived assuming that its shape was a combination of the albedo spectrum and secondary neutron spectrum calculated by Armstrong [8]. The Bonner sphere cannot resolve for high energy neutrons, therefore, the spectra for neutrons above 14 MeV is not based on real measurements and is found by using the power law extrapolation. Moreover, by using the conversion factor for fluence-to-dose from ICRP-51, the energy spectra were converted to dose equivalent. The data from the Bonner sphere are not consistent compared to the data obtained by the proton recoil measurements, since the flights with Bonner sphere were done at the time of a strongest solar maximum; also the location which the Bonner sphere was located in the lower shuttle shielding.

Gautam D. and his colleagues reported the neutron absorbed dose using ^{6}Li [8] and the rate of neutron capture is given by:

$$R = N \int \sigma(v)\varphi(v)dv = N\sigma_0 \int \rho(v)dv \tag{11}$$

Where, N is the number of interacting nuclei, σ is the cross section, ϕ is the flux, and ρ(v) is the neutron density with velocity v. Also, the ^{6}Li cross section for the neutron energy of 0.01 eV to 200 KeV display a 1/v dependence, the response R would be the same for varying averaged flux, therefore the R can be expressed by[8]:

$$R = \varphi_0 - \varphi = \varphi_0(1 - e^{-n\sigma a}) \tag{12}$$

Where, Φ_o is the incident flux of neutron on a slab of thickness a, and Φ is the final flux from the back surface of the slab. If the flux is coming from different directions then the effect must be integrated over all directions:

$$\varphi = \int e^{-n\sigma a\, sec\theta} \sin\theta \, d\theta \tag{13}$$

Knowing that the cross section is dependent on the energy of neutrons, the dose measurements cannot be simply interpreted, therefore the calibrations of these detectors are needed both for mono energetic and neutron spectra. The calibration of these detector where done in CERN Reference Neutron field. Also using the fluence-to-dose conversion factors the cumulative absorbed dose and dose equivalent was calculated. The measurements found using these passive detectors showed that the neutron contribution of energy less than 1 MeV to the total dose equivalent is less than 5%, and neutrons of 1-10 MeV dose equivalent contribution is 50% of the total dose equivalent. The dose measurements depend on the altitude, solar conditions and shielding locations [8].

In another study by R. Machrafi, as part of the Matroshka-R project, reported that the internal and external dose measured on the spherical phantom with the use of space bubble detectors (SBDs) are about the same. For these measurements a total of 16 bubble detectors with the sensitivity of 140 to 200 bubbles/mSv were used for duration of about 5 days. Also to simulate the human body a spherical phantom was used. During the experiment the bubble detectors were located in different locations of the International Space Station, outside and inside of the phantom [9].

2.3.2 Neutron Detectors and Dosimeters in Space

There are many different technologies being developed to characterize the space radiation environment for the ISS. NASA, Russian Space Agency (RSA), European Space Agency (ESA), National Space Developments Agency of Japan (NASDA) and Canadian Space Agency (CSA) are the ISS partners and they are developing technologies for ISS to help characterizing and monitoring the space radiation environment.

NASA, instruments are flown on board the ISS and allow the ground support personal to evaluate space radiation environment. The instrumentations that are used by NASA are as follows; tissue equivalent proportional counter (TEPC), extravehicular charge particle directional spectrometers (EV-CPDS), Intravehicular charge particle directional spectrometers (IV-CPDS), and Passive Dosimetry Systems (PDS), Crew Passive Dosimetry (CPDs), Radiation Area Monitors (RAMs) and High Rate Dosimeters (HRDs).

TEPC has a capability of measuring a complete LET spectrum and it can provide the absorbed dose rate and the dose equivalent rate. The absorbed dose rate and the equivalent dose rate can be expressed respectively by [21]:

$$D=k \int J(y)\, y\, dy \quad (14)$$

$$\dot{H} = k \int J(y)\ q(y) y\, dy \quad (15)$$

Where,

J(y) is the differential lineal energy spectrum, y is the lineal energy, k is the proportionality constant related to the unit of measurement, and q is the quality factor taken from ICRP-60.

The TEPC is a right cylindrical detector which is surrounded by tissue equivalent plastic. For calibration of these kinds of detectors a ^{137}Cs $\boldsymbol{\gamma}$- ray source and ^{252}Cf neutron source were used on the ground. Also the TEPCs were tested in CERN-EC reference flied facility and at Los Alamos Nuclear Service Center (LANSCE). From experimental results it was shown that the radiation risk will increases by up to a factor of two behind a shielding thickness of about 5g.cm^{-2} [20], this is due to the production of secondary particles and the change in the lineal energy spectrum from the primary interaction with the shied material. TEPC also is used for development of space radiation transport models since it can determine the integral liner energy spectrum of the space radiation field.

The CPDs are worn during the space mission by the crew for the documentation recorded on the absorbed dose, the RAMs are compact, and are used in different locations to monitor the radiation, and the HRDs are self indication ion chambers which are used during high dose rate [21].

Russian Space Agency uses both onboard radiation monitoring for operations and an individual dosimetry control system. There are different types of detector and hardware that are being used by Russians, R-16 radiation detectors, Radiation Monitoring System and passive dosimeter for

individual controls. RSA has provided significant experimental results on GCR, SPE and radiation belt. Also, by using different methods such as; nuclear photoemulsion, fissionable foils, recoil proton and CsI-TI crystal, Russians measured and reported the neutron spectra inside and outside the MIR-Station. Furthermore, to provide better characterization of the space environment RSA are working on the Matroshka-R experiments on board the ISS and this work is a part of such effort.

The other partner of the ISS are the European Space Agency, has suggested using passive TLDs, active silicon detectors and biological dosimetry for personal monitoring. Also, to monitor the space environment, they have been using different passive and active detectors located in different locations. Some of the detectors being used by ESA are Lithium fluoride (LiF) TLD chips, polycarbonate detectors, and silicon Dosimetry Telescope (DOSTEL). ESA has been involved in several missions on MIR, in order to measure the radiation environment using several passive and active detectors, and the measurements of the dose equivalent has been found to be in the range of 576-767 μSvd^{-1} [21]. The ESA has been involved in Matroshka-R phantom experiments; also they are working on development the Dosimetric Mapping experiment.

National Space Development Agency of Japan, are involve in both personal and environmental space monitoring. The detectors that they are using for personal monitoring absorbed dose are TLDs and Plastic Nuclear Track Detectors (PNTD). Also for area and personal monitoring, a Real time Radiation Monitoring Device (RRMD) is being used to measure the absorbed dose and silicon detectors is used for LET spectrum measurements. For neutron measurements, a neutron spectrometer system (NeM) has been developed, NeM consists of BBND for neutrons in the energy range from thermal to 10 MeV, five different polyethelene wall and He-3 proportional

counters are being used, and for the neutrons of higher energy the NeM uses a Scintillation Fiber Detector (SFD).

The Canadian Space Agency has been contributing to space science and research, and has supported the development of devices for real time active monitoring, and personal neutron dosimetry. The technologies that are used by Canadian are metal oxide semiconductor field-effect transistor (MOSFET) dosimetry and Bubble detectors.

The MOSFET is used for monitoring the real time absorbed dose to the skin, eye and blood forming organs measurements. It has been calibrated and tested by Russian investigators on several experiments onboard the Bion-10 satellite. It has been discussed that better calibration is needed for this technology and ground based testing is necessary before using these type of detectors on board. Furthermore, the MOSFET has been used for a crew exposure assessment on the Shuttle and MIR-Starion in the past and it will be continued to be used aboard ISS.

The other technology being used by CSA is the bubble detector technology which was developed in 1984 for terrestrial neutron dosimetry and due to the need of proton, neutron and HZE particles measurements in space, the use of this detector in space was needed, since it is the only passive detector that could easily provide neutron dose equivalent measurements. The BD was then used in several space mission such as; Bion-9, Bion-10, MIR-Station and in several other experiments. Since bubble detector has been used for experimental study of the neutron dose and our simulation will be compared to the data obtained with such instrumentation. A detail description of such passive dosimeters is given in the next section.

Bubble detector is a passive personal neutron dosimeter, which was originally created by Bubble Technology Industries Inc (BTI) for terrestrial neutron dose equivalent measurements in 1984

[21] and in 1989 bubble detector was used by Russians to measure neutron dose equivalent in space missions.

Bubble detector consists of superheated liquid in the form of superheated droplet dispersed in a transparent, firm polymer gel. The superheated liquid has stored mechanical energy, due to the interactions of neutron with this superheated droplet the stored energy is released and visible bubbles form in the detector. The BD is reusable and it can be made for different sensitivity and is totally insensitive to gamma rays [21]. By changing the composition of the supper heated fluid, the detector can response to different energy thresholds. A firmer polymer than the BD was used to create so called Space Bubble Detector (SBD). This allows to the slower bubble formation so that the detectors could be used for longer missions. The SBD are reusable and the bubbles can be recompressed by a piston which is attached to the top of each detector. The SBD is shown in Fig.2.3 [22].

Fig.2.3 Space Bubble Detector [22]

For bubble formation in a liquid, there is a minimum energy required, and to form a bubble, the critical radius is an important parameter given by [7],

$$r_c = \frac{2\gamma}{\Delta p} \tag{16}$$

Where $\boldsymbol{\gamma}$ is the surface tension of the liquid and Δp is the degree of superheat and can be calculated by the vapour pressure of the superheated liquid in the droplet minus the pressure that exerted on the elastic polymer. The minimum energy is given by [7],

$$E_{min} = 16\pi\gamma^3(\Delta p)^2\left(\frac{1+\frac{2}{3p_vH}}{M\Delta p}\right) \tag{17}$$

Where P_v is the density of the vapour, H is the molar heat of vaporization and M is the molecular weight.

To calibrate the bubble detector, AmBe source has been used and in some cases ^{252}Cf source are used. The response from the two sources vary by less than 10% [7]. The AmBe source with neutron emission rate of $1.13\text{x}10^7$ s^{-1} and a conversion coefficient factor of $4.11\text{x}10^{-4}$ $\mu Sv.cm^2$ (from ICRP-66) was used at Chalk River to calibrate the SBD, the sensitivity of the bubble detector is given in bubbles/μSv. The bubble detectors are calibrated for personal dose equivalent $H_p(10)$.

Chapter3:
Monte Carlo Simulation and Results

3.1. Monte Carlo Transport Code Description

The Monte Carlo method was developed at Los Alamos National Laboratory during the Manhattan Project in the early 1940s. This method is mostly used to perform radiation transport calculations. MCNP (Monte Carlo N-Particles) is a general-purpose Monte Carlo radiation transport code for modeling the interaction of radiation with matter and the code can perform coupled neutron, photon and electron transport calculations. Monte Carlo N-Particle extended (MCNPX), is three dimensional and time dependent version of MCNP, and it includes other particles physical models and reduction techniques as well as neutron, proton and electron [10].

MCNPX has been used for different applications such as; nuclear medicine, nuclear safeguard, accelerator, space and more. MCNPX is an extremely useful tool for shielding or energy deposition calculations. For detector design, the code is generally used to optimize the design of the detectors before they are built. This saves a lot of experimental work on prototypes [10]. The code is written in different computer operating systems; Fortran 90 runs on PC Windows, Linux, and UNIX platforms.

MCNPX code is consisting of an input file which contains several files that are provided as part of the code package, generated by problem runs, or user-supplied. This section focuses on the user-supplied INP (the default name of the input file) file which describes the problem to be run [10].

The code structure is usually as follows; Geometry specification, materials selection and properties, location and characteristics of the source, and output desired (tallies).

The geometry is defined by cells, which are defined by intersections, unions, and complements of the regions and contained user material. Finally using intersection of the surfaces, different cells can be created. A created cell can have material or it can be void. The importance is the sensitivity of each cell to one or more particle type and it is different for each particle. The importance of zero for a cell means that the particle will not be followed in the cell. Therefore the geometry should be surrounded by an importance of zero to avoid going 'forever'. The material cards provide information of the elemental (or isotopic) composition, and the cross section compilations to be used. The other part of input file is, tally card used to specify what type of information the user wants to gain from the MCNPX calculation. There are many different types of tallies, such as; flux in the cell, flux on the surface, energy deposition in cells and etc... Finally the source specification 'SDEF card' is used to characterize all the sources in the problem. The SDEF card provides information about the type, energy and the location of the sources.

The Monte Carlo transport codes have been used in many research fields related to space radiation, where they played an important role for simulation and calculations of space radiation dose.

In this thesis, the MCNPX code has been used to characterize the neutron fluxes inside and outside of a spherical phantom currently flying aboard ISS. The specification of the geometry, which is a 3D configuration of the phantom model, was created in an input file. The geometry consists of seven surfaces defined as spheres with different radiuses. The region between two consecutive spheres has been defined as a cell (volume). The radius of each cell presents a defined depth in of the phantom.

Martial card have been created to fill each cell with a tissue equivalent material, which consists of the isotopic composition of the material in the real phantom and information about the cross section used for the simulation. There are different list of cross section available by MCNPX. In this work the cross section used is .60c for neutron transport inside the phantom.

The neutron source was defined to be a point source; also source information card (SI) and source probability card (SP) were defined, where, SI is the energy spectrum of neutrons, and SP is the probability of having neutron in that energy.

For the output, the neutron flux was calculated using the tally F4. The average flux in each cell is then calculated in the unit of #/cm^2. The definition of the F4 tally is as follows; suppose a particle of weight *W* and energy *E* makes a track length *T* within a specific cell of volume *V*. This segment makes a contribution *WT/V* to the flux in the cell. The sum of the contributions is reported as the F4 tally in the MCNP output. The F4 tallies can be giveb by [10]:

$$\text{F4}=\frac{1}{V}\int_V dV \int_E dE \int_{4\pi} d\Omega E\Phi(r,E,\Omega) \tag{18}$$

Where, Φ(r, *E*, Ω) were the energy and angular distribution of the fluence as a function of position.

Normally the MCNPX run is terminated when a certain number of particle histories (NPS) have been run or a desired computing time (CTME) has been exceeded. In this work, 10^8 events have simulated for each run. A sample of MCNPX code is given in Appendix B.

3.2. Visual Editor

The MCNP Visual Editor is a graphical user interface for the MCNP computer code; it allows the user to create the geometry directly from the plot window. It also provides different views of the geometry including 3D. Fig.3.1 shows the spherical phantom generated in Visual Editor of MCNPX. This phantom has been used in this simulation.

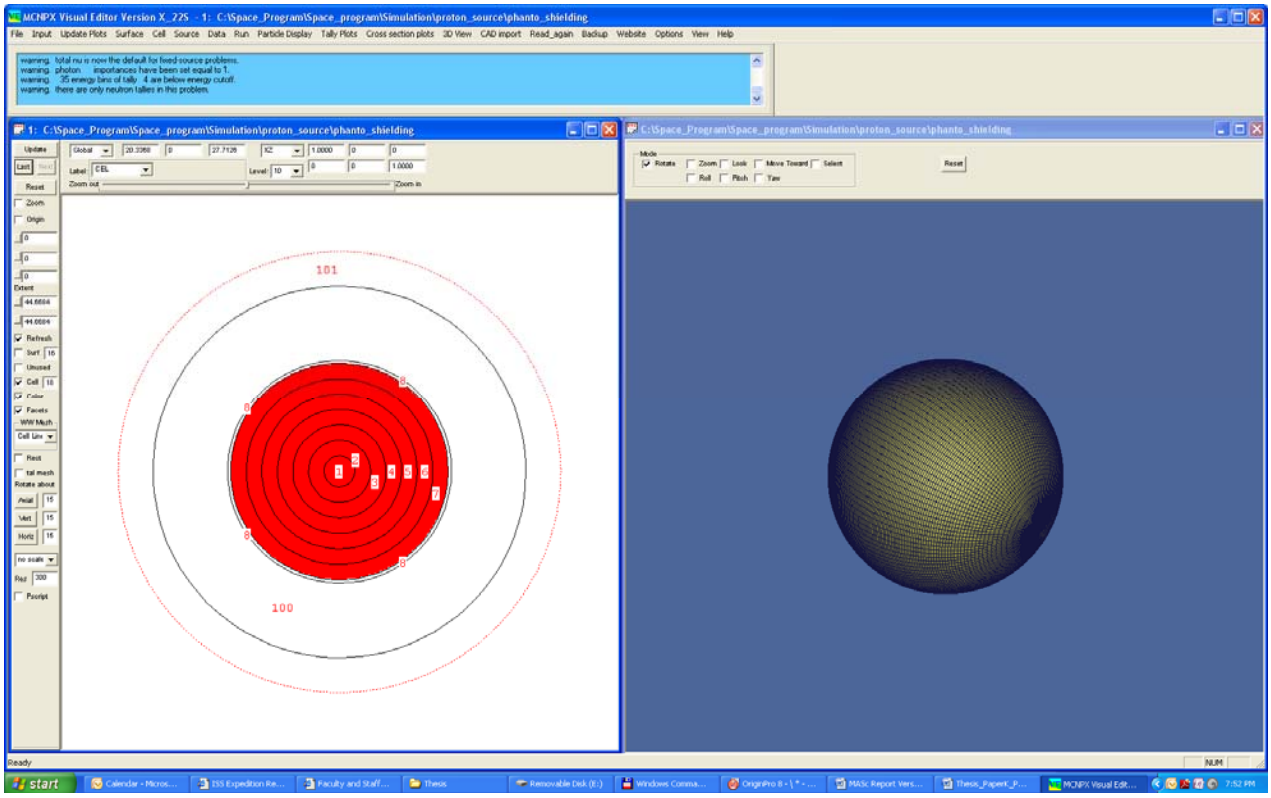

Fig 3.1 Spherical Phantom Used in this Work and Generated in Visual Editor of MCNPX

In this work, Monte Carlo codes have been used to transport neutron and protons with different energies through the spherical phantom currently flying aboard the international space station. More information about the used phantom will be given in the next section.

3.3. Methodology Description

As it was mentioned earlier, the measurement of the neutron dose in space is extremely difficult task. Due to the large uncertainty on the neutron dose measured aboard the international space station reported by different research groups and the lack of data on the internal and external doses inside and outside the phantom, it is paramount to approach the problem differently by using extensive simulation with different codes. This chapter discusses the methodology used in this work to clarify, through the simulation, two major issues namely, the neutron generation in the tissue equivalent phantom and the relation of the internal to external dose. It should be mentioned that experimental investigation has been done during, what called, Matroshka R experiment that includes a spherical phantom. Thus, for the purpose of comparison, the same phantom has been used in this thesis.

3.3.1 Matroshka- R Spherical Phantom

The radiation effect on human organs has been a concern for many years; therefore tissue equivalent phantoms are being made for the purpose of dose radiation measurements. The Matroshka-R phantom is made of human tissue equivalent material, and is used to estimate the dose in the ISS environment. This spherical phantom has a diameter of 35 cm; it has 13 tissue-equivalent slices and it is made of 8.6% Hydrogen, 2.6% Nitrogen, 32.3% Oxygen and 56.5% Carbon, and with a mass of 32 Kg. Also the phantom has radial holes specially designed to fit the SBD for neutron dose measurements. Fig.3.2 shows a picture of the Matroshka-R spherical phantom used in this work.

Fig 3.2 Matroshka-R Spherical Phantom

3.3.2 Monte Carlo Simulation Models

To estimate the neutron production inside the spherical phantom described above, two Monte Carlo models have been built: the first model has been built to transport a measured neutron spectra in space through the phantom, while the second model has been built to transport high energy protons with different energies.

The phantom model has been built in MCNPX and it consists of the same material and size as the Matroshka-R phantom. The phantom was simulated to have seven level of depth where neutron fluxes at different levels have been calculated. Fig.3.3 represents the phantom created in MCNPX.

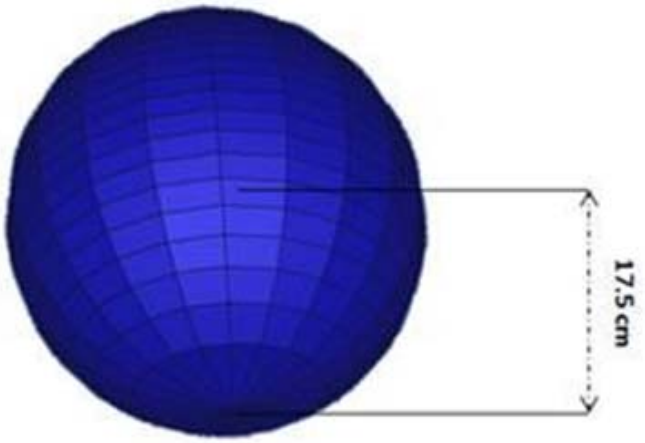

Fig 3.3 The MCNPX Phantom Model

The phantom slices which represent different depths of the tissue equivalent are referred to as phantom cells. Cell 1 with the radius of 2.5 cm represents the inner cell, while cell 7 with the radius of 17.5 cm represents the surface of the phantom. Fig.3.4, schematically, illustrates the position of different cells.

Cell Num	Radius of Cell (cm)
1	2.5
2	5
3	7.5
4	10
5	12.5
6	15
7	17.5
8	18

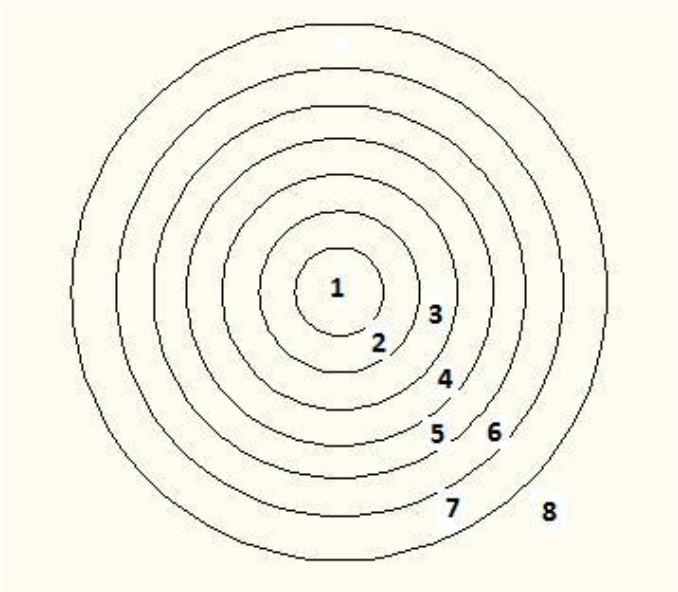

Fig 3.4 Phantom Cells

3.3.3 Neutron Production behind different Shielding

Since the astronaut spends most of his/her time in the service module (Fig.3.5) and, since the neutron production depends on the amount of shielding, a part of this work has been dedicated to the influence of the shielding thickness on the neutron production in the service module. Thus, the neutron spectra inside the service module have been simulated for different thicknesses of 7.5, 15 and 30 g/cm^2. An isotropic model has been built, where the protons with energy of 10-800 MeV were transmitted through Al shielding and the number of neutrons was calculated. Fig.3.6 illustrates such model.

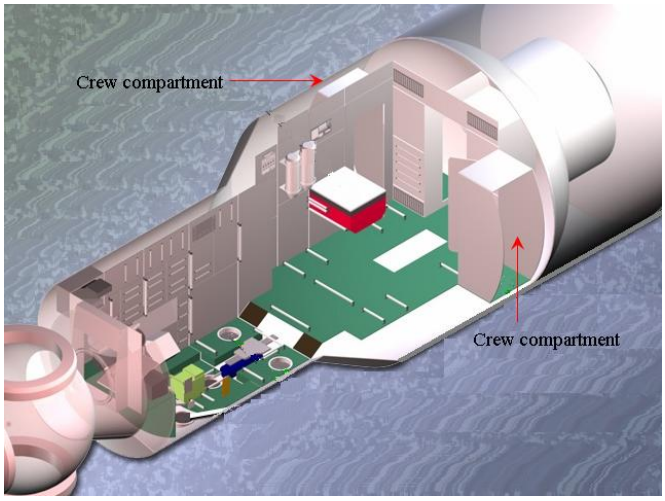

Fig 3.5 ISS Service Module

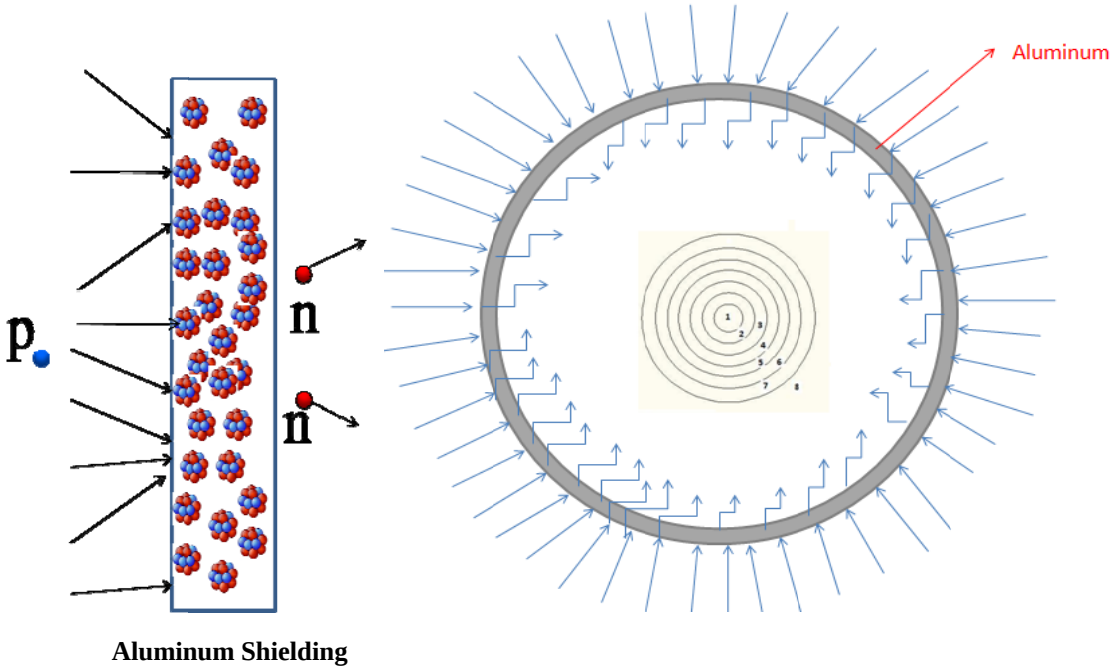

Fig 3.6 MCNPX Model with Aluminum Shielding

The result of the proton interaction of 10-800 MeV with three Al thicknesses of 7.5, 15, 30 g/ cm^2 are shown in Fig. 3.7.

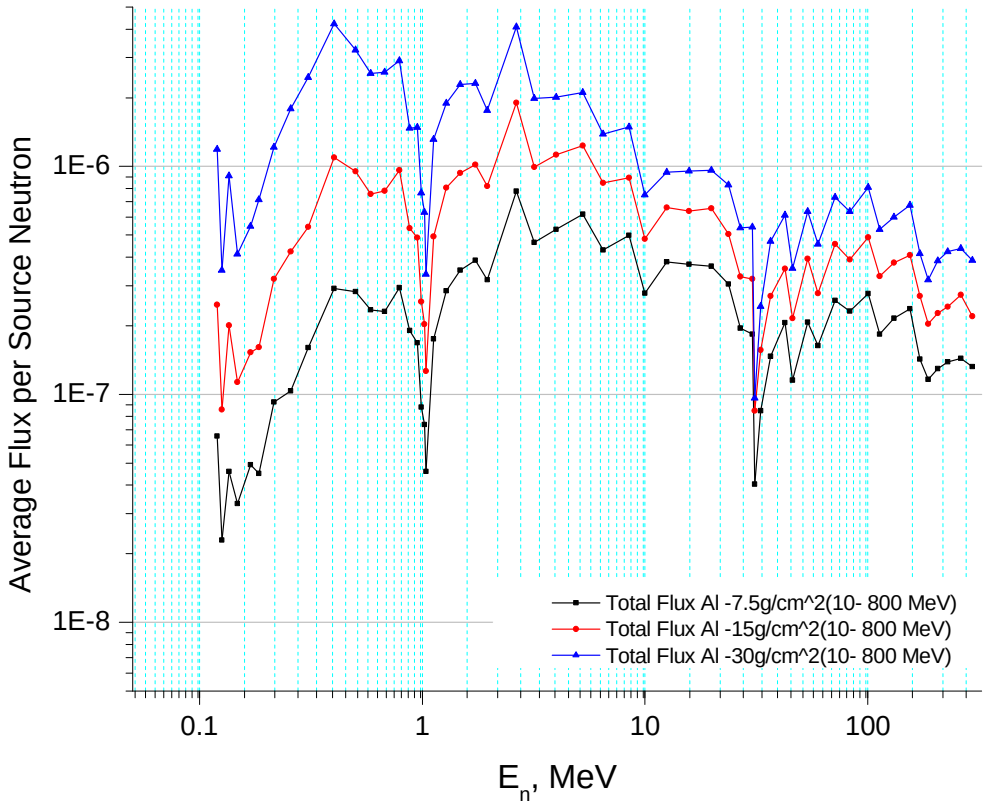

Fig 3.7 Neutron Spectra from Interaction of Protons of 10-800 MeV with three Al Thicknesses of 7.5, 15, 30 g/ cm^2

3.3.4 Neutron Production by Fast Secondary Neutrons

The space neutron spectrum is shown in Fig.3.8, was transmitted through the phantom model.

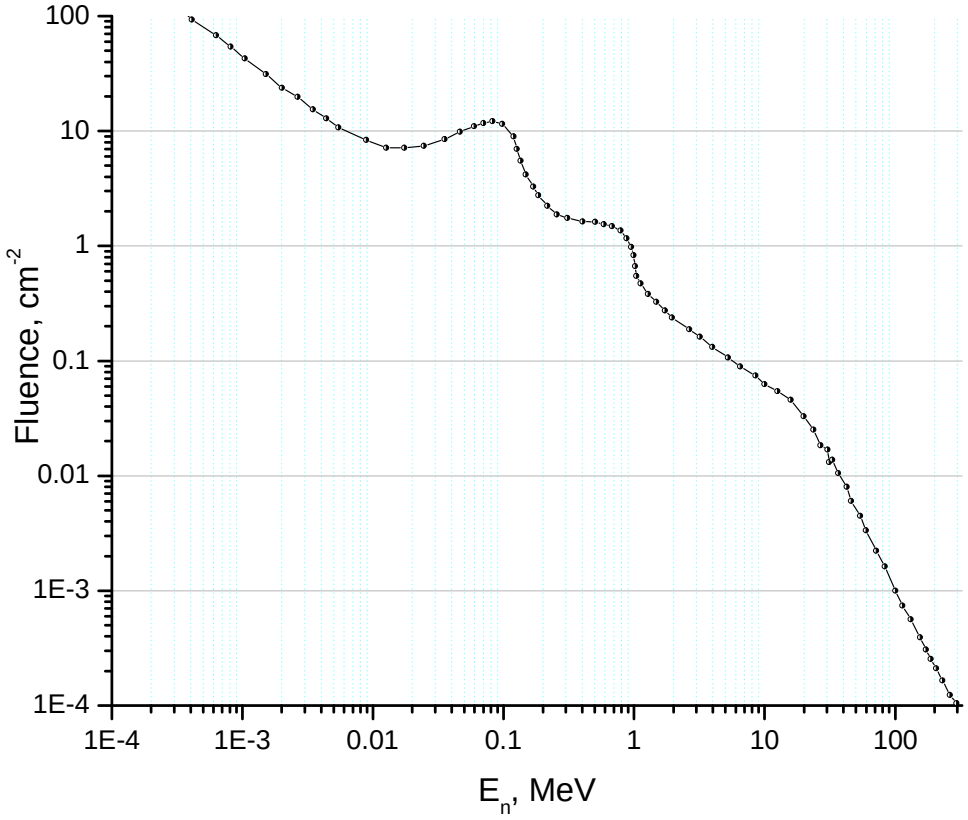

Fig.3.8 Neutron Spectra used in the Simulation

The average total flux has been calculated in different cells. Fig.3.9 shows the distribution of neutron in the phantom, and the obtained results of the average flux in different cell are shown in Fig.3.10.

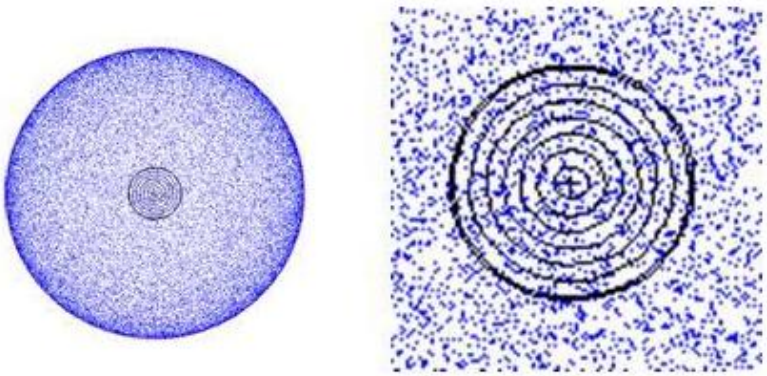

Fig.3.9 The Phantom Model Irradiated by the MIR-Station Neutron Spectra

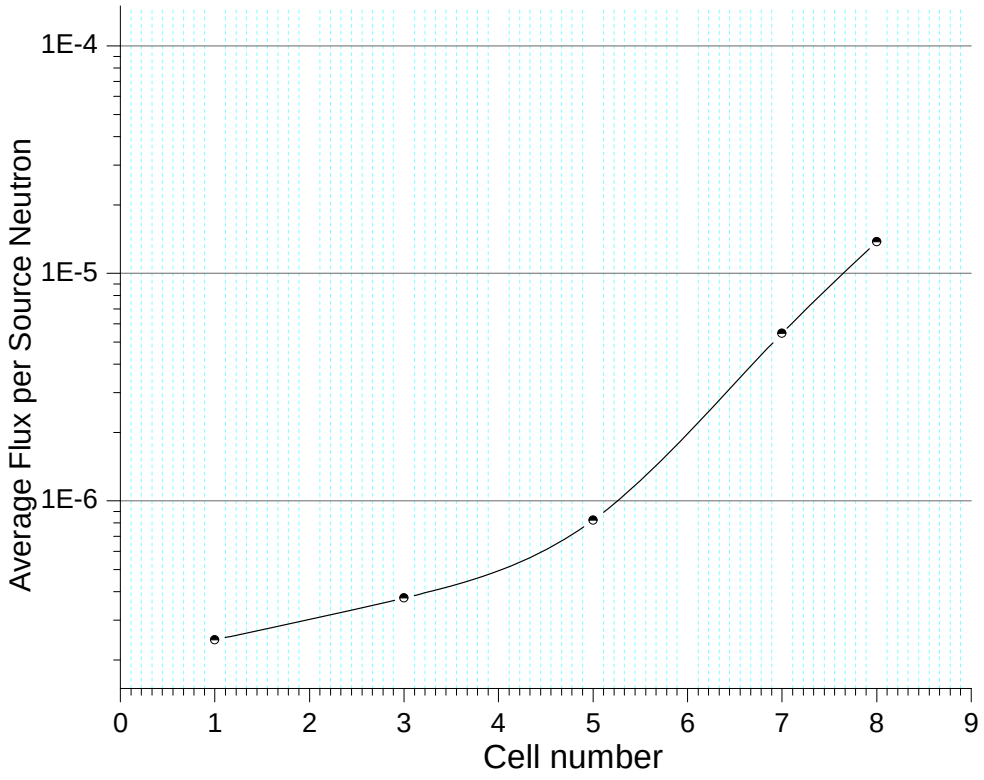

Fig.3.10 Total Neutron Flux in Each Cell of the Phantom

In addition to the total flux in individual cells, the neutron spectrum in different cells has been calculated. Since the major concern is to compare the neutron dose inside the phantom against the value outside the phantom, two spectra in internal and external cells are presented in Fig.3.11 and Fig.3.12, respectively.

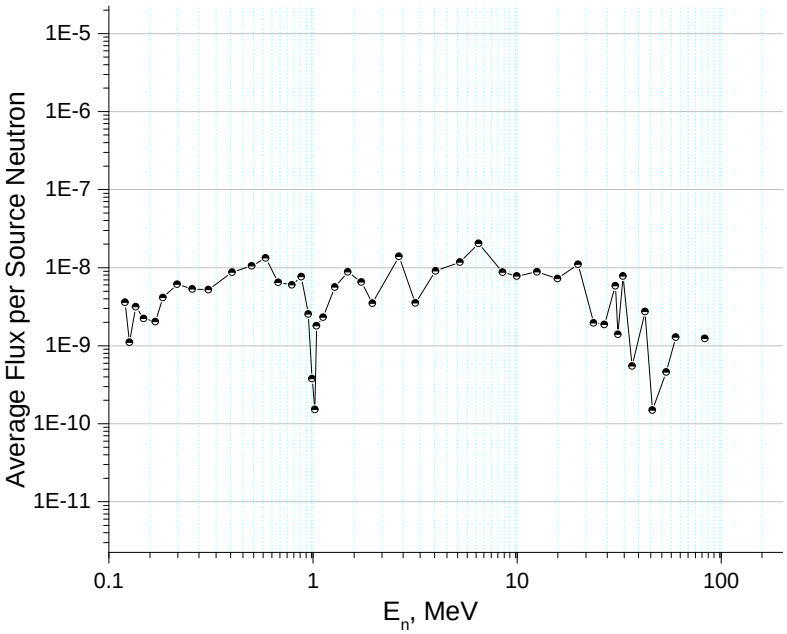

Fig.3.11 Neutron Flux in the Internal Phantom Cell

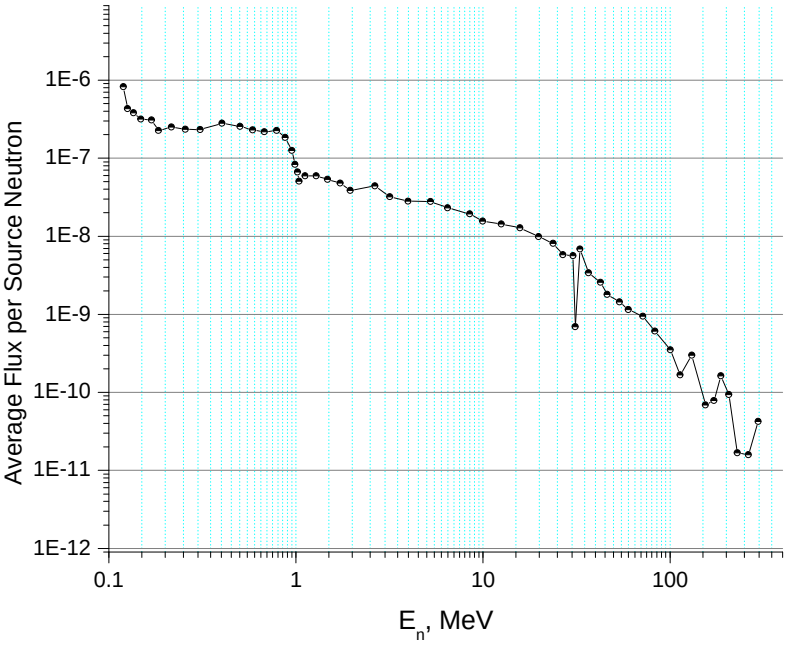

Fig.3.12 Neutron Flux in the External Phantom Cell

The neutron spectra in different cells are summarized in Fig.3.13.

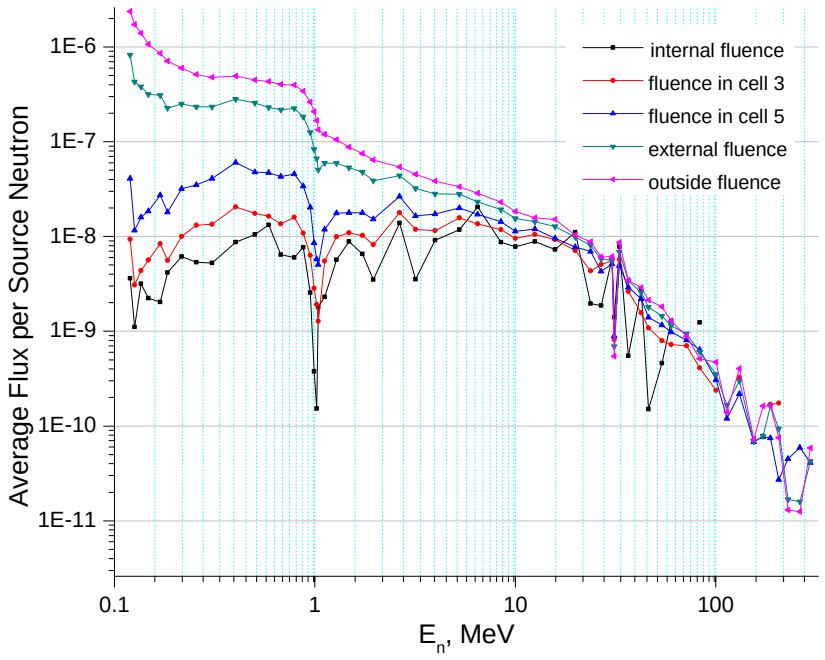

Fig.3.13. Neutron Spectra Calculate in Different Cells.

Fig.3.13 shows that the neutron spectra flux just outside of the outer cell is almost similar to the initial neutron energy spectra.

3.3.5 Neutron Production by Different Proton Energies

The internal mixed field of different particles inside the space station contains not only secondary neutron created as a result of charged particle interaction with the shielding material of the station, but also high energy protons and other particles that escape the interaction and get through the shielding material. Theses protons interact with the phantom and generate additional

secondary neutrons inside. To estimate their contribution, protons of different energies were transmitted through the phantom and the neutron flux have been calculated in different cells.

Before doing any MCNP calculation, the SRIM (The Stopping and Range of Ions in Matter) code was used to calculate the range of proton penetration inside the phantom, and the results are listed in Table.3.1. The proton of 10 MeV has a very short range of penetration, therefore, it will not reach the inner cell of the phantom and it cannot contribute that much to secondary neutron production inside the phantom. On the other hand, the protons of other energies have a larger range and their contribution can be significant to secondary neutron production.

Table.3.1. Proton Range in the Phantom Material

Proton Energy (MeV)	**Range, mm**
10	$779.31.10^3$
20	2.69
50	14.06
70	25.75
100	48.69
200	163.79
300	324.73
400	519.45
500	739.57
800	1500

To estimate the contribution of secondary neutrons as a result of the proton interactions, the phantom was bombarded by protons with different energies. The results from the simulation of 20, 100 MeV are shown in Fig. 3.14 and Fig.3.15, respectively. While Fig.3.16 presents the total average flux in different cells for energies from 50 to 800 MeV.

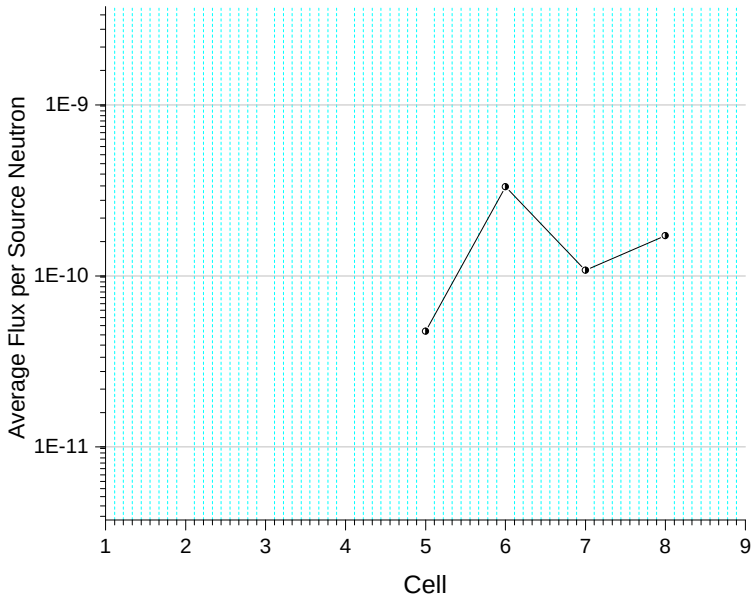

Fig.3.14 Neutron Production in all Cells of the Phantom from Interaction of 20 MeV Protons

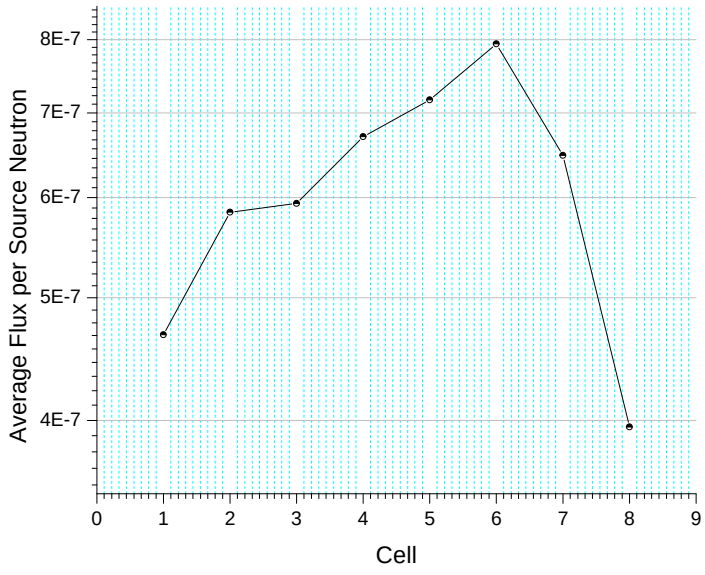

Fig.3.15 Neutron Production in all Cells of the Phantom from Interaction of 100 MeV Protons

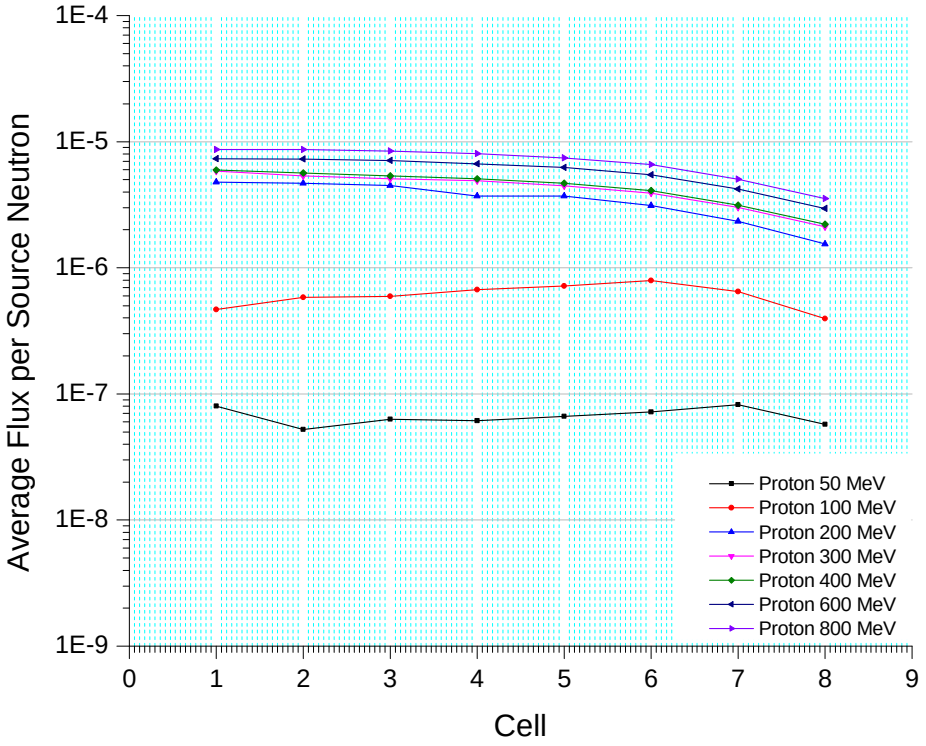

Fig.3.16 Neutron Production inside the Spherical Phantom as a Function of Proton Energies

Chapter 4:
Discussion and Analysis

Before analysing the obtained data, the built model of the phantom was compared to the cylindrical phantom model reported in NCRP-38 [23], and it was found that the ratio of the internal to external flux in both models is close to 4. The phantom was exposed to thermal neutrons and the results from the simulation are listed in Table.4.1.

Table.4.1 Comparison between MCNPX and NCRP-38 Phantom Model

	Spherical Phantom Model	**NCRP-38 Phantom Model**
External Flux (cm^{-2})	$1.43x10^{-5}$	$2x10^{-7}$
Internal Flux (cm^{-2})	$5.60x10^{-6}$	$8x10^{-8}$
Ratio of Int. to Ext. Flux	**3.87**	**4**

In this chapter, the obtained results will be discussed and compared with some experimental data that have been measured recently.

4.1 Neutron Production behind Different Shielding

Depending on their energy, when protons interact with the Al shielding, several neutron reactions take place. In the simulation, three thicknesses have been used, i.e. 2.78 cm (7.5 g/cm^2), 5.56 cm (15 g/cm^2) and 11.11 cm (30 g/cm^2) based on the estimation reported in ref [24]. The proton range for such thicknesses is presented in Table. 4.2. The results shown in Fig.3.7 present the neutron production behind the above listed thicknesses. It is clear that the neutron production is proportional to the thickness of the shielding material, because the rate of neutron reactions is proportional to the number of atoms that protons have chance to interact with. This

can be seen from the cross section of proton interaction with Al, presented in Fig.4.1. For the largest thickness of 11.11 cm, all proton energies less than about 180 MeV fully deposit their energy in the Aluminum shielding and create secondary neutrons. For other energies higher than 180 MeV, protons pass through the shielding and their contribution is not significant. From the same, Fig3.7, there are two valleys around 1 MeV and 30 MeV neutron energies corresponding to the resonance region, Fig. 4.2, where the probability of neutron absorption is significant.

Table 4.2 Proton Range in Al

Proton Energy, MeV	10	20	30	40	60	100	150	200	250
Range, cm	0.06	0.2	0.43	0.73	1.8	3.7	7.5	12.2	17.9

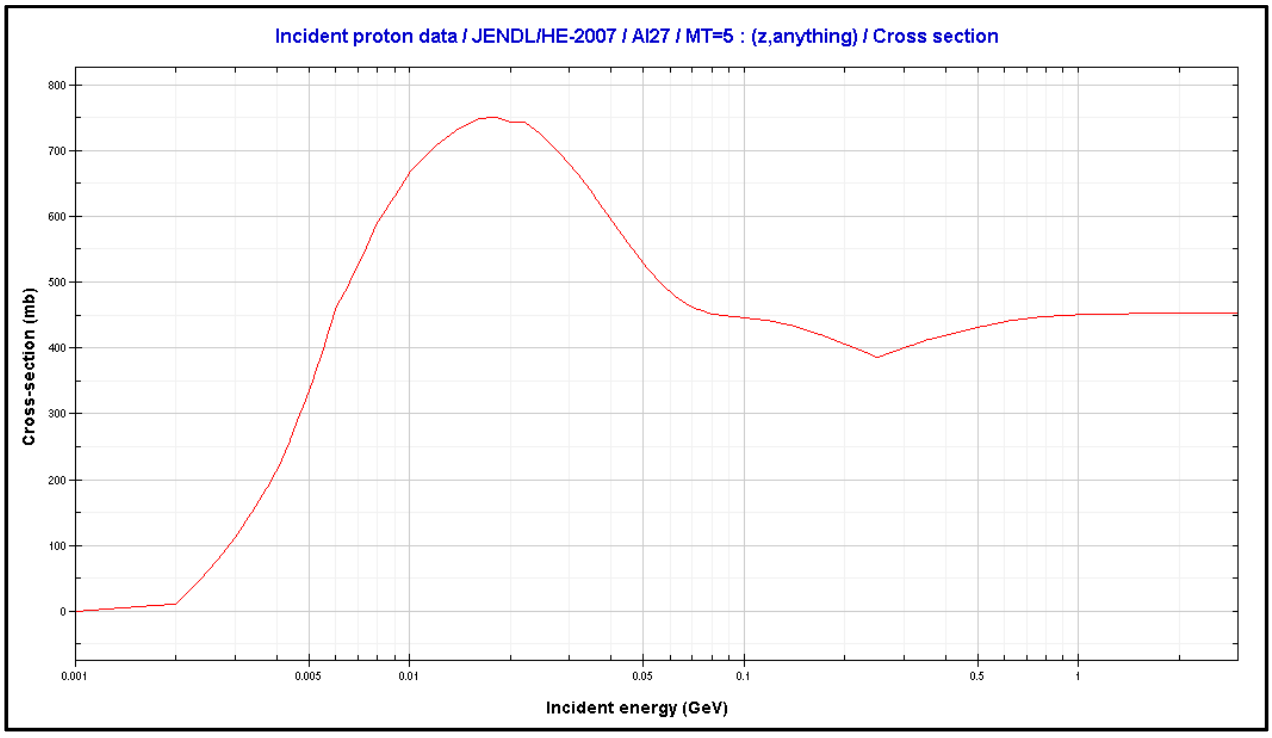

Fig.4.1 Total Cross Section of Proton Interaction with Aluminum

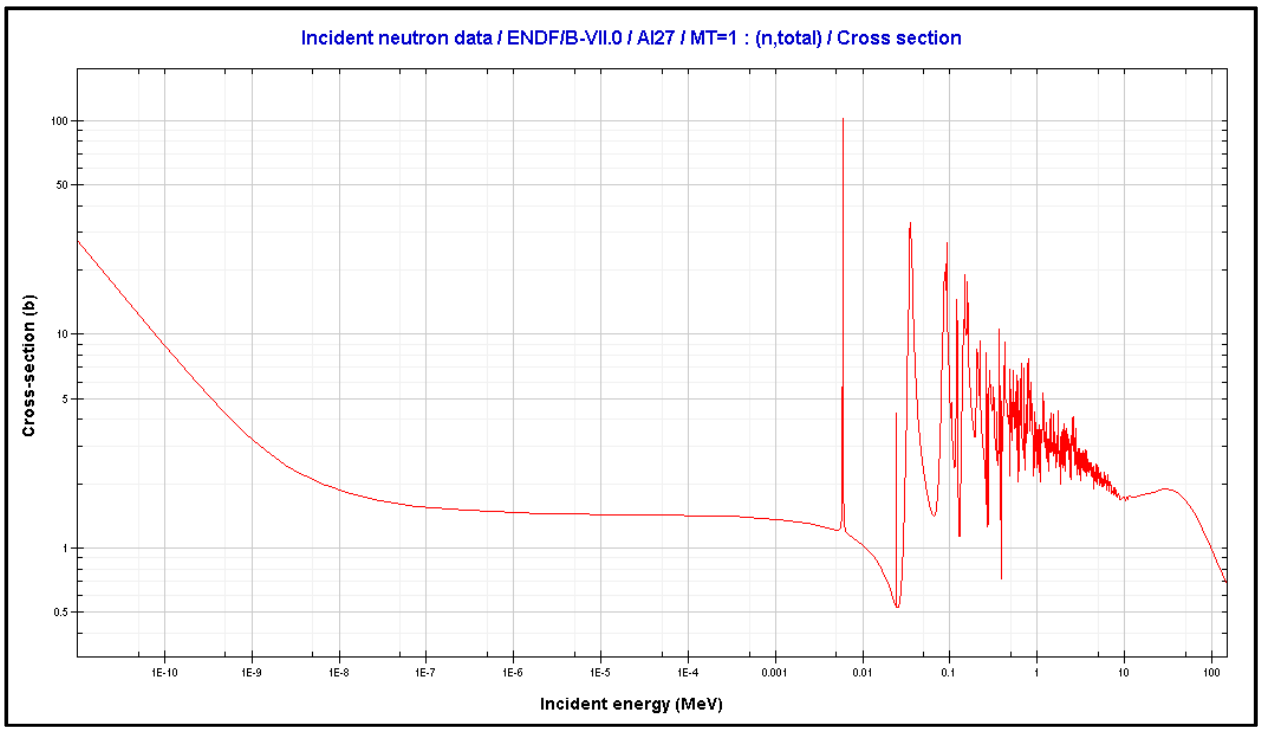

Fig.4.2 Total Neutron Absorption Cross Section in Aluminum

It should be mentioned that the obtained neutron spectra, using MCNPX, doesn't have the same shape as the measured spectra by Lygoshin [5]. This is due to the complexity of the space station shielding design where the shielding distribution is not well known and it differs from one location to another. The model used in this work has been simplified to a uniform shielding, Fig.3.6, where particles are coming uniformly from different angles. To be able to simulate the neutron spectra inside the space station, one should know the shielding distribution of the space station.

Later in this work the measured neutron spectra [5] was used for further calculation of neutron production inside the phantom from interaction of secondary neutrons.

4.2. Neutrons Production inside the Phantom by External Neutron Spectra

When high energy charged particles interact with the material shielding of the International Space Station, many neutrons are created as a result of such interactions. The neutron spectrum is very wide and it covers neutrons from thermal to very fast neutrons as shown in Fig 3.8. When these neutrons are transmitted through the phantom, there are two processes that compete, with each other, when the interaction with the phantom occurs. The first one is the absorption process due to the attenuation of neutrons in the phantom media, where low energy neutrons are more concerned because of the high absorption cross sections. Fig 4.3-Fig 4.6 show the absorption cross sections of O, N, C, and H, respectively. This process is an additive process and the total absorption cross section at one energy, such as thermal, is around few barns, but in the resonance region, especially, for the Oxygen, Nitrogen and Carbon its value is more than tens of barns. Therefore the rate of absorption of neutrons in the phantom may change the neutron spectrum shape from one cell to another.

The second process that competes with the absorption in the phantom is the production of neutrons as a result of interactions of the fast part of the energy spectra with the phantom media. Theses neutrons have enough energy to create secondary neutrons through different threshold reactions. Even their cross sections are not high enough, but in additive manner they can create enough secondary neutrons. The cross sections for (n,2n), (n,3n) and (n,4n) reactions for C are presented in Fig.4.7. In this regards, the comparison between the absorption and the production cross section are clearly different in the favour of absorption which is mostly dominating.

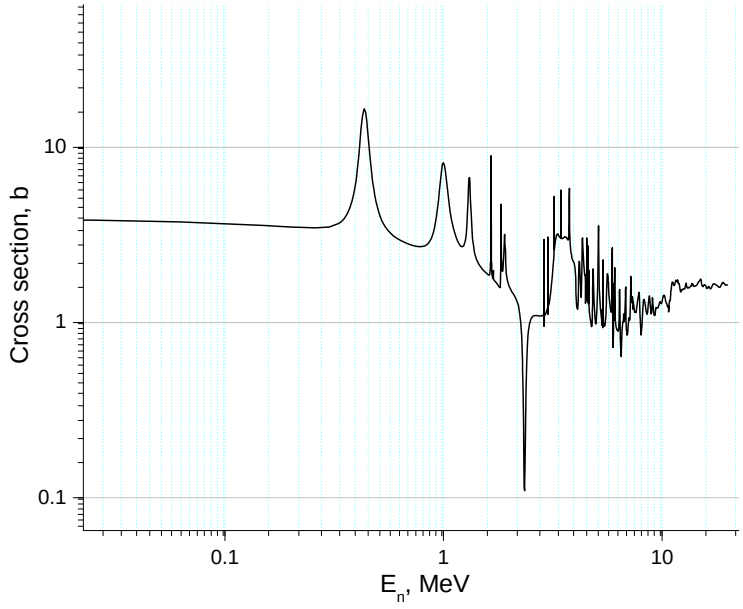

Fig.4.3 Total Neutron Cross Section of Oxygen

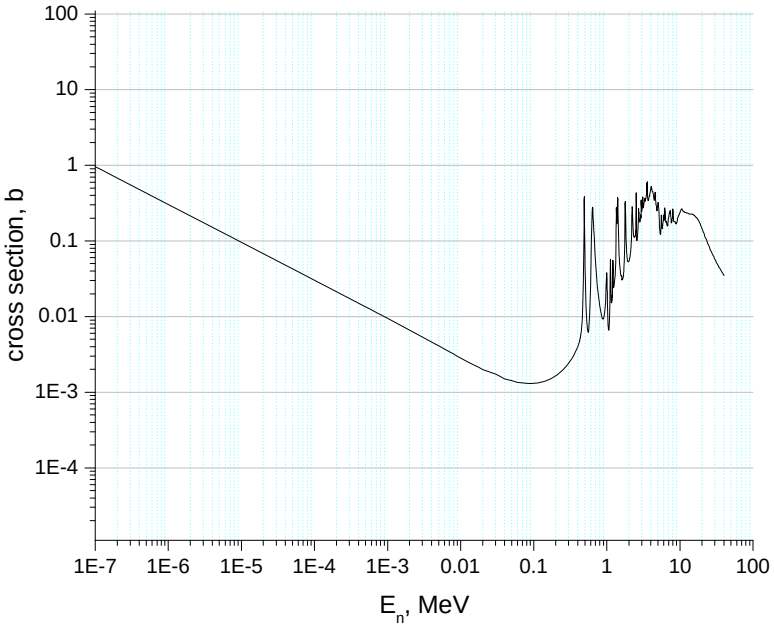

Fig.4.4 Absorption Neutron Cross Section of Nitrogen

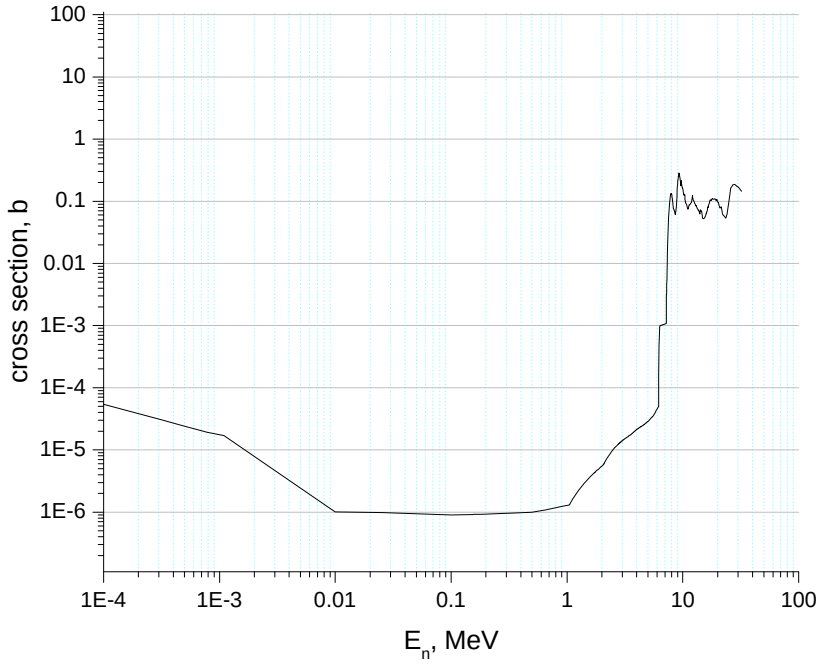

Fig.4.5 Absorption Neutron Cross Section of Carbon

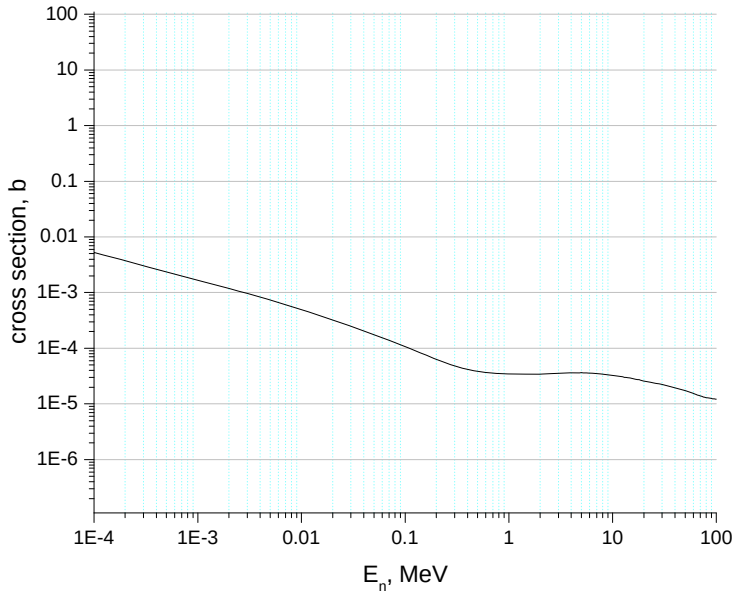

Fig.4.6 Absorption Neutron Cross Section of Hydrogen

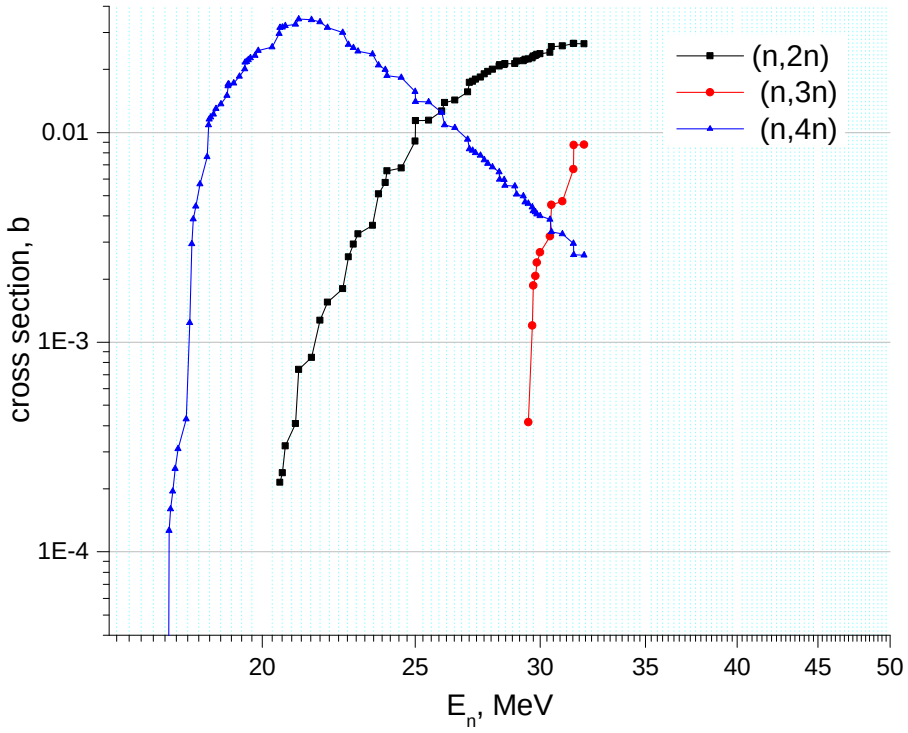

Fig.4.7 Reaction Cross Section of (n,2n), (n,3n), and (n,4n)

When analysing the data obtained from MCNPX in different cells, Fig.3.10, when the phantom has exposed to the space spectra, one can see that neutrons have been attenuated and their number decreases when going from the external cell to the internal one. This is explicitly clear when comparing the flux of neutrons in cell 1 against the flux calculated in cell 7. In Table.4.3 are given the fluxes calculated in different cells. Also Fig.4.8 and Fig.4.9 are illustrating such difference.

Table.4.3. Neutron Flux in Different Cells when exposing the Phantom to Space Spectra

Cell Num	Cell Radius, cm	Flux, cm^{-2}
1	2.5	2.45E-07
3	7.5	3.74E-07
5	12.5	8.24E-07
7	17.5	5.45E-06
8	18	1.38E-05

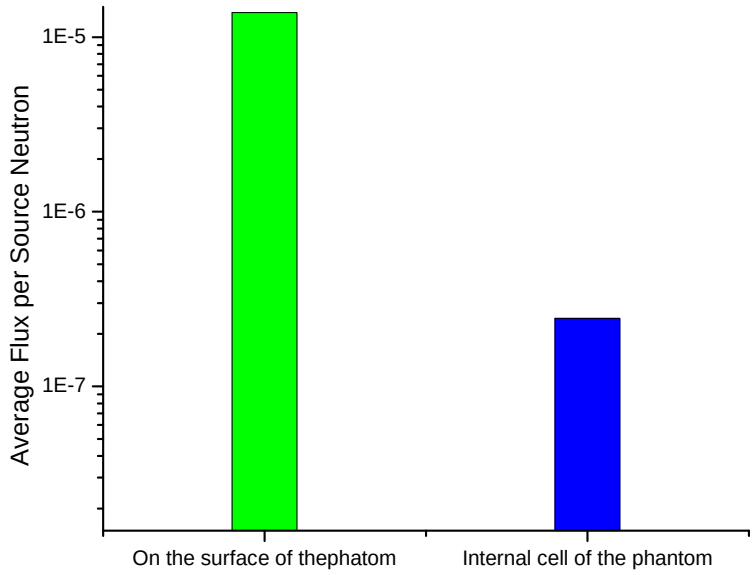

Fig 4.8 Difference of Neutron Flux between External and internal Cell of the Phantom

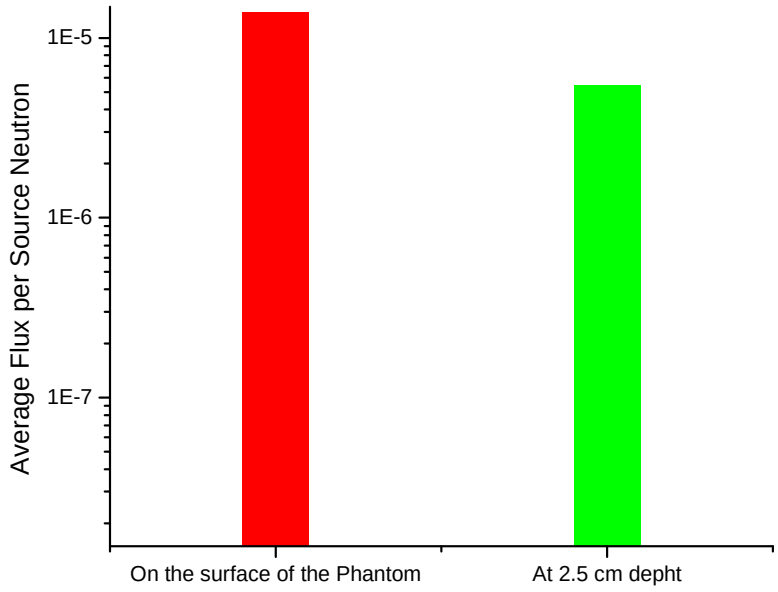

Fig.4.9 Comparison of Neutron Fluxes between outside and in the outer cell (surface) of the Phantom

The same behaviour is occurring when comparing the result of the simulation that calculates the neutron spectra instead of the total average flux in the external cell (cell 7) and in the internal one. Fig.3.11 and Fig.3.12 shows clearly the difference between the 2 spectra. In addition, Fig.3.13, illustrates the neutron spectra in different cells of the phantom. Notice that, there is sharp peak shown a great deal of absorption around 1 MeV. This can be explained by the resonance character of the absorption cross section of Oxygen, Carbon and Nitrogen that are ones of elements making up the phantom.

4.3. Neutrons Production inside the Phantom by External Protons

Not all charged particles from cosmic radiation interact with the shielding material of the international space station. Since protons presents more than 86% of the charged particle flux hitting the space craft external material, some of them pass through without any interactions. In the literature, there is no precise data on the fluence of the charged particle field inside the space station; however some estimation has be done. These protons interact with the phantom media through different high energy reactions. Among them one can cite neutrons as secondary products. The rate of such production depends mainly on the cross section of the interaction with the constituents of the phantom such Oxygen, Carbon and Nitrogen.

Fig.4.10 shows the cross for different reactions that can produce neutrons when different high energy protons interact with the phantom media (Nitrogen). Also Fig.4.11 and Fig.4.12 show the cross section of neutron production through different reaction with the oxygen and carbon that make up the phantom.

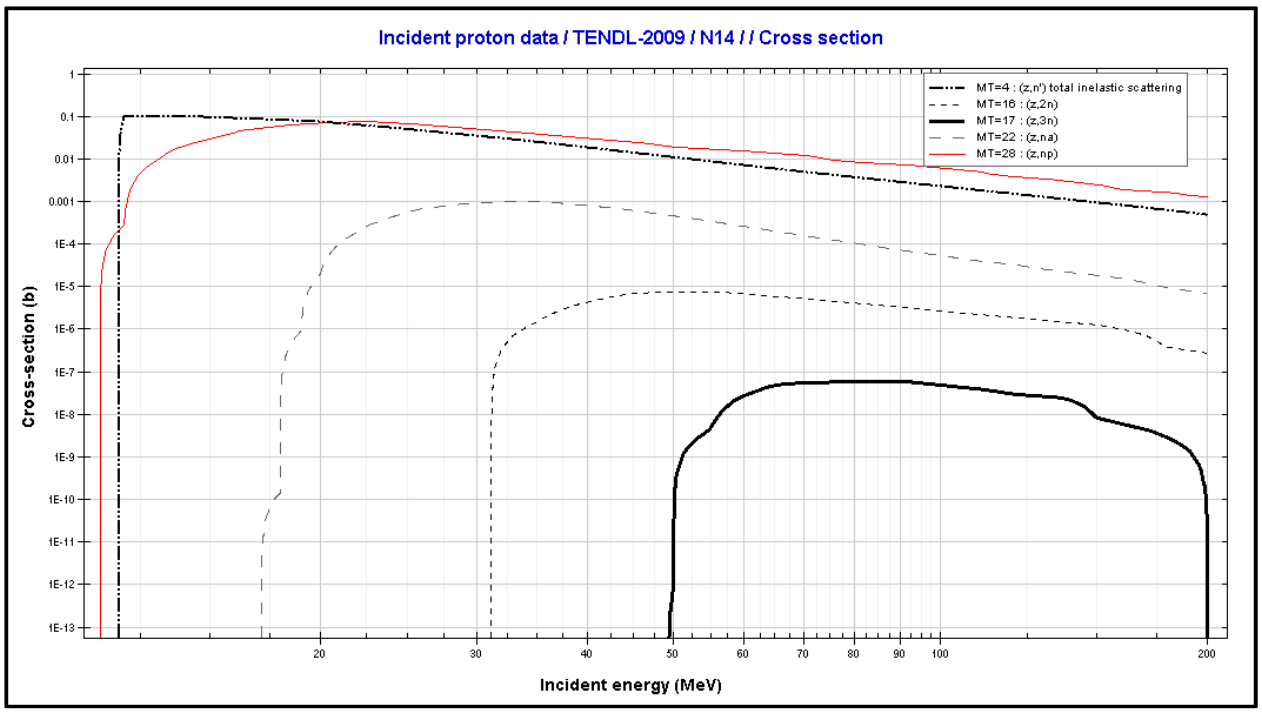

Fig.4.10 Cross Section of Neutron Production from Reactions on Nitrogen as a Function of Proton Energy

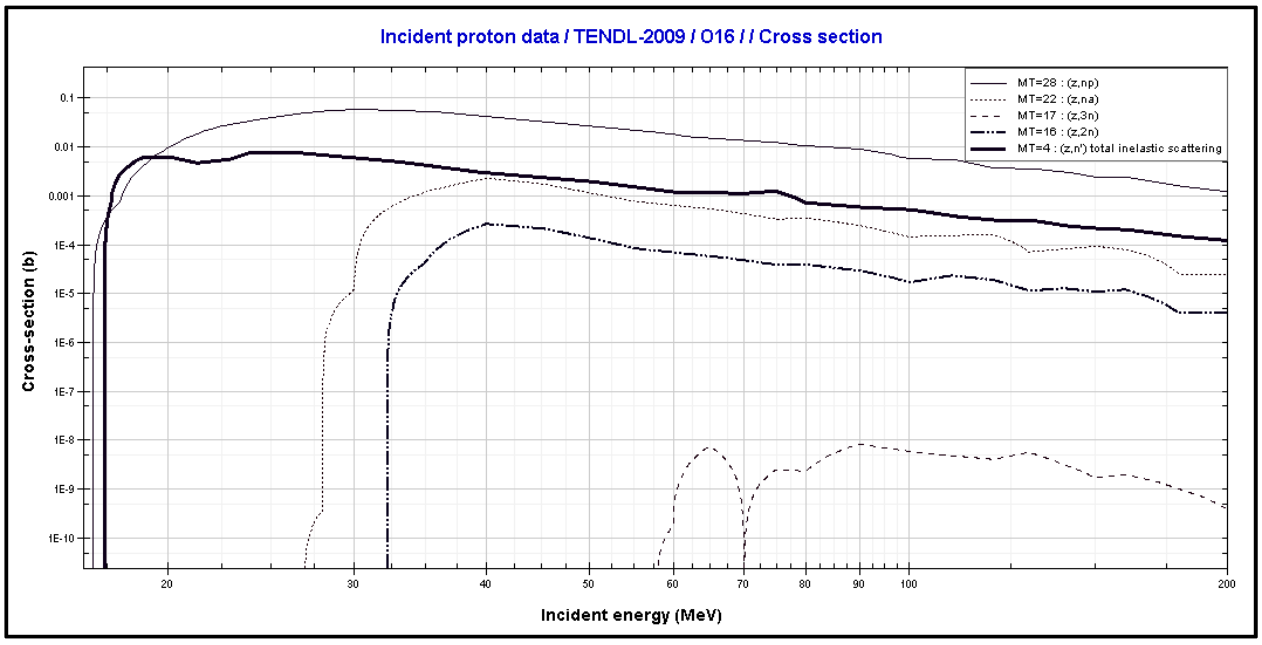

Fig.4.11 Cross Section of Neutron Production from Reactions on Oxygen as a Function of Proton Energy

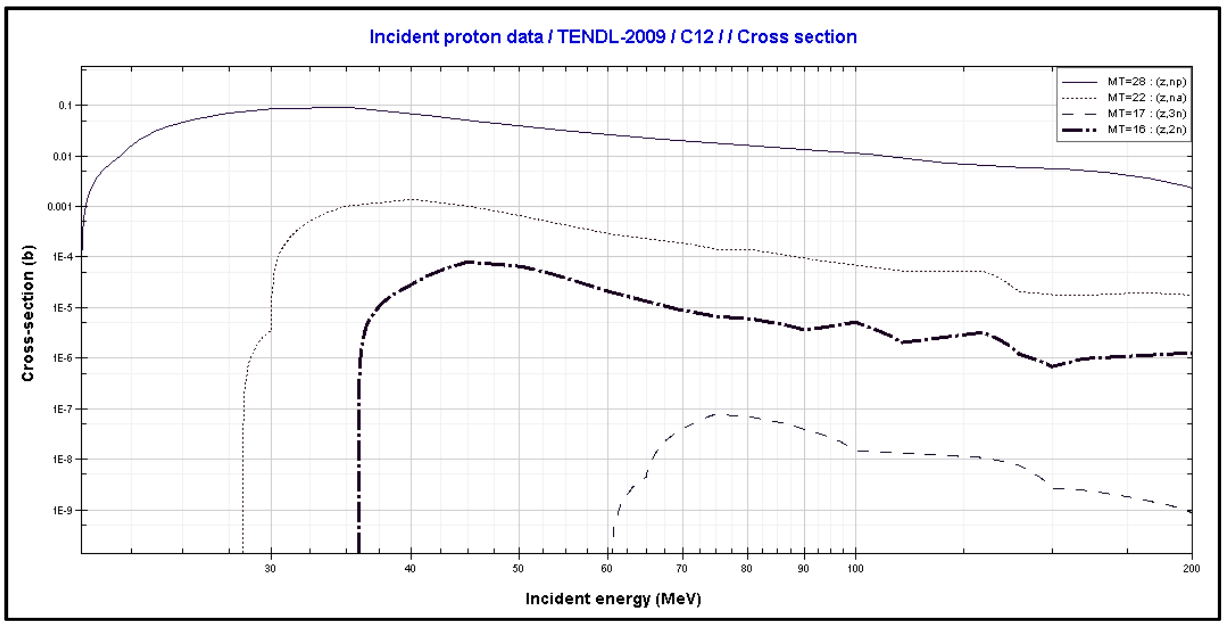

Fig.4.12 Cross Section of Neutron Production from Reactions on Carbon as a Function of Proton Energy

In the second part of the simulation, the phantom was exposed to different protons energy and the task was divided into two parts: the first part is the calculation of the total flux of neutrons in each cell of the phantom while in the second part, the neutron spectra has been calculated for each cell for every single proton energy.

The total neutron flux in different cell of the phantom for proton energies of 50-800 MeV is shown in Fig.3.16. Also, the summaries of results for secondary neutron production from the proton interaction with phantom protons in different cells are shown in Table.4.4. Also, Appendix C illustrates the results of neutron production in each cell for different proton energies.

Table.4.4. Neutron Flux in Different Cell of the Phantom when Bombarding the Phantom with Different Proton Energies

Cell Num	Radius (cm)	20 MeV	50 MeV	70 MeV	100 MeV
1	2.5	8.30E-08	8.33E-08	6.64E-08	5.54E-07
3	7.5	5.91E-08	5.93E-08	5.88E-08	5.78E-07
5	12.5	5.94E-08	5.97E-08	5.90E-08	7.19E-07
7	17.5	8.36E-08	8.36E-08	8.33E-08	6.51E-07
8	18	5.82E-08	5.83E-08	5.82E-08	3.94E-07

Table.4.4 Neutron Flux in Different Cell of the Phantom when Bombarding the Phantom with Different Proton Energies

Cell Num	Radius (cm)	200 MeV	300 MeV	400 MeV	500 MeV	800 MeV
1	2.5	5.02E-06	5.72E-06	5.99E-06	6.14E-06	8.49E-06
3	7.5	4.48E-06	5.04E-06	5.35E-06	5.97E-06	8.44E-06
5	12.5	3.72E-06	4.46E-06	4.71E-06	5.25E-06	7.44E-06
7	17.5	2.32E-06	2.99E-06	3.16E-06	3.56E-06	5.05E-06
8	18	1.54E-06	2.09E-06	2.23E-06	2.48E-06	3.54E-06

Protons inside the international space have an extended spectrum from few MeV to few hundred of MeV. The reactions that can take place with the phantom to produce neutrons have relatively small cross sections, but in additive manner, they can contribute to the population of secondary neutrons inside the phantom media. As an example, the cross section of the proton interaction with Nitrogen, Oxygen, and Carbon are presented in Fig.4.10, Fig.4.11 and Fig.4.12. The contribution for all these reactions can compensate for such process of attenuation for external neutron flux passing through the phantom. Individually, a comparison has been done for the contribution of different energy protons in the neutron production in two specific cells of concern, mainly, the internal cell and the external one. The result of the comparison is shown in Fig.4.13 and Fig.4.14, respectively.

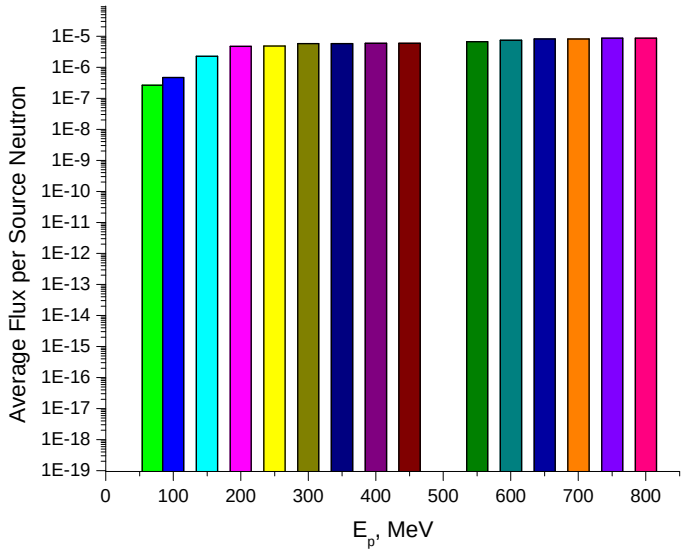

Fig.4.13. Neutron Production as Function of Different Proton Energies in the Internal Cell

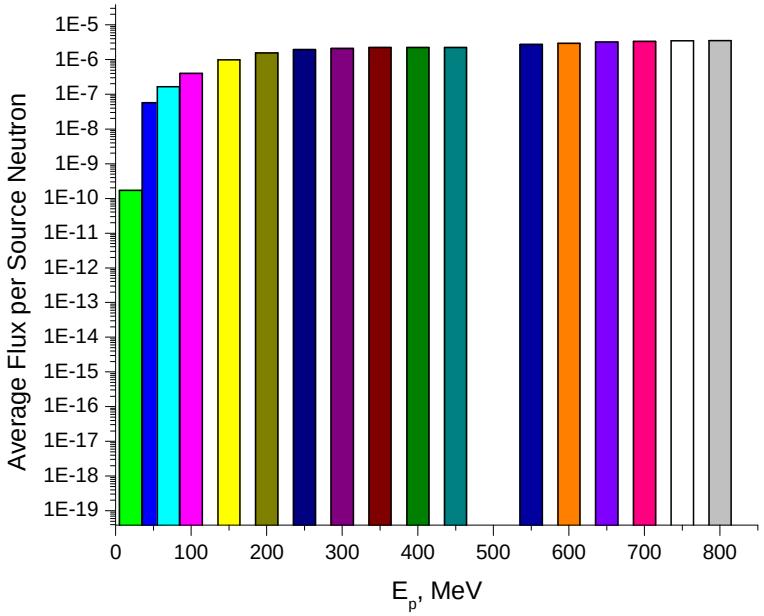

Fig.4.14 Neutron Production as Function of Different Proton Energies in the External Cell

The low energy protons do not contribute to the neutron production in the inner cell because of their short range. For instance protons of 20 MeV are stopped after penetrating only a few millimetres inside the phantom, therefore they cannot reach the inner cell. This can be seen in Fig.3.14 where the average neutron flux in different cells is presented. However, for high energy, protons can penetrate deeper in the phantom and consequently can produce more neutrons in different cells. An example is illustrated clearly in Fig3.15, where 100 MeV protons have been transmitted through the phantom. From this figure, one can see that at around 13.5 cm depth, the neutron production reaches its maximum value (Bragg peak where the proton deposits its maximum energy at the end of its range). After the maximum value, the number of neutrons decreases towards the center of the phantom because of the neutron absorption process (neutron attenuation).

As the proton energy increases, the number of created neutrons increases accordantly in both cell external as well as the internal one. Notice that reactions with protons are threshold reactions i.e. (p, n) and (p, xn) and require different proton energies thresholds to occur. From Fig.4.13 and Fig.4.14, it is clear that the neutron flux increase due to the number of reaction that are taking place when the threshold energy is reached. In other words for high energy protons other neutron reaction channels open up.

It should be motioned, from the comparison of the above figures, that the overall number of neutrons in the internal cell is higher than in the external one. This is expected due to the long range that high energy protons have when going through from the surface of the phantom toward the center. This gives more chance to those protons to interact along their track and create more neutrons.

4.4. Overall Neutrons Production inside the Phantom

As a result of interaction with the fast part of the neutron spectra and high energy protons with the constituents of the phantom, a large number of neutrons are created at different depths. The overall contribution from different components is a sum from the fast neutron side as well as from the proton side. As mentioned above, there are 2 processes competing inside the phantom: the process of absorption against the process of production. To get the overall neutron flux in each cell the neutron flux produced using neutron spectra and protons from 20-800 MeV were added together and the result are presented in Table.4.5.

Table 4.5 Overall Neutron Flux inside the Phantom

Cell Num	Radius , cm	20 MeV	50 MeV	70 MeV	100 MeV
1	2.5	$3.28.10^{7}$	$3.29.10^{7}$	$3.12.10^{7}$	$7.99.10^{7}$
3	7.5	$4.33.10^{7}$	$4.33.10^{7}$	$4.33.10^{7}$	$9.52.10^{7}$
5	12.5	$8.84.10^{7}$	$8.84.10^{7}$	$8.83.10^{7}$	$1.54.10^{6}$
7	17.5	$5.54.10^{6}$	$5.54.10^{6}$	$5.53.10^{6}$	$6.10.10^{6}$
8	18	$1.38.10^{5}$	$1.38.10^{5}$	$1.38.10^{5}$	$1.42.10^{5}$

200 MeV	300 MeV	400 MeV	500 MeV	800 MeV
5.26E-06	$5.97.10^{6}$	$6.23.10^{6}$	$6.39.10^{6}$	$8.74.10^{6}$
4.85E-06	$5.42.10^{6}$	$5.73.10^{6}$	$6.35.10^{6}$	$8.81.10^{6}$
4.54E-06	$5.28.10^{6}$	$5.53.10^{6}$	$6.07.10^{6}$	$8.26.10^{6}$
7.77E-06	$8.44.10^{6}$	$8.61.10^{6}$	$9.01.10^{6}$	$1.05.10^{5}$
1.53E-05	$1.59.10^{5}$	$1.60.10^{5}$	$1.63.10^{5}$	$1.73.10^{5}$

Finally the ratio of external to internal neutron flux due to the absorption and production processes was calculated and the results are shown in Table.4.6. This ratio shows that there is

almost no difference between the internal to external value of the overall flux which means there is a major contribution in producing neutron inside the phantom from other processes.

Table.4.6 Ratio of External Neutron Flux to Internal Neutron Flux

	Flux when the phantom was exposed to neutron space spectra	**Flux when the phantom was exposed to protons**	**Overall Neutron Flux**
In internal cell	2.45E-07	3.21E-05	$8.43.10^{-05}$
In external cell	5.45E-06	1.80E-05	$5.29.10^{-05}$
Ratio	**22.23**	**0.56**	**0.63**

From the table above, without proton contribution the ratio of the external flux to internal one is about 22 times. This attests that the process of neutron attenuation, dramatically, reduces the neutron population when going though the phantom. This confirms the study conducted with cylindrical phantom in NCRP-38 [23].

4.5. Comparison between Experimental Data and Simulation

The Matroshka-R experiments with space bubble detector have used the same spherical phantom used in this simulation. The experimental data has shown that the dose received internally and externally is almost the same even in different modules of the international space station that has different shielding thicknesses (Docking and service modules) [9]. The result of one of such experiment is shown in Table 4.7. This attests that the dose read by a dosimeter worn on the human body in space is not an overestimate of the real dose received by critical organs as it is on Earth. However, in this experiment the estimation of the charged particle contributions was difficult due to the lack of experimental data on charged particles inside the station.

The simulation conducted in this work shows that the overall neutron flux calculated almost close to the surface of the phantom and the flux at the center has a difference of only 28% (Table4.6). It is hard to say that this calculation confirm the experimental data since the dose measured is a contribution of all neutron energies and it is very well known that the dose curve (fluence to dose conversion factor) depends on the neutron energy. However what this calculation can confirm is the fact that, in space there are some other processes that contribute to neutron production inside the phantom and compensate for the decrease of the dose due to the attenuation of the neutron spectra observed on the surface. Unfortunately, the lack of data on the cosmic-ray spectra within the ISS makes an estimation of the contribution of charged particles to neutron production in the phantom very difficult.

Table 4.7 Ratio of External to Internal Dose Measurement Obtained in Three Different Experiments [7]

Dose rate	Measurement #1	Measurement # 2	Measurement # 3
Internal Dose rate, (μSv/d)	94±14	83±17	97±16
External Dose rate (μSv/d)	114±16	119±23	120±18
Ratio	1.21±0.35	1.43±0.56	1.24±0.38

Conclusion

In the frame of an ongoing large international collaboration on space radiation monitoring, this work has been conducted to investigate the relationship of the internal to external flux of neutrons of the Russian spherical phantom currently aboard the international space station and to clarify the large difference between the behaviour of the neutron dose internally and externally.

Due to the lack of the data on the cosmic ray spectra Monte Carlo simulation code MCNPX has been used to estimate secondary neutron production on the surface and inside the phantom. For such goal, the Russian spherical phantom has been used. The phantom was first bombarded with a measured neutron spectra and the neutron flux resulted from the neutron produced by fast neutrons when interaction with the constituents of the phantom such as Oxygen, Hydrogen and carbon has been calculated.

In the second part of the simulation, the calculation has covered a large interval of protons energies from 20 to 800 MeV that interact with the phantom and produce secondary neutrons in different layers of the phantom.

Finally, the neutrons produced from proton interaction was added to the number of neutrons produced using the neutron spectrum and the external to internal neutron flux ratio was calculated for different proton energies. Also, the ratio of external to internal neutron flux was calculated to be 0.63 assuming that the proton spectra cover from 20 to 800 MeV.

The calculation has shown that the ratio is of 0.63, which is two times less than the experimental ratio of the measured dose rate 1.3.

To clarify the difference between the phantom in space and the one on earth, experimental data on the cosmic ray spectra inside of the international space station are needed. There is a lack of data and information not only on the charged particle spectra but also on the neutron spectra inside the ISS. There should be more investigation on several parameters that affect the radiation environment inside the space station, mainly, structure and mass distribution of the station, the altitude of the spacecraft and space weather conditions. Also, the detectors which are been used in the experiment have been calibrated using terrestrial sources, which are different from the source of space radiation.

Future Work

From previous calculations and experiments, the major issue that have to be investigated is an accurate measurement of the neutron spectra to clarify the large difference between the internal and external doses. To do so, it is very important to:

- Measure the neutron spectra on the surface of the phantom
- Simulate these spectra with MCNP through the phantom
- Measure the spectra inside the phantom and compare it with the simulated one.

If the measured spectra inside is the same as the simulated one there is a need to find an alternative explanation for the low attenuation of neutrons incident on the phantom. But if the spectrum is different, that means there is a contribution from other process (es) that contribute to neutron production inside the phantom and compensate for the decrease of the dose due to the attenuation of the neutron spectra observed on the surface.

References

1. Proceeding of workshop, Predictions and Measurements of Secondary Neutron in Space, Houston Texas, September 20-30, 1998.
2. Gautam D. Badhwar, *Deep Space Radiation Sources, Models, and Environmental Uncertainty,* Shielding Strategies for Human Space Exploration, NASA Conference Publication 3360*,* December 1997, pp 17-28.
3. L. Heilbronn, L. W. Townsend, *Overview of Ground Based Neutron Measurements Applicable to GCR and SPE Transport Through Shielding Material In Space*, Proceeding of workshop, September 20-30, 1998, Houston Texas, Predictions and Measurements of Secondary Neutron in Space.
4. H. Matsumoto and T. Goka, K. Koga, T. Omoto and T. Watari, *Real-Time Neutron Measurement in Shuttle Flight, STS-89,* Proceeding of workshop, September 20-30, 1998, Houston Texas, Predictions and Measurements of Secondary Neutron in Space.
5. V. I. Lyagushin, V.E. Dudkin, Yu. V. Potapov and V.D. Sevastainov, *Russian Measurments of Neutron Energy Spectra on the Mir Orbital Station,* Radiat, Meas. 33, 313–319, 2000.
6. L. A. Braby, G.D. Badhwar. *Proportional Counters as Neutron Detector*, Proceeding of workshop, September 20-30, 1998, Houston Texas, Predictions and Measurements of Secondary Neutron in Space.
7. H. Ing. *Neutron Measurements Using Bubble Detectors- Terrestrial and Space,* Proceeding of workshop, September 20-30, 1998, Houston Texas, Predictions and Measurements of Secondary Neutron in Space.
8. D. Badhwar, J.E. Keith and T. Cleghorn. *Neutron Dosimertic Measurements Onboard the Space Shuttle,* Proceeding of workshop, September 20-30, 1998, Houston Texas, Predictions and Measurements of Secondary Neutron in Space.
9. R. Machrafi, K. Garrow, H. Ing. M. B. Smith, H. R. Andrewa, *Neutron Dose Study With Bubble Detectors Aboard The International Space Station As Part of The Matroshka-R Experiment,* Radiation Protection Dosimetry, (2009), pp 1-8.
10. MCNPX™ USER'S MANUAL, Denise B. Pelowitz, editor, Version 2.6.0, April, 2008
11. ICRP Publication 60, *Annals of the ICRP,* 21, (No. 1–3), Pergamon Press, Oxford, 1991.

12. NCRP116, Limitation of Exposure to Ionizing Radiation, NCRP Report No. 116, National Council on Radiation Protection and Measurements, Bethesda, MD, 1993.
13. Lisa C. Simonsen, *Analysis of Lunar and Mars Habitation Modules for the Space Exploration Initiative (SEI)*, Shielding Strategies for Human Space Exploration, NASA Conference Publication 3360, December 1997, pp 43-77. (1997)
14. National Council of Radiation Protection and Measurements: Guidance on Radiation Received in Space Activities. NCRP Report No. 98, July 31, 1989.
15. John W. Wilson, Francis A. Cucinotta, Sheila A. Thibeault, Myung-Hee Kim, Judy L. Shinn and Francis F. Badavi*: Radiation Shielding Design Issue*, Shielding Strategies for Human Space Exploration, NASA Conference Publication 3360, December 1997, pp 109-149.
16. Stsnley B. Curtis, *Human Risk Models and Risk Uncertainty*, Shielding Strategies for Human Space Exploration, NASA Conference Publication 3360, December 1997, pp 79-90.
17. National Aeronautics and Space Administration report "Strategic Program Plan for Space Radiation Health Research," Life Science Division, Office of Life and Microgravity Science and Applications, 1998.
18. http://spacemath.gsfc.nasa.gov
19. L. Heilbronn, *Production of Neutrons from Interactions of GCR- Like Particles,* Shielding Strategies for Human Space Exploration, NASA Conference Publication 3360, December 1997, pp 247-259.
20. A. Farrari, A. Mitaroff, M. Silari*, A Reference Radiation Facility for Dosimetry at Flight Altitude and Space*, Physica Medica - Vol. XVII, Supplement 1, 2001.
21. Lewis consultant, *Review of Radiation Detector Research and Technology Development* Canadian Space Agency Internal report, March 31,2001.
22. Bubble Technology, *Matroshka-R Experiment Phase 2 Final Report*, March 31st , 2009.
23. National Council of Radiation Protection and Measurements: Protection against Neutron Radiation. NCRP Report No. 38, January 4, 1971.
24. Mitrikas V.G. shielding model in manned section of service module of ISS for radiation safety estimation, Avia-kosmicheskaya I ecology medicine, 2004 T.38, N3, pp.41-47.

Appendices

Appendix A: Neutron Sources and Neutron Interactions

Atomic nuclei consist of protons and neutrons; neutron is a subatomic particle with no electric charge and is slightly larger than the proton with a mass of 1.67495×10^{-27}. The neutrons are not stable particles except when are bounded into an atomic nucleus. Atoms with excess number of neutron emit neutron through radiation decays. The neutrons produced through radiation decays are called free neutrons. Free neutrons can be classified into different energy levels, thermal and fast neutrons.

Neutrons can be classified according to their energies, thermal neutrons with the energy of 0.025 eV, slow or intermediate neutrons with energy of 0.01 MeV to 0.1 MeV, and fast neutrons with energies of 10 MeV to 20 MeV. The neutrons with higher energy of 20 MeV are called Relativistic neutrons.

Neutrons are mostly generated in reactors; also particle accelerator can be used to generate neutrons through different nuclear reactions. Neutron emission is possible from different reactions such as; (α, n) reaction, (γ, n) reaction and spontaneous fission. In the (α, n) reaction usually a light metal such as beryllium or boron and an alpha source, usually radium, polonium, or plutonium and a light metal, are mixed together as powder and encapsulated to make a radioactive neutron source. Neutrons from (α, n) reaction have continues energy spectrum. (γ, n) reactions are will emit neutrons with mono-energetic neutrons. Some of the heavy nuclei such as ^{254}Cf, ^{252}Cf, ^{244}Cm, ^{238}Pu and ^{235}U, can be a source of neutron; the neutron will be emitted through the spontaneous fission of these heavy nuclei.

Since neutrons are electrically neutral, they are not affected by the positive charges of the nucleus or by the electrons. As a result, neutrons will interact directly with the nucleus by passing through the atomic electron cloud. Therefore, neutrons collide with nuclei rather than the atom. There are two types of interaction that can occur as a result of neutrons interactions with matter; scattering, which can be divided in two reactions, elastic scattering and inelastic scattering. The other form of interaction is through neutron absorption, which can be divided into, radiation capture, charge particle, neutron producing, and fission reactions. Fig.1.

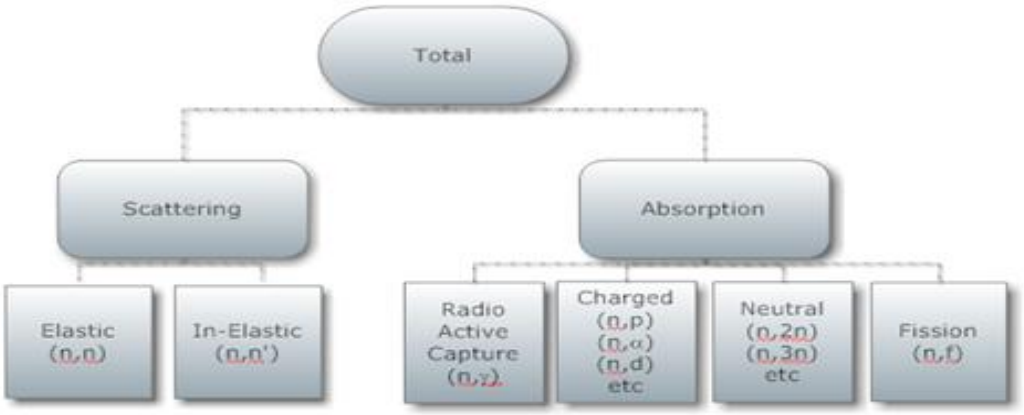

Fig.1 Neutron Interaction with Matter

When neutron collides with a nucleus, which is almost in its ground state, the neutron transfers some energy and bounces off in a different direction. When the energy lost by the neutron is equal to the kinetic energy of the recoil nucleus the scattering is elastic. This interaction could be represented using (n, n) notation. Elastic scattering reaction typically happens for fast neutrons.

The average energy loss could be calculated using the equation 1.

$$Average\ Energy\ loss = \frac{2EA}{(A+1)^2} \quad (1)$$

Where E represents the kinetic energy of the neutron and A represents the atomic weight of the nucleus. And the maximum transfer energy by the neutron of mass M and kinetic energy E_n to the nucleus of mass m in an elastic collision can be given by equation 2.

$$Q_{max} = \frac{4mME_n}{(M+m)^2} \quad (2)$$

In the case of inelastic scattering reaction, a neutron collides with the nucleus and it will be temporarily absorbed which would form a compound nucleus. The nucleus undergoes an internal rearrangement into an excited state which then emits another neutron of lower energy with a gamma photon (radiation). Therefore, the total kinetic energy of the nucleus and the outgoing neutron is less than the total kinetic energy of the incoming neutron. This excess of energy would place the nucleus into the excited state. Therefore, inelastic scattering generally happens only when high-energy neutron interact with heavy nuclei. Inelastic scattering reaction could be represented by the symbol (n,n') or (n,nγ) Fig.2(a) and (b).

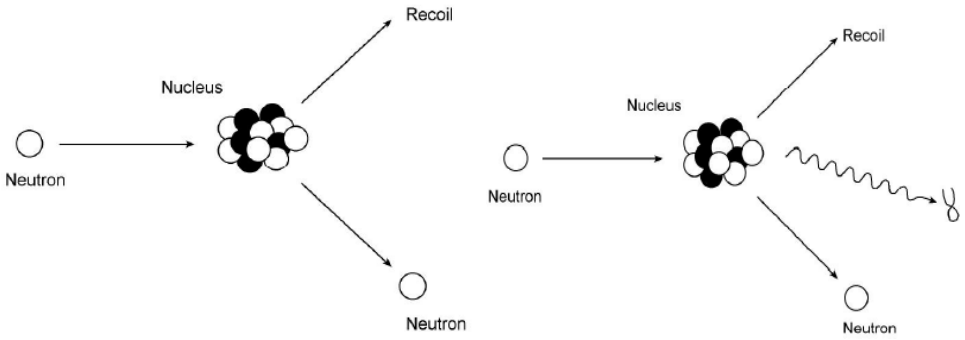

Fig.2 (a) Elastic Scattering **Fig.2 (b) Inelastic Scattering**[1]

[1] canteach.candu.org/library/20040706.pdf

Radioactive capture is the most common nuclear reaction. Where the neutron is captured by the nucleus and it forms a compound nucleus which then emits gamma photon called capture γ-rays and the product nucleus is an isotope of the same element as the original nucleus Fig.3.

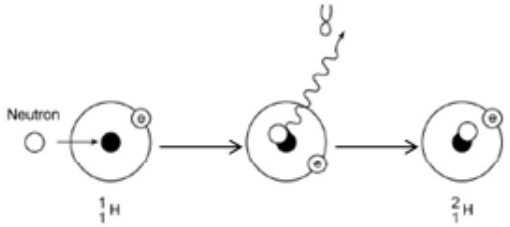

Fig.3 Radio Active Capture

Neutrons may be absorbed by the nucleus forming a compound nucleus, which then be de-energized by emitting a charged particle, either a photon or an alpha particle, this however would result in a nucleus of a different element, this reaction is called charge particle reaction.

In the neutron production reaction, an energetic incoming neutron strikes with the nucleus and as a result it would eject two or more neutrons from the nucleus. These reactions are endothermic since there are more than one neutrons being extracted when the nucleus is struck by the neutron. This reaction could be represented by the symbol (n, 2n), (n, 3n), etc...

Fission can be a result of neutron absorption by a heavy elements, the compound nucleus after capturing the thermal neutron would have an excess of energy. This excess of energy would excite the nucleus and result in immediate break-up or fission of the compound nucleus into fission fragments. The fission neutrons are emitted promptly from the fission fragments and the delayed neutrons will be emitted later. Most of the energy from fission is in the form of kinetic energy of the fission fragments. The positively charged fragments stop quickly and deposit their energy in a very short distance. Excitation of the nearby atoms and some direct collisions of the

fragments with the nuclei transfer some energy. The fission fragments are radioactive and mostly they decay several times to form a stable daughter nuclide Fig.4.

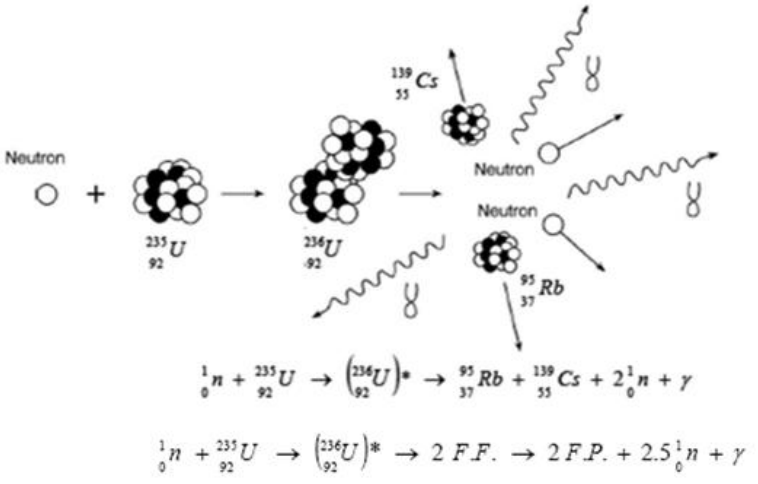

Fig.4 Neutron Fission

Appendix B: Part of the MCNPX Code used in the simulation

```
C
C Cell cards. Must be followed by a blank card
   1    281   -1.    -1         imp:n=1
   2    281   -1.    +1   -2    imp:n=1
   ……
   ……
   ……
   ……
   ……

   6    281   -1.    +5   -6    imp:n=1
   7    281   -1.    +6   -7    imp:n=1
   8    0             +7   -8    imp:n=1
 100    0             +8   -100  imp:n=1
 101    0             +100 -101  imp:n=0

C
C Surface cards. Must be followed by a blank card
   1  so    2.5
   2  so    5.0
   ……
   ……
   ……
   ……

   8  so   18.0
 100  so  100.
 101  so  101.

C
C Material cards
m281  1001.60c         -0.086  $MAT281
      7014.60c         -0.026 8016.60c         -0.323 6012.50c         -0.565

C
C
C Mode card
MODE   N
C
C
C Source cards
SDEF Par=1 POS=0 0 0 RAD=D2 CEL=100 ERG=D1
SI2  17.0 100.5
SP2 -21 2
SI1  L     0.1198      &
           0.1259      &
           0.1355      &
           0.1479      &
           0.1689      &
           0.1841      &
           0.216       &
       …….
       ……..
       ……..
```

```
        …….
            53.7836     &
            59.9363     &
            71.5748     &
            83.1075     &
            100.3552    &
            113.4697    &
            131.1807    &
            154.8389    &
           ……..
           ……
           ……
           ……
           ……
           ……
           ……


C
C ------------------------------------------------------------
C Energy binning for tally
E0          3.28E-06      &
            4.77E-06      &
            7.08E-06      &
            9.13E-06      &
            1.08E-05      &
           ……
           ……
           ……
           ……
            206.2481    &
            229.4193    &
            262.6032    &
            295.9579
C
C ------------------------------------------------------------
C Physics cards
PHYS:N 300 300
C
C ------------------------------------------------------------
C Problem cutoff cards
NPS   100000000
CUT:N 1000e2 1e-1 0
CTME  30
C
C ------------------------------------------------------------
C Tally cards
F4:N  1 3 5 7 8
```

Appendix C: Additional Results of MCNPX

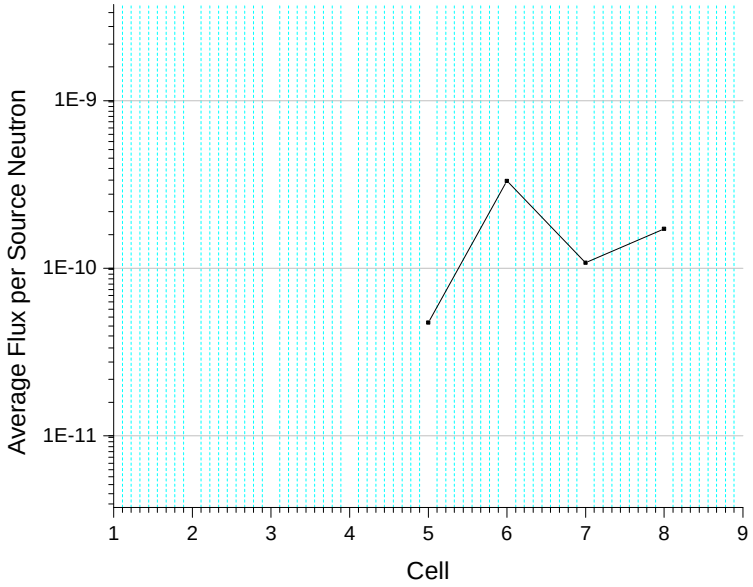

Neutron Production in all cells of the phantom from interaction of 20 MeV protons with Phantom

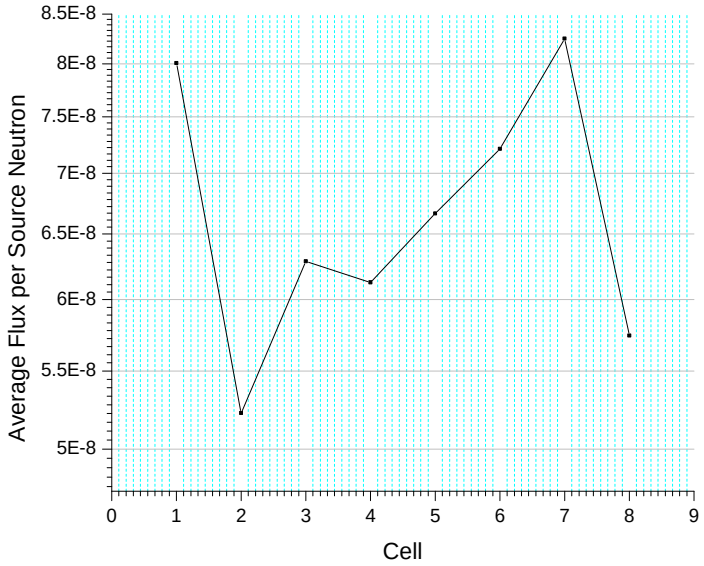

Neutron Production in all cells of the phantom from interaction of 50 MeV protons with Phantom

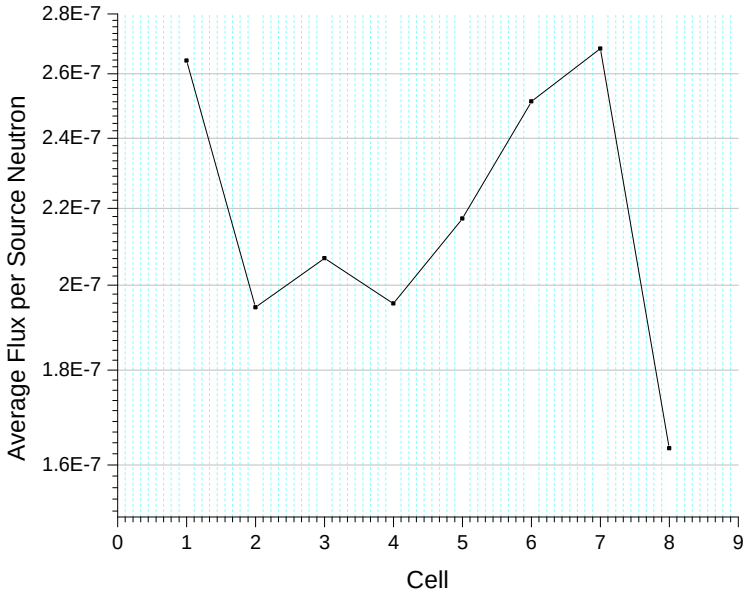

Neutron Production in all cells of the phantom from interaction of 70 MeV protons with Phantom

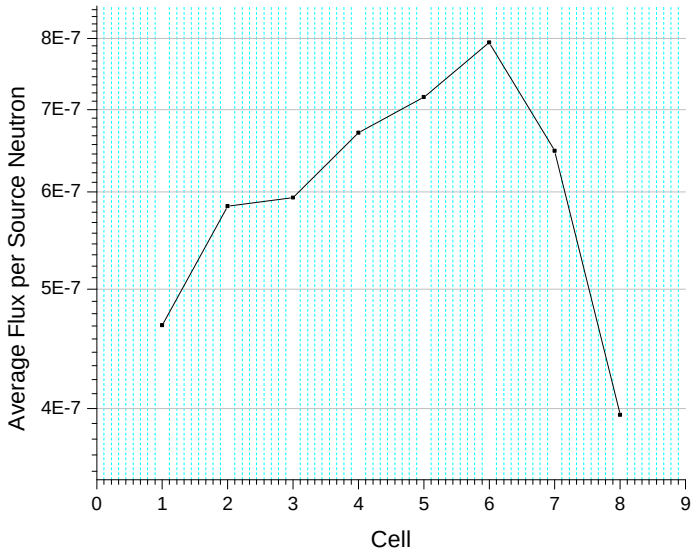

Neutron Production in all cells of the phantom from interaction of 100 MeV protons with Phantom

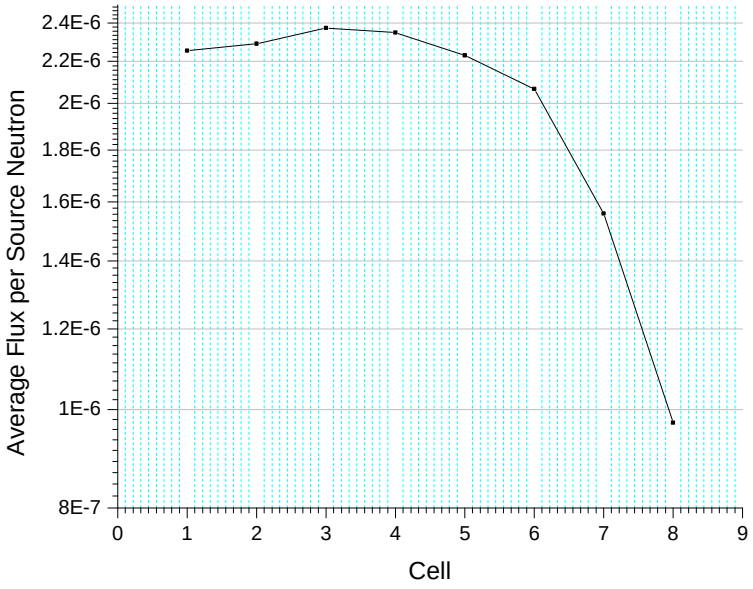

Neutron Production in all cells of the phantom from interaction of 150 MeV protons with Phantom

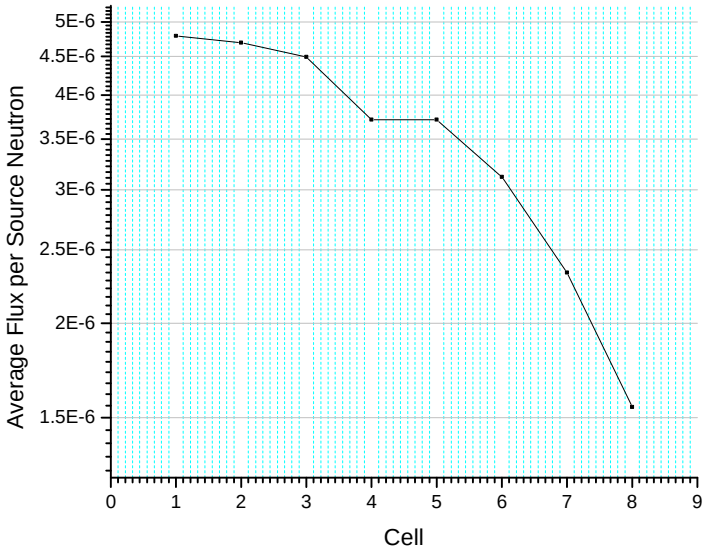

Neutron Production in all cells of the phantom from interaction of 200 MeV protons with Phantom

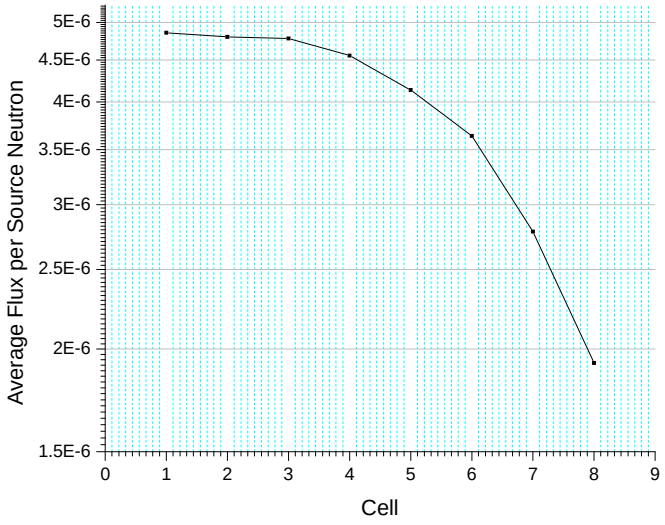

Neutron Production in all cells of the phantom from interaction of 250 MeV protons with Phantom

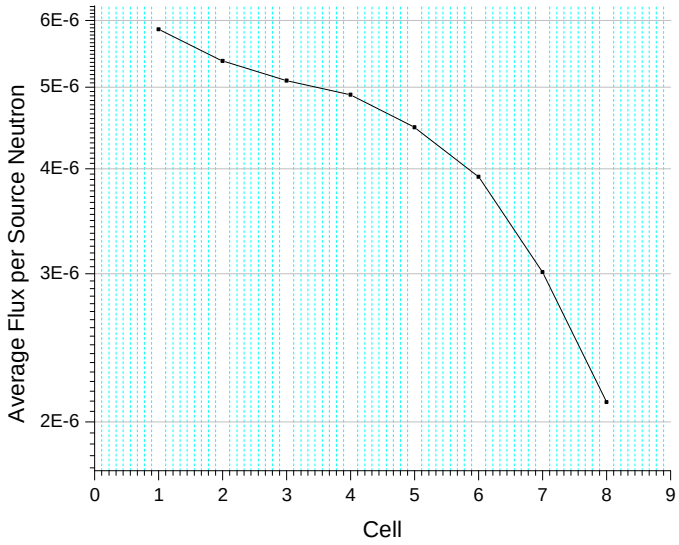

Neutron Production in all cells of the phantom from interaction of 300 MeV protons with Phantom

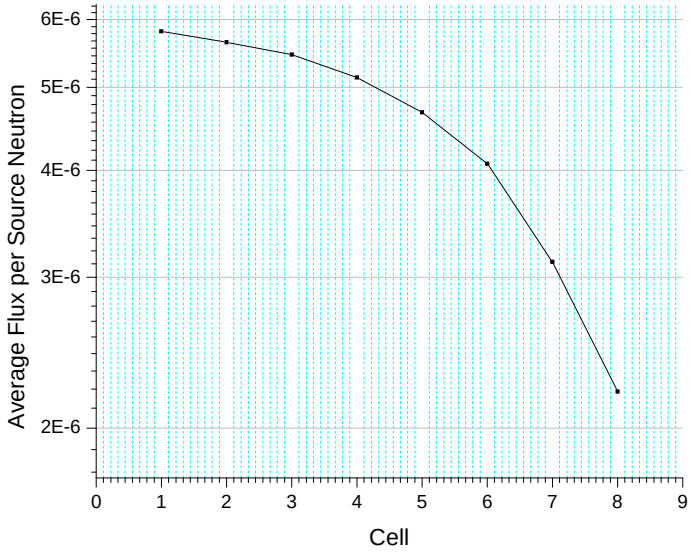

Neutron Production in all cells of the phantom from interaction of 350 MeV protons with Phantom

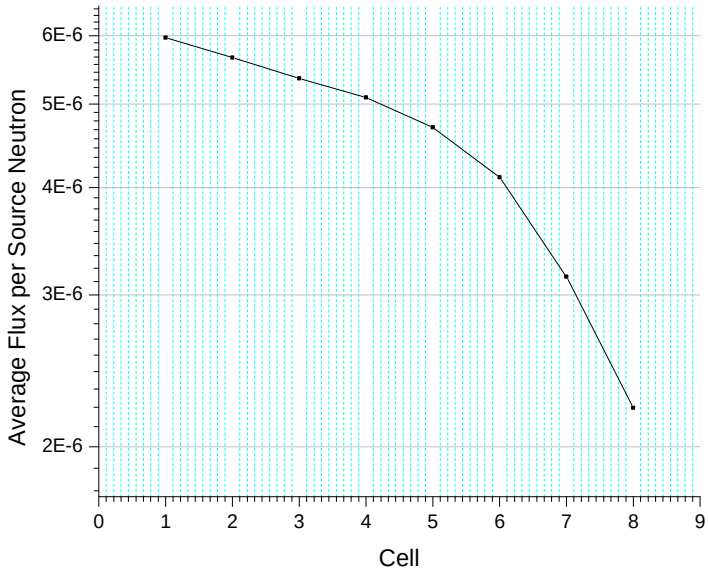

Neutron Production in all cells of the phantom from interaction of 400 MeV protons with Phantom

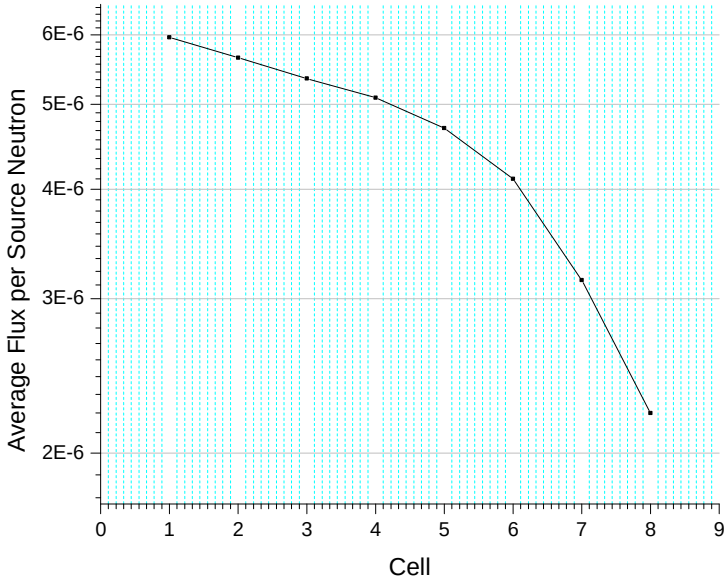

Neutron Production in all cells of the phantom from interaction of 450 MeV protons with Phantom

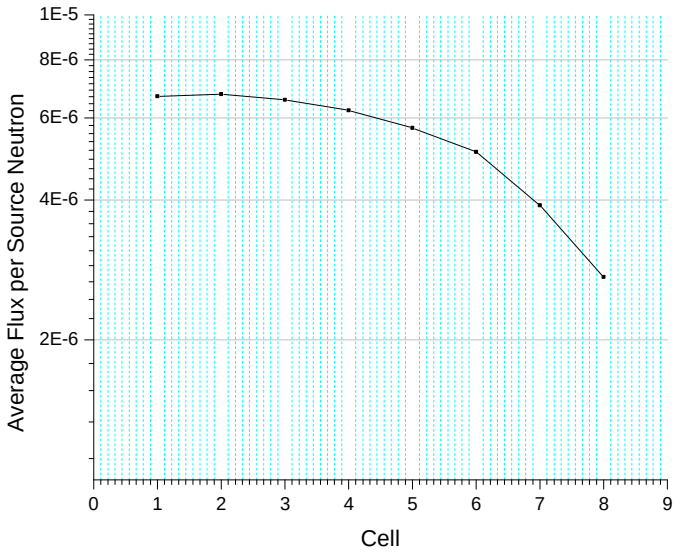

Neutron Production in all cells of the phantom from interaction of 550 MeV protons with Phantom

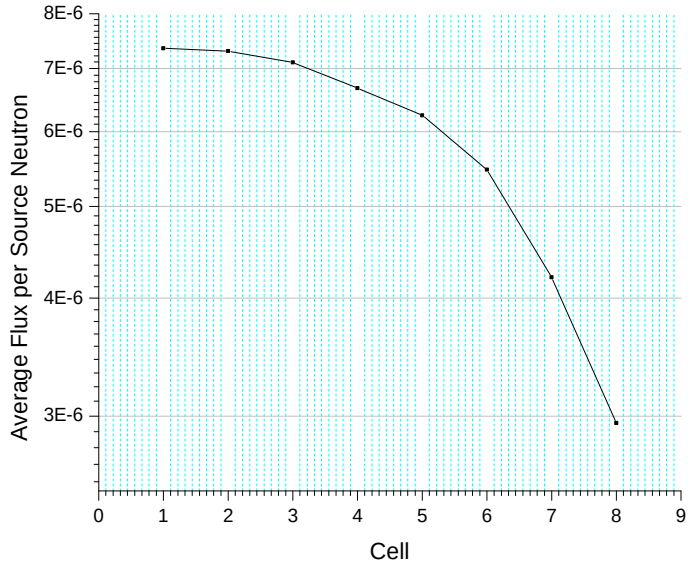

Neutron Production in all cells of the phantom from interaction of 600 MeV protons with Phantom

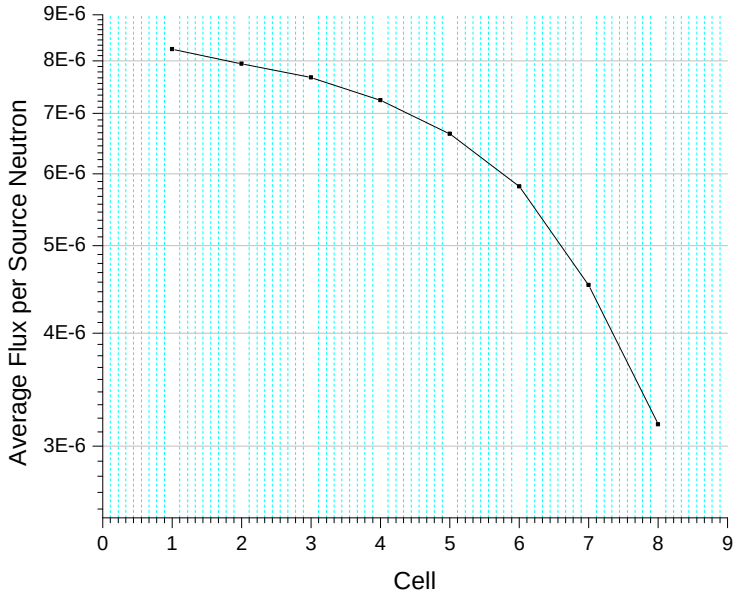

Neutron Production in all cells of the phantom from interaction of 650 MeV protons with Phantom

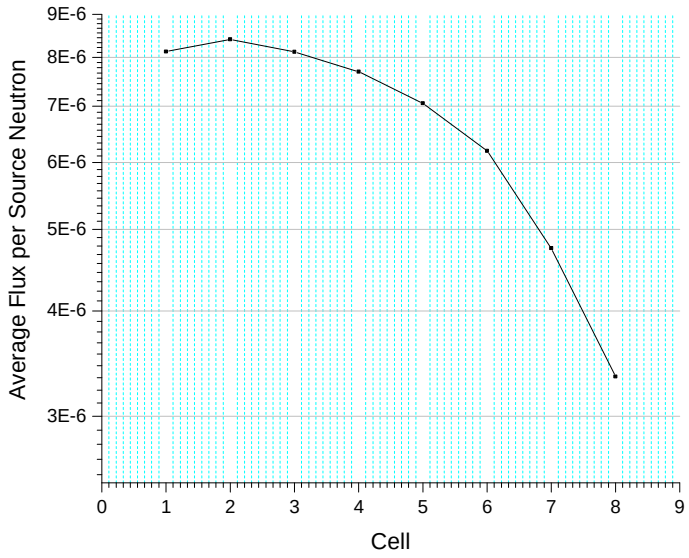

Neutron Production in all cells of the phantom from interaction of 700 MeV protons with Phantom

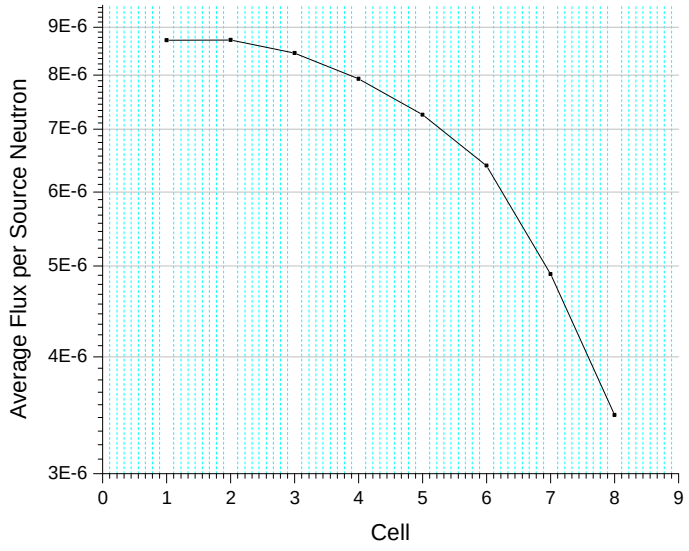

Neutron Production in all cells of the phantom from interaction of 750 MeV protons with Phantom

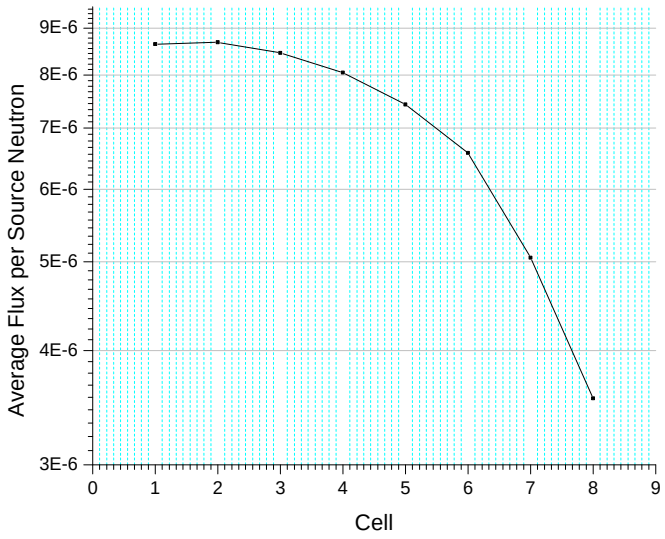

Neutron Production in all cells of the phantom from interaction of 800 MeV protons with Phantom

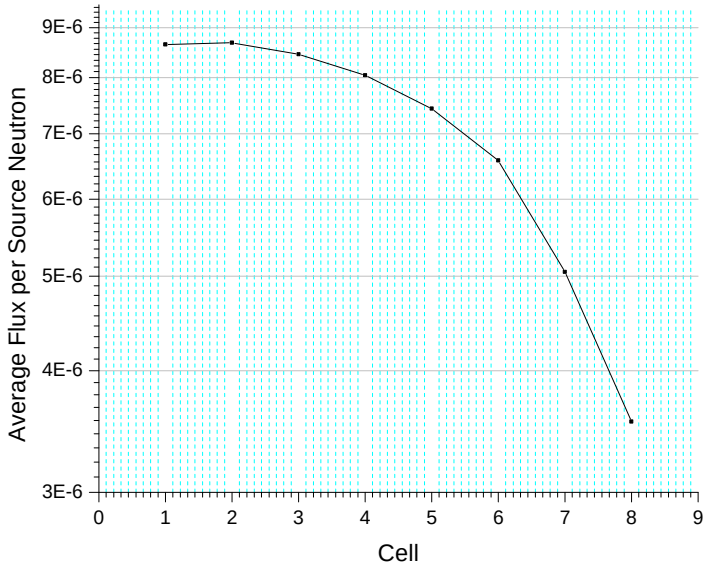

Total Neutron Production in all cells of the phantom from interaction of 10-800 MeV protons with Phantom

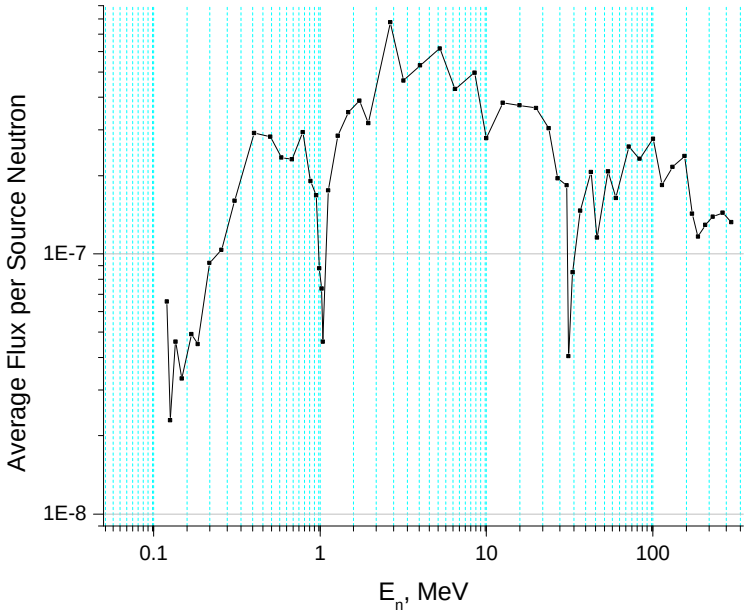

Neutron Flux behind Aluminum Shielding (7.5 g/cm^2)

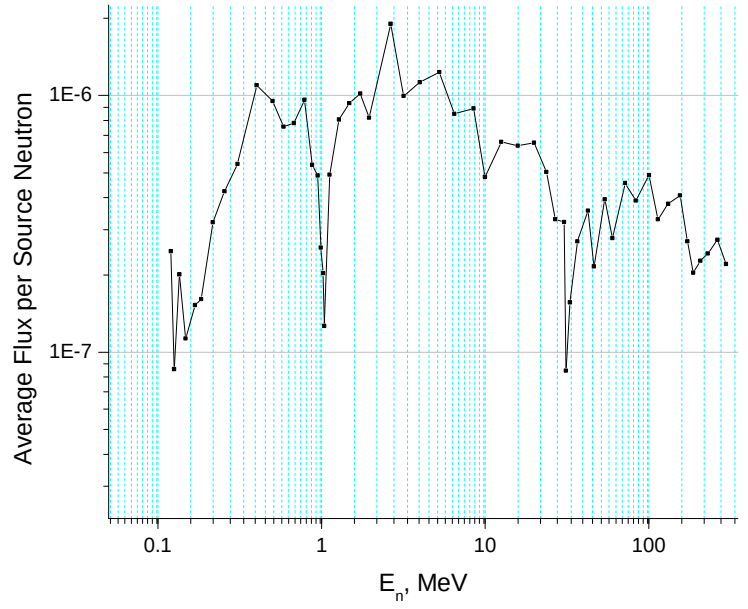

Neutron Flux behind Aluminum Shielding (15 g/cm^2)

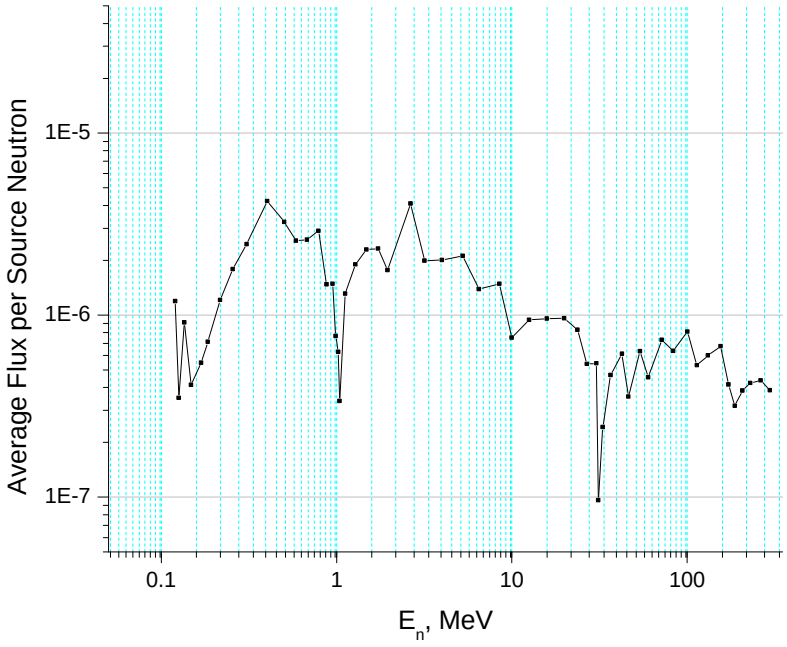

Neutron Flux behind Aluminum Shielding (30 g/cm^2)

Appendix D: Average daily proton integral spectra ($p.cm^{-2}day^{-1}$) behind shielding of varying thickness at minimum solar activity.

ENERGY (MeV)	**0.0** $g.cm^{-2}$	**0.3** $g.cm^{-2}$	**3.0** $g.cm^{-2}$	**7.0** $g.cm^{-2}$	**15.0** $g.cm^{-2}$	**30.0** $g.cm^{-2}$	**50.0** $g.cm^{-2}$
10	$3.3.10^{6}$	$2.6.10^{6}$	$1.7.10^{6}$	$1.2.10^{6}$	$7.1.10^{5}$	$3.5.10^{5}$	1.8E+05
20	$2.5.10^{6}$	$2.2.10^{6}$	$1.6.10^{6}$	$1.2.10^{6}$	$7.0.10^{5}$	$3.5.10^{5}$	1.7E+05
30	$2.1.10^{6}$	$2.0.10^{6}$	$1.5.10^{6}$	$1.1.10^{6}$	$6.7.10^{5}$	$3.4.10^{5}$	1.7E+05
40	$1.9.10^{6}$	$1.8.10^{6}$	$1.4.10^{6}$	$1.0.10^{6}$	$6.5.10^{5}$	$3.3.10^{5}$	1.7E+05
50	$1.7.10^{6}$	$1.6.10^{6}$	$1.3.10^{6}$	$9.9.10^{5}$	$6.2.10^{5}$	$3.2.10^{5}$	1.6E+05
60	$1.5.10^{6}$	$1.5.10^{6}$	$1.2.10^{6}$	$9.2.10^{5}$	$5.8.10^{5}$	$3.1.10^{5}$	1.6E+05
70	$1.4.10^{6}$	$1.3.10^{6}$	$1.1.10^{6}$	$8.5.10^{5}$	$5.5.10^{5}$	$2.9.10^{5}$	1.5E+05
80	$1.2.10^{6}$	$1.2.10^{6}$	$1.0.10^{6}$	$7.8.10^{5}$	$5.1.10^{5}$	$2.8.10^{5}$	1.4E+05
90	$1.1.10^{6}$	$1.1.10^{6}$	$9.0.10^{5}$	$7.2.10^{5}$	$4.8.10^{5}$	$2.6.10^{5}$	1.4E+05
100	$9.7.10^{6}$	$9.6.10^{5}$	$8.2.10^{5}$	$6.5.10^{5}$	$4.4.10^{5}$	$2.5.10^{5}$	1.3E+05
120	$7.7.10^{5}$	$7.6.10^{5}$	$6.6.10^{5}$	$5.4.10^{5}$	$3.7.10^{5}$	$2.2.10^{5}$	1.2E+05
140	$6.1.10^{5}$	$6.1.10^{5}$	$5.4.10^{5}$	$4.5.10^{5}$	$3.2.10^{5}$	$1.9.10^{5}$	1.0E+05
160	$4.9.10^{5}$	$4.8.10^{5}$	$4.4.10^{5}$	$3.7.10^{5}$	$2.6.10^{5}$	$1.6.10^{5}$	9.2E+04
180	$3.9.10^{5}$	$3.9.10^{5}$	$3.5.10^{5}$	$3.0.10^{5}$	$2.2.10^{5}$	$1.4.10^{5}$	8.1E+04
200	$3.1.10^{5}$	$3.1.10^{5}$	$2.9.10^{6}$	$2.5.10^{5}$	$1.9.10^{5}$	$1.2.10^{5}$	7.0E+04
250	$1.9.10^{5}$	$1.8.10^{5}$	$1.7.10^{5}$	$1.5.10^{5}$	$1.2.10^{5}$	$7.9.10^{4}$	4.9E+04
300	$1.1.10^{5}$	$1.1.10^{5}$	$1.0.10^{5}$	$9.2.10^{4}$	$7.4.10^{4}$	$5.2.10^{4}$	3.3E+04
350	$7.0.10^{4}$	$6.9.10^{4}$	$6.5.10^{4}$	$5.6.10^{4}$	$4.6.10^{4}$	$3.3.10^{4}$	2.3E+04
400	$4.3.10^{4}$	$4.3.10^{4}$	$4.0.10^{4}$	$3.4.10^{4}$	$2.8.10^{4}$	$2.2.10^{4}$	1.5E+04
500	$1.6.10^{4}$	$1.6.10^{4}$	$1.6.10^{4}$	$1.2.10^{4}$	$1.0.10^{4}$	$8.6.10^{4}$	6.8E+03
600	$5.3.10^{3}$	$5.3.10^{3}$	$5.0.10^{3}$	$2.2.10^{3}$	$2.2.10^{3}$	$2.1.10^{3}$	2.1E+03

Appendix E: Peak proton integral spectra (pr/cm2/day) behind shielding of varying thickness during passes of the ISS through the SAA at minimum solar activity

ENERGY (MeV)	**0.0** $g.cm^{-2}$	**0.3** $g.cm^{-2}$	**3.0** $g.cm^{-2}$	**7.0** $g.cm^{-2}$	**15.0** $g.cm^{-2}$	**30.0** $g.cm^{-2}$	**50.0** $g.cm^{-2}$
10	1.8E+08	1.6E+08	1.3E+08	9.5E+07	5.8E+07	2.9E+07	1.5E+07
20	1.6E+08	1.6E+08	1.2E+08	9.3E+07	5.7E+07	2.9E+07	1.5E+07
30	1.5E+08	1.5E+08	1.2E+08	8.9E+07	5.5E+07	2.8E+07	1.4E+07
40	1.4E+08	1.4E+08	1.1E+08	8.4E+07	5.3E+07	2.7E+07	1.4E+07
50	1.3E+08	1.3E+08	1.0E+08	7.9E+07	5.0E+07	2.6E+07	1.4E+07
60	1.2E+08	1.2E+08	9.6E+07	7.4E+07	4.7E+07	2.5E+07	1.3E+07
70	1.1E+08	1.1E+08	8.8E+07	6.9E+07	4.5E+07	2.4E+07	1.3E+07
80	9.7E+07	9.6E+07	8.0E+07	6.3E+07	4.2E+07	2.3E+07	1.2E+07
90	8.8E+07	8.6E+07	7.3E+07	5.8E+07	3.9E+07	2.2E+07	1.2E+07
100	7.8E+07	7.7E+07	6.6E+07	5.3E+07	3.6E+07	2.1E+07	1.1E+07
120	6.3E+07	6.2E+07	5.4E+07	4.5E+07	3.1E+07	1.8E+07	1.0E+07
140	5.0E+07	4.9E+07	4.4E+07	3.7E+07	2.6E+07	1.6E+07	8.9E+06
160	4.0E+07	4.0E+07	3.6E+07	3.1E+07	2.2E+07	1.4E+07	7.9E+06
180	3.2E+07	3.2E+07	2.9E+07	2.5E+07	1.9E+07	1.2E+07	6.9E+06
200	2.6E+07	2.6E+07	2.4E+07	2.1E+07	1.6E+07	1.0E+07	6.0E+06
250	1.6E+07	1.6E+07	1.5E+07	1.3E+07	1.0E+07	6.9E+06	4.1E+06
300	9.8E+06	9.7E+06	9.1E+06	8.0E+06	6.4E+06	4.4E+06	2.7E+06
350	6.0E+06	6.0E+06	5.6E+06	4.9E+06	3.9E+06	2.8E+06	1.7E+06
400	3.6E+06	3.6E+06	3.4E+06	2.9E+06	2.3E+06	1.7E+06	1.1E+06
500	1.3E+06	1.2E+06	1.2E+06	9.0E+05	7.4E+05	5.4E+05	3.5E+05
600	2.9E+05	2.9E+05	2.7E+05	9.8E+03	9.1E+03	8.0E+03	6.8E+03

Appendix F: (He-U) heavy ion integral LET spectra (1/cm2/day) behind shielding of varying thickness given the absence of solar flares and a magnetic activity index of Wi=4**.**

LET	**0**	**0.3**	**3**	**7**	**15**	**30**	**50**
$MeV.cm^2.mg^{-1}$	$g.cm^{-2}$	$g.cm^{-2}$	$g.cm^{-2}$	$g.cm^{-2}$	$g.cm^{-2}$	$g.cm^{-2}$	$g.cm^{-2}$
0.002	1.4E+04	1.4E+04	1.3E+04	1.2E+04	1.0E+04	7.1E+03	4.5E+03
0.003	1.4E+04	1.4E+04	1.3E+04	1.2E+04	1.0E+04	7.1E+03	4.5E+03
0.004	1.4E+04	1.4E+04	1.3E+04	1.2E+04	1.0E+04	7.1E+03	4.5E+03
0.005	1.4E+04	1.4E+04	1.3E+04	1.2E+04	1.0E+04	7.1E+03	4.5E+03
0.006	1.4E+04	1.4E+04	1.3E+04	1.2E+04	1.0E+04	7.1E+03	4.5E+03
0.007	9.6E+03	9.5E+03	8.9E+03	8.1E+03	6.6E+03	4.6E+03	2.8E+03
0.008	5.5E+03	5.4E+03	5.0E+03	4.5E+03	3.6E+03	2.4E+03	1.4E+03
0.009	4.5E+03	4.4E+03	4.1E+03	3.7E+03	2.9E+03	1.9E+03	1.1E+03
0.01	3.8E+03	3.8E+03	3.5E+03	3.1E+03	2.5E+03	1.6E+03	8.6E+02
0.02	1.5E+03	1.5E+03	1.4E+03	1.3E+03	1.0E+03	6.3E+02	3.2E+02
0.03	1.2E+03	1.1E+03	1.0E+03	9.2E+02	7.2E+02	4.6E+02	2.3E+02
0.04	1.0E+03	1.0E+03	9.4E+02	8.3E+02	6.4E+02	4.0E+02	2.0E+02
0.05	9.4E+02	9.2E+02	8.4E+02	7.4E+02	5.7E+02	3.5E+02	1.8E+02
0.06	8.9E+02	8.7E+02	8.0E+02	7.0E+02	5.3E+02	3.2E+02	1.6E+02
0.07	6.9E+02	6.7E+02	6.2E+02	5.3E+02	4.0E+02	2.4E+02	1.2E+02
0.08	6.5E+02	6.3E+02	5.7E+02	5.0E+02	3.7E+02	2.2E+02	1.1E+02
0.09	5.8E+02	5.7E+02	5.1E+02	4.4E+02	3.3E+02	1.9E+02	9.4E+01
0.1	5.4E+02	5.3E+02	4.8E+02	4.1E+02	3.1E+02	1.8E+02	8.6E+01
0.2	2.3E+02	2.2E+02	2.0E+02	1.6E+02	1.2E+02	6.1E+01	2.7E+01
0.3	1.5E+02	1.4E+02	1.2E+02	1.0E+02	7.0E+01	3.5E+01	1.4E+01
0.4	1.0E+02	8.7E+01	7.6E+01	6.2E+01	4.1E+01	2.0E+01	7.5E+00
0.5	8.7E+01	7.1E+01	6.1E+01	5.0E+01	3.3E+01	1.5E+01	5.6E+00
0.6	7.8E+01	6.2E+01	5.3E+01	4.3E+01	2.8E+01	1.3E+01	4.6E+00
0.7	7.0E+01	5.5E+01	4.7E+01	3.8E+01	2.4E+01	1.1E+01	3.9E+00
0.8	6.5E+01	4.9E+01	4.2E+01	3.4E+01	2.2E+01	9.7E+00	3.4E+00
0.9	6.0E+01	4.4E+01	3.8E+01	3.1E+01	2.0E+01	8.7E+00	3.0E+00
1	5.5E+01	4.0E+01	3.4E+01	2.8E+01	1.8E+01	7.8E+00	2.7E+00
2	1.2E+01	2.9E+00	2.2E+00	1.8E+00	1.1E+00	4.6E-01	1.6E-01
3	6.5E+00	1.2E+00	7.8E-01	6.6E-01	4.0E-01	1.7E-01	5.6E-02
4	4.2E+00	7.4E-01	4.0E-01	3.4E-01	2.0E-01	8.4E-02	2.9E-02
5	3.1E+00	5.1E-01	2.3E-01	2.0E-01	1.2E-01	4.9E-02	1.7E-02
6	2.4E+00	3.8E-01	1.5E-01	1.3E-01	7.8E-02	3.2E-02	1.1E-02
7	1.9E+00	2.8E-01	1.1E-01	8.8E-02	5.3E-02	2.2E-02	7.1E-03
8	1.5E+00	2.2E-01	7.6E-02	6.4E-02	3.8E-02	1.5E-02	5.0E-03
9	1.3E+00	1.8E-01	5.7E-02	4.7E-02	2.8E-02	1.1E-02	3.7E-03
10	1.0E+00	1.4E-01	4.4E-02	3.6E-02	2.2E-02	8.7E-03	2.8E-03
20	1.5E-01	2.7E-02	5.9E-03	4.8E-03	2.8E-03	1.1E-03	3.4E-04
30	8.3E-07	1.7E-05	3.6E-05	3.0E-05	1.6E-05	5.9E-06	1.7E-06
40	1.9E-07	9.8E-07	1.9E-06	1.3E-06	5.7E-07	1.3E-07	2.2E-08
50	6.2E-08	4.1E-07	8.4E-07	5.5E-07	2.3E-07	4.8E-08	7.1E-09
60	2.1E-08	1.7E-07	3.6E-07	2.3E-07	9.3E-08	1.7E-08	2.2E-09
70	5.1E-09	7.5E-08	1.7E-07	1.0E-07	4.0E-08	6.8E-09	8.2E-10

LET	0	0.3	3	7	15	30	50
$MeV.cm^2.mg^{-1}$	$g.cm^{-2}$	$g.cm^{-2}$	$g.cm^{-2}$	$g.cm^{-2}$	$g.cm^{-2}$	$g.cm^{-2}$	$g.cm^{-2}$
80	4.9E-10	3.1E-08	7.3E-08	4.5E-08	1.7E-08	2.8E-09	3.2E-10
90	-	6.0E-09	1.4E-08	8.8E-09	3.2E-09	4.9E-10	5.5E-11

Appendix G: US short-term and career ionizing radiation exposure limits

Organ-specific exposure limits (Sv)			
Exposure interval	**Over all organs**	**Eye**	**Skin**
30 Days	0.25	1.0	1.5
Annual	0.50	2.0	3.0

Career Exposure Limits Over All Organs (Sv)				
	Age			
	25	35	45	55
Male	0.70	1.00	1.50	3.00
Female	0.40	0.60	0.90	1.70

Appendix H: Additional Radiation Dosimetry References

1. W. Schimmerling, Gravitational and Space Biology Bulletin **16(2)**, 5 (2003)
2. F.A. Cucinotta, M.-H.Y. Kim and L. Ren, NASA/TP-20050210XXX (2005)
3. B.J. Lewis, "Review of Radiation Detector Research and Development Technology Development", report to the Canadian Space Agency, 2001
4. http://srag-nt.jsc.nasa.gov/
5. F. Sulzman, F. Cucinotta, M. Golightly and W. Schimmerling, Radiation Dosimetry Working Group Final Report, 2003
6. NASA–Johnson Space Center Flight Rules, draft, November 2000
7. http://www.thomson-elec.com/
8. http://www.bubbletech.ca/
9. H. Ing and C. Birnboim, "Bubble-Damage Polymer Detector for Neutrons," Nucl. Tracks Rad. Meas. **8**, 285 (1984)
10. G. Jonkmans et. al., Acta Astronautica **56,** 975 (2005)
11. M.B. Smith et. al., Proceedings of the International Workshop on Fast Neutron Detectors and Applications, Cape Town, South Africa, April 3-6, 2006, Proceedings of Science, PoS(FNDA2006)006 (2006)
12. J. Miller, 16th Annual NASA Space Radiation Investigators' Workshop, Port Jefferson, New York, May 15–18, 2005
13. T. Nakamura, Proceedings of the 2nd International Space Workshop, Chiba, Japan, February 16-18, 2000, pp. 27
14. B.W. Glickman, "Biomonitoring Radiation Effects in Astronauts in Space: a Canadian Perspective", report to the Canadian Space Agency, 2003, CSA contract number 9F008-2-0127
15. Proceedings of the International Workshop on Predictions and Measurements of Secondary Neutrons in Space, Universities Space Research Association, Center for Advanced Space Studies, 3600 Bay Area Boulevard, Houston, Texas 77058-1113, USA, September 28-30, 1998
16. http://www.sciencedaily.com/releases/2003/11/031112073014.htm
17. R.H. Maurer, J.D. Kinnison and D.R. Roth, Radiation Protection Dosimetry **116**, 125 (2005)
18. P. Goldhagen, "EML Multisphere Neutron Spectrometer, Ion Chamber and Scintillation Counters," Atmospheric Ionizing Radiation Investigators Workshop, NASA Langley Research Centre, Hampton, Virgina, March 31, 1998
19. http://www.hq.nasa.gov/office/codeq/trl/index.htm